Numerical modeling of flow and scour using strict vertex-based terrain conformal moving mesh with masked elements

Xiaohui Yan

Thesis submitted to the University of Ottawa
in partial fulfillment of the requirements for the
Doctorate in Philosophy degree in Civil Engineering

Department of Civil Engineering
Faculty of Engineering
University of Ottawa

uOttawa
L'Université canadienne
Canada's university

Université d'Ottawa | University of Ottawa

Abstract

Local scour can jeopardize the safety of the hydraulic structures and the ecology of a river system, so it is desirable to understand better the relevant processes and characteristics, and thus it is of primary importance for researchers to propose better research methodologies or numerical models. OpenFOAM is attractive for sediment-scour applications because of its high-quality hydrodynamic solvers and turbulence models, and its advantages of being open source and readily modifiable and extendable. However, the standard OpenFOAM package does not have a sediment scour module. It lacks the ability to perform large-amplitude motions needed for sediment-scour problems, and thus its application is normally restricted to small-amplitude cases to prevent divergence due to mesh deterioration.

The first part of this study presents the implementation and validation of a new sediment-scour model with a strict vertex-based terrain conformal moving-mesh technique within the framework of OpenFOAM. The proposed simple moving-mesh technique in OpenFOAM is implemented to overcome the shortcomings of the conventional automatic mesh-motion techniques in handling large-amplitude moving geometries. The model is employed to simulate a simple case of prescribed boundary motion, a previous experiment in the literature, and a new laboratory experiment for local scour due to submerged wall jets. The results are compared with both the experimental and other numerical results. The comparisons demonstrate that the present model has the novel advantage of allowing for more severe topographic variations, and can provide more reliable predictions for the key characteristics and evolution of the bed profiles in wall jet scour problems.

The second part of this study extends the model presented in the first part to simulate cases in which there is an embedded structure (here, a pipeline). In contrast to previous moving-mesh models, the newly implemented model uses masked elements to resolve the effects of the stationary object on the flow and sediment scour processes. This approach makes it possible to track directly the moving fluid-sediment interface using a very simple mesh setup, which is more practical for engineering computations than the existing models.

The third part of this study further applies the proposed masked-element approach to simulate local scour at submerged weirs with downstream slopes. A new laboratory experiment is reported and used to validate the model. The effects of various parameters and configurations on the numerical predictions are studied, including the roughness height estimation, angle of repose, turbulence model, stochastic model, critical Shields number, and the form of the sand-slide model.

The fourth part of this study provides some additional results and discussions, including the applications of the wall jet scour model, numerical modeling of flow around a pipeline near a scoured bed, and mesh configurations and improvement.

Acknowledgements

My deepest appreciation goes to my supervisors, Dr. Majid Mohammadian and Dr. Colin Rennie, without whom I could not possibly have embarked upon this study. Their wide-ranging supervision and unwavering support means a lot to me. Their tireless guidance has also cultivated my interest in water resources engineering.

Thanks also to Dr. Hossein Bonakdari, Dr. Ioan Nistor, Dr. Julio Angel Infante Sedano, Dr. Ousmane Seidou, and Dr. Ryan Mulligan, whose suggestions, intelligence and resourcefulness make a real difference in this project. I would like to thank the anonymous reviewers for their careful reading of our manuscripts, and their insightful comments and suggestions. I would like to acknowledge Mark Lapointe, Marieh Rajaie, Shilong Liu, and Amanj Jamal at the Water Resources Engineering Laboratory (University of Ottawa) for their assistance in conducting the experiments.

I would like to thank the China Scholarship Council (CSC) for providing me the scholarship and financial support for my graduate study. I would also like to mention that the officers in the Education Section of the Embassy of China, such as Mrs. Xinyu Yang, Mr. Yuguang Guo, and Mr. Zhehua Dai, have provided me with many helpful suggestions and motivations for my study and life during my Ph.D. study and my future career.

I would also like to thank my parents, Changkun Yan and Ping Sun, who are both working in the field of water resources engineering, for their love and support, raising me up, and encouraging me to become engaged in water resources engineering. My proudest thing in life is that we are a “water resources engineering” family. I would also like to

thank my wife, Xin Chen, who is also a PhD student in water resources engineering at the University of Ottawa, and my parents in law, Lin Zhu and Huiqing Chen. They have spent a lot more time than me in taking care of our family, and are very supportive for my studies and career plans. I really want to express my love to my son, Ryan Yan: I will always do what is best for you. If you also want to work in water resources engineering in your future, like your grandparents and parents, I hope you can be the best engineer or researcher in the world.

Last but not least, I would like to thank my friends at the University of Ottawa, such as Amir Gharavi, Behnaz Ghodoosipou, Iman Bahreini, Kate Neigel, Shilong Liu, Yarzar Tun, and Xueming Wang, for providing the support and friendship that I needed.

Table of Contents

List of Figures

List of Tables

List of Symbols

a_s = mesh smoothing coefficient;

B_0 = width of the gate opening;

$c_{1\varepsilon}$ = constant in turbulence model;

$c_{2\varepsilon}$ = constant in turbulence model;

c_μ = constant in turbulence model;

C_s = roughness constant;

d = grain diameter;

d_{50} = median grain size;

d_χ = sediment diameter (χ percent sediment is finer);

E_r = roughness coefficient;

g = gravitational acceleration vector;

G = production of turbulence due to shear;

h_b = depth of sediment bed;

h_d = tail water level;

h_o = sluice gate opening;

h_u = upstream water level;

h_w = height of overflow weir;

I = turbulence intensity;

k_s = sand–grain roughness height;

k_s^+ = dimensionless sand–grain roughness height;

l = turbulence length scale;

L = characteristic length;

L_g = Length of sluice gate;

L_a = length of apron measured from the sluice gate;

L_r = length of upstream reservoir;

L_s = length of sediment bed;

L_w = length of overflow weir;

$\mathrm{N_e}$ = number of cells;

$\mathrm{N_{eo}}$ = reference number of cells;

q_B = bed–load flux vector;

q_{Bi} = bed–load transport rate in the *i*–th direction;

q_i^* = dimensionless bed–load transport rate;

k = turbulent kinetic energy;

p = pressure;

Re = Reynolds number;

t = time;

T = viscous stresses tensor;

$\bar{u}$ = average velocity under the sluice gate;

$\vec{u}$ = grid motion velocity field;

U = flow velocity vector;

U_a = velocity of the air phase;

U_{1i} = velocity of the flow parallel to the bed at the first cell center;

$U_{\text{Prescribed}}$ = prescribed boundary motion velocity;

U_{r} = relative velocity vector;

u_τ = friction velocity;

U_w = velocity of the water phase;

U_{wi} = velocity of the flow on the wall;

x = horizontal coordinate;

y = vertical coordinate;

y_{bottom} = vertical coordinate of the bottom boundary in a water column;

y_i = bed elevation at point P_{i};

$y_{initial}$ = initial vertical coordinate of a node;

y_{i-1} = bed elevation at point $\mathrm{P}_{\mathrm{i-1}}$;

y_{i+1} = bed elevation at point $\mathrm{P}_{\mathrm{i+1}}$;

$\mathrm{y}_{\mathrm{i,new}}$ = New bed elevation at point P_{i};

$\mathrm{y}_{\mathrm{i+1,new}}$ = New bed elevation at point $\mathrm{P}_{\mathrm{i+1}}$;

y_{new} = new vertical coordinate of an internal node;

Y_{top} = vertical coordinate of the top boundary in a water column;

y_1 = perpendicular distance of the first cell center to the wall;

y^+ = non–dimensional distance to the wall;

z_b = bed elevation;

α = fraction function;

δ = empirical coefficient for sand–grain roughness height;

ε = turbulent energy dissipation rate;

γ = bed material porosity;

γ_d = diffusion field;

κ = von Karman constant;

μ = dynamic viscosity;

μ_a = dynamic viscosity of the air phase;

μ_w = dynamic viscosity of the water phase;

ν = kinematic viscosity;

ν_{eff} = effective viscosity;

ν_t = turbulent kinematic viscosity;

ρ = density of the mixed fluid;

ρ_a = density of the air phase;

ρ_s = density of the bed material;

ρ_w = density of the water phase;

σ_k = constant in turbulence model;

σ_ε = constant in turbulence model;

τ_{bi} = bed shear stress;

θ_c = critical Shields number;

θ_i = Shields number.

List of Acronyms

ADV = acoustic Doppler velocimetry;

CFD = computational fluid dynamics;

DDES = delayed detached-eddy simulation;

Exp = experimental;

FAVOR = fractional area-volume obstacle representation;

GIMP = GNU Image Manipulation Program;

IDDES = improved delayed detached eddy simulation;

LES = large-eddy simulation;

LRR = Launder-Reece-Rodi;

MAPE = mean absolute percentage error;

Num = numerical;

OpenFOAM = open-source field operation and manipulation;

PGC = preconditioned conjugate gradient;

PIV = particle image velocimetry;

PTV = particle tracking velocimetry;

RANS = Reynolds-Averaged Navier-Stokes equations;

RMSE = root-mean square error;

RNG = re-normalisation group

R^2 = coefficient of determination;

SGS = subgrid scale;

SST = shear stress transport;

TM = turbulence model;

VOF = volume of fluid;

2D = two-dimensional;

3D = three-dimensional.

Chapter 1 Introduction

1.1 Introduction

Turbulent jets or hydraulic structures may cause severe local erosion of streambed material, which can jeopardize the safety of the hydraulic structures (Dey and Sarkar 2006; Sarathi et al. 2008; Wu et al. 2018). Therefore, it is desirable to understand better the processes and characteristics of local scour to ensure streambed stability and the safety of the nearby hydraulic structures, and thus it is of primary importance for researchers to propose better research methodologies or numerical models.

Many different methods can be used to study local scour problems. Despite scale effects, experimental or physical modeling works are reliable. However, these methods are quite expensive, especially when various cases are under investigation, and difficult when detailed measurements of temporal variations in the flow fields and bed elevations are required. For example, acoustic Doppler velocimetry (ADV) can record instantaneous velocity components, but it only measures data at a single point, or multiple points along a single line, and the flow may be disturbed if multiple ADVs are used simultaneously. Particle image velocimetry (PIV) and particle tracking velocimetry (PTV) can produce high–resolution instantaneous velocity fields (Cooper et al. 2013; Tomas et al. 2018), but their application in sediment transport problems is difficult because the results are based on suitable tracer particles, which may be significantly impacted by sediment particles. Complementing laboratory approaches, computational fluid dynamics (CFD) modeling has been a topic of significant research interest in recent years because sediment scour and deposition phenomena can be efficiently simulated (Khosronejad et al. 2007; Sumer

2014; Langendoen et al 2016). Although many numerical models have been developed for sediment scour problems, it is still necessary to develop different models with a high degree of accuracy, efficiency and versatility to achieve different potential objectives.

There are two interfaces in local scour problems: the water-air and fluid-sediment interfaces. The dynamic location of interfaces is typically identified using either “interface–capturing” or “interface–tracking” techniques. A schematic plot of the two methods are shown in Figure 1.1. In an interface–capturing method, the computations are carried out on a non–moving mesh, where an interface or fraction function is solved to “capture” or implicitly describe the interface. In an interface–tracking method, the computational grids are moved or deformed with the flow field to “track” or explicitly describe the surface (Charin et al. 2017). These two approaches both have advantages and disadvantages specific to the nature of the applications and should be selected properly. Locating the water-sediment interaction is more complicated. Many previous multi–phase models employed interface–capturing techniques to model the streambed evolution (Amoudry and Liu 2009; Lee et al. 2016; Cheng et al. 2017; Lee et al. 2017). The immersed boundary method is also a very promising interface-capturing approach, which first locates an immersed boundary in a fixed background mesh, and then incorporates the impacts of the boundary on the flow field (Khosronejad 2011). These interface–capturing models do not require re–meshing, so they are usually less computationally expensive and more numerically stable than interface–tracking models, especially for complex applications.

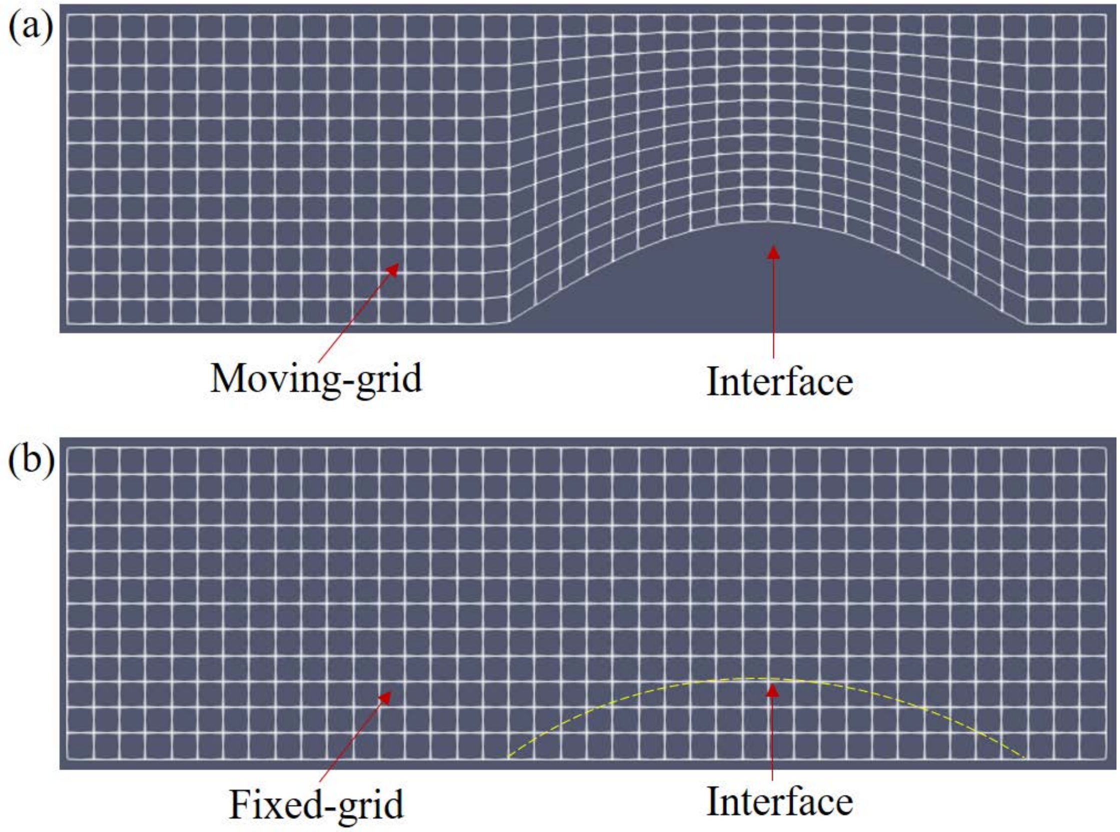

Figure 1.1 Schematic of the interface–tracking and interface–capturing methods: (a) interface-tracking method (the computational grids are moved or deformed with the flow field to “track” or explicitly describe the interface); and (b) interface-capturing method (the computations are carried out on a non–moving mesh, where an interface or fraction function is solved to “capture” or implicitly describe the interface).

Numerous researchers have applied interface–tracking techniques to simulate the phenomenon of sediment bed scour and deposition (Apsley and Stansby 2008; Liu and García 2008; Zhao et al. 2010; Marsooli and Wu 2014). These models can explicitly represent the fluid–sediment interface and thus yield more accurate results than interface–capturing models, but they may require time–consuming grid updates and severely deteriorate the mesh quality in cases with complex geometries.

A major factor hindering the wide spread use of Lagrangian interface-tracking (moving-mesh) models is the problem of mesh failure. A typical moving-mesh approach in a finite volume model is to solve a mesh motion equation at the cell centers and then interpolate the values to the vertices to perform the mesh motion. For simple and small boundary deformation, the method works very well. However, for cases with more complicated or larger mesh deformation, the grids at different levels may intersect each other, generating negative grid volume, and causing the simulation to be unstable. An example of this problem is shown in Figure 1.2; the boundary patch downstream of the cell C_L is moving upwards at a constant velocity of U_B, while the one upstream of C_L is stationary.

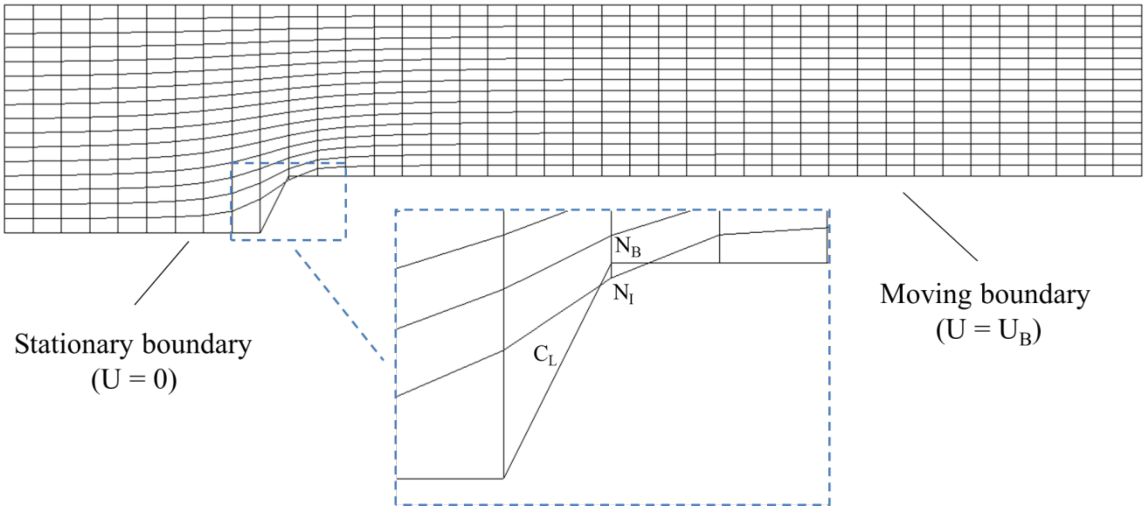

Figure 1.2 Sketch of a typical deforming-mesh problem. An internal level intersects the bathymetry which causes the simulation to fail.

Using the typical mesh motion solvers available in OpenFOAM, the solved motion velocity of the internal node, N_I, is much smaller than the motion velocity of the boundary node, N_B, which moves at the same speed as the boundary. Eventually, an internal level intersects the bathymetry which causes the simulation to fail. This is a very common and serious problem of the interface-tracking approach, which has been troubling the community for many years and has significantly hindered its wider use. In recent years, many sediment scour models of other types have been developed (Amoudry and Liu 2009; Khosronejad et al. 2011; Lee et al. 2016; Cheng et al. 2017; Lee et al. 2017), but it is still meaningful to improve the practice of the moving-mesh method. It has more advantages than interface-capturing methods regarding the mass conservation and discontinuities across the interface, is less sensitive to the size of computational grids around the interface, and can produce more accurate results at comparable levels of mesh resolution (Watts et al. 2005; Tezduyar 2006; Mirjalili et al. 2017). Therefore, it is quite beneficial and urgent to propose a new code that can ensure efficiency and mesh quality in a more practical and reliable way.

In addition to the mesh failure issue explained above, modeling flow and local scour adjacent to a static rigid object, such as a pipeline or a submerged weir, is often challenging and requires further investigation. Both of the traditional moving-mesh and fixed-grid methods have inherent advantages and disadvantages specific to the nature of these applications (sediment scour near a structure). Therefore, it is also necessary to implement and validate a novel numerical model for flow and sediment scour phenomena that combines the best properties of the moving-mesh and fixed-grid methods.

1.2 Objectives of the Study

The primary objective of this study is to implement a sediment scour module in OpenFOAM and apply it to local scour problems. The proposed module is expected to have the novel advantage of allowing for more severe topographic variations and complicated geometries, can combine the best properties of the traditional moving-mesh and fixed-grid methods, and can provide more reliable predictions for the key characteristics and evolution of the bed profiles in sediment scour problems.

The primary objective of the first part of the present study (Chapter 3) is to implement and validate a new sediment-scour module in OpenFOAM that uses a strict vertex-based, terrain conformal, moving-mesh technique. A total of six additional models using the conventional moving-mesh techniques available in OpenFOAM have also been implemented. The results for a simple case of prescribed boundary motion show that the proposed module has the novel advantage of allowing for more severe topographic variations. To evaluate the accuracy of model predictions, the experiment by Chatterjee et al. (1994) was simulated using the implemented model. The comparisons with the experimental and previous numerical results demonstrate that the present model can provide promising predictions for sediment-scour problems compared with the current modeling practice. To gain more confidence in the implementation and provide more insight, a new laboratory experiment was conducted and simulated using the implemented model; the good agreement between the experimental and numerical results confirmed that the model can be used as a reliable tool to simulate local scour problems due to submerged wall jets. Furthermore, various turbulence modeling approaches and bedload equations are also evaluated to improve the practice of modeling wall jet scour.

The primary objective of the second part of the present research (Chapter 4) was to implement and validate a novel numerical model for flow and sediment scour phenomena that combined the best properties of the boundary-fitted-grid and fixed-grid methods; i.e., a model that was capable of directly tracking the moving fluid-sediment interface using a very simple computational mesh setup. The present study was also motivated by a number of practical reasons. For example, preliminary studies have found that employing a purely fixed-bed method for sediment scour problems requires the modeller to estimate accurately the maximum scour depth prior to the simulations; if not, the computational domain will be too large or too small because the physical domain varies with time. The new model performs mesh motions for bed conforming without considering the pipeline, and then simulates the pipeline with a fixed-grid approach (using masked elements) after the mesh motion has been completed. To the best of the authors' knowledge, the numerical modeling of flow and local scour using moving mesh with masked elements in OpenFOAM has not been previously reported. The phenomena of flow and local scour around a pipeline in a steady current was chosen here because this is very important in a wide range of industrial applications, and has been commonly used for validating numerical models.

The third part of this study (Chapter 5) aimed to further apply the improved moving-mesh approach proposed in the second part of this study to implement a numerical model that could simulate the transient local scour process near a hydraulic structure, such as a submerged weir with a downstream slope. In the implemented model, the fluid-sediment interface is tracked using a moving-mesh technique, and the effects of the structure on the hydrodynamics and bed morphology are resolved using a masked-element technique. Compared to traditional sediment scour models, based on the moving-mesh technique, the present model has the advantage of allowing for a simpler setup of the computational grids and a larger-amplitude deformation, and is thus more effective and efficient for practical engineering applications. Furthermore, the effects of various parameters and configurations, such as the roughness height estimation, angle of repose, turbulence model, stochastic model, critical Shields number, and a second sand-slide model, on the numerical predictions have also been studied. To the best of the authors' knowledge, numerical modeling of local scour caused by submerged weirs with a downstream slope, has not previously been reported.

The fourth part of this study (Chapter 6) aimed to provide some additional results and discussions.

1) First, the best performing modules and algorithms proposed in the first part were further applied to investigate the effects of the gate opening, apron length, and tailgate height on the transient local scouring processes due to submerged wall jets in the early stages, and some regression formulas are proposed. This section provides some new observations that have not been adequately handled in the literature and an example of how to apply the validated model to conduct further investigations.

2) Second, the flow field around a pipeline near a scoured bed for five different cases were conducted using the masked-element model, and the modelled results were compared to published laboratory measurements as well as to previous numerical predictions obtained by other models. The results show that the proposed model satisfactorily reproduces the features of the flow observed in the experiments, and thus can be a promising tool.

3) Third, the mesh configurations and the improvement have been briefly discussed.

The current study focuses on 2D cases because it aims to develop and validate the modeling approach. The experiments used for model validation were found to be 2D, so conducting 2D simulations is reasonable and correct in terms of reproducing the experimental conditions. It only considers non-cohesive soil, and cohesive soil is not within the research scope.

1.3 Novelty and contributions

The major novel aspects and contributions of this study are summarized as follows:

1) This study presents the implementation and validation of a new sediment-scour model with a strict vertex-based terrain conformal moving-mesh technique within the framework of OpenFOAM. The proposed simple moving-mesh technique in OpenFOAM is implemented to overcome the shortcomings of the conventional automatic mesh-motion techniques in handling large-amplitude moving geometries. The model is employed to simulate a simple case of prescribed boundary motion, a previous experiment in the literature, and a new laboratory

experiment for local scour due to submerged wall jets. The results are compared with both the experimental and other numerical results. The comparisons demonstrate that the present model has the novel advantage of allowing for more severe topographic variations, and can provide more reliable predictions for the key characteristics and evolution of the bed profiles in wall jet scour problems. To the best of the author's knowledge, numerical modeling of local scour due to submerged wall jets using a strict vertex-based, terrain conformal, moving-mesh technique in OpenFOAM has not been previously reported.

2) This study also extends the implemented model to simulate cases in which there is an embedded structure (here, a pipeline). In contrast to previous moving-mesh models, the newly implemented model uses masked elements to resolve the effects of the stationary object on the flow and sediment scour processes. This approach makes it possible to track directly the moving fluid-sediment interface using a very simple mesh setup, which is more practical for engineering computations than the existing models. To the best of the authors' knowledge, numerical modeling of local scour around a pipeline in steady currents using moving mesh with masked elements has not been previously reported.

3) This study applied the implemented model to simulate local scour at submerged weirs with downstream slopes. In the model, the fluid-sediment interface is tracked using a moving-mesh technique, and the effects of the structure on the hydrodynamics and bed morphology are resolved using a masked-element technique. Compared to traditional sediment scour models, based on the moving-

mesh technique, the present model has the advantage of allowing for a simpler setup of the computational grids and a larger-amplitude deformation. Laboratory experiments on local scour at a submerged weir with a downstream slope were conducted, which provided bed profiles at different time instants. The results obtained by the present model are compared to the experimental data. The comparisons demonstrate the performance of the model in satisfactorily predicting local scour at a submerged weir with a downstream slope. To the best of the authors' knowledge, numerical modeling of local scour at a submerged weir with a downstream slope has not been previously reported.

4) As applications, the present model was further applied to investigate the effects of a few parameters on the transient scouring processes in the early stages. These studies not only made contributions to the knowledge regarding sediment scour problems but also demonstrated how the present model would be useful in engineering practice.

5) Two sets of laboratory experiments have been conducted, which can be used in future studies for validating numerical models.

1.4 Thesis structure

This thesis is organized as follows:

1) Chapter 1: introduction.

2) Chapter 2: a literature review. The literature reviewed for this research focused on the governing equations, turbulence models, sediment scour equations, previous

models based on the moving-mesh approach, and previous models based on the fixed-grid approach.

3) Chapter 3: a journal paper entitled "Numerical modeling of local scour due to submerged wall jets using a strict vertex-based, terrain conformal, moving-mesh technique in OpenFOAM". This paper has been published in the *International Journal of Sediment Research*. A part of this chapter has also been presented and published at the *38th IAHR World Congress*.

4) Chapter 4: a journal paper entitled "Numerical modeling of flow and local scour around a pipeline in steady currents using moving mesh with masked elements". This paper has been published in the *Journal of Hydraulic Engineering*. A part of the work was presented at the Ontario and Quebec Hydraulics Research Student Symposium (2019).

5) Chapter 5: a journal paper entitled "Numerical modeling of local scour at a submerged weir with a downstream slope using a coupled moving-mesh and masked-element approach". This paper has been accepted by the *International Journal of Sediment Research*.

6) Chapter 6: this chapter provides some additional results and discussions

    - Section 5.1: an additional study entitled "applications of the wall jet scour model"

    - Section 5.2: an additional study entitled "flow around a pipeline near a scoured bed"

- Section 5.3: an additional discussion about the mesh configurations and improvement.

- Section 5.4: some additional figures.

7) Chapter 7: summary and conclusions.

Chapter 2 Literature review

It is important to model the processes of local scour to ensure streambed stability and the safety of the nearby hydraulic structures. This chapter presents the relevant hydrodynamic equations, bed morphology equations, and some previous models. In terms of hydrodynamic equations, the governing equations, the equation for the volume–of–fluid (VOF) method, and the turbulence models are summarized. In terms of bed morphology equations, the sediment continuity equation and some sediment transport formulas based on different approaches are presented. The previous sediment scour models are classified into two categories, moving-mesh and fixed-grid, and some of them are introduced and discussed in this chapter.

2.1 Hydrodynamic equations

The proposed model has been implemented on the basis of the solver "interDyMFoam" in OpenFOAM. The solver solves the three–dimensional Reynolds–Averaged Navier–Stokes equations (RANS) for incompressible flows. The general form of the equations can be expressed as

Continuity:

$$\frac{\partial}{\partial x}\left(u_x\right)+\frac{\partial}{\partial y}\left(u_y\right)+\frac{\partial}{\partial z}\left(u_z\right)=0 \tag{2.1}$$

Momentum in the *x*-direction:

$$\frac{\partial\left(\rho u_x\right)}{\partial t}+\frac{\partial}{\partial x}\left(\rho u_x u_x\right)+\frac{\partial}{\partial y}\left(\rho u_y u_x\right)+\frac{\partial}{\partial z}\left(\rho u_z u_x\right)=-\frac{\partial p}{\partial x}+\frac{\partial \tau_{xx}}{\partial x}+\frac{\partial \tau_{yx}}{\partial y}+\frac{\partial \tau_{zx}}{\partial z}+\rho g_x \tag{2.2}$$

Momentum in the *y*-direction:

$$\frac{\partial\left(\rho u_y\right)}{\partial t}+\frac{\partial}{\partial x}\left(\rho u_x u_y\right)+\frac{\partial}{\partial y}\left(\rho u_y u_y\right)+\frac{\partial}{\partial z}\left(\rho u_z u_y\right)=-\frac{\partial p}{\partial y}+\frac{\partial \tau_{xy}}{\partial x}+\frac{\partial \tau_{yy}}{\partial y}+\frac{\partial \tau_{zy}}{\partial z}+\rho g_y \qquad (2.3)$$

Momentum in the *z*-direction:

$$\frac{\partial\left(\rho u_z\right)}{\partial t}+\frac{\partial}{\partial x}\left(\rho u_x u_z\right)+\frac{\partial}{\partial y}\left(\rho u_y u_z\right)+\frac{\partial}{\partial z}\left(\rho u_z u_z\right)=-\frac{\partial p}{\partial z}+\frac{\partial \tau_{xz}}{\partial x}+\frac{\partial \tau_{yz}}{\partial y}+\frac{\partial \tau_{zz}}{\partial z}+\rho g_z \qquad (2.4)$$

where ρ is the density; t is the time, u_x, u_y, and u_z are the velocity components in the x, y, and z directions respectively; p is the pressure; τ_{ij} denotes a stress in the j-direction exerted on a plane perpendicular to the i-axis; g_x, g_y, and g_z are the gravitational acceleration components in the x, y, and z directions respectively (Wendt et al. 2008).

OpenFOAM uses algebraic tensor operations, and the expressions in OpenFOAM can be written as

$$\nabla\cdot\mathbf{U}=0 \qquad (2.5)$$

$$\frac{\partial\rho\mathbf{U}}{\partial t}+\nabla\cdot\left(\rho\mathbf{U}\mathbf{U}\right)=\nabla\cdot\mathbf{T}+\rho\mathbf{g}-\nabla p \qquad (2.6)$$

where $\mathbf{U}$ is the flow velocity vector; ρ is the density; t is the time; $\mathbf{T}$ is the viscous stresses tensor; $\mathbf{g}$ is the gravitational acceleration vector; and p is the pressure.

The water–air interface is often represented by a zero–shear stationary boundary or a frictionless slip rigid lid. Amoudry and Liu (2009) developed a two–phase granular sediment transport model that solves concentration–weighted averaged equations of motion for both fluid and sediment phases and applied the model to studies on scouring downstream of an apron; they assumed the top boundary to be a symmetry boundary and applied the zero–gradient condition to all variables. Lee et al. (2016) developed a multi–dimensional, rheology–based, two–phase model for sediment transport in OpenFOAM and applied the model to problems concerning sheet flow and scour under a pipeline; they imposed a wall function at the top boundary and set at zero the shear stresses for both phases and fluxes of turbulent kinetic energy and dissipation. Cheng et al. (2017) proposed a multi–dimensional, Eulerian, two–phase sediment transport model (in OpenFOAM) with applications to sheet flows and scouring downstream of an apron; similar to the above, the dynamic shape of the water–air interface was not considered in their study. These zero–shear boundary or rigid lid approaches ignore the free surface motions and thus can simplify the modeling equations and avoid limitations on computational time steps. However, the existence of hydraulic structures in many applications usually result in rapid and large–scale water surface changes, especially at the early stages, which can in turn substantially impact the internal flow and water–sediment interaction, so the errors due to these assumptions may reduce model reliability. Therefore, it is necessary to locate the water-air interface, and thus the major tasks for modeling local scour problems include locating both the water–air and fluid–sediment interfaces.

The free water surface can be properly handled by a variety of interface-capturing approaches, among which the volume–of–fluid (VOF) method is widely used. The VOF method is a free–surface modeling technique that locates the fluid–fluid surface based on the idea of a so–called fraction function, which is used as an indicator for determining whether a cell is occupied by one certain fluid or a mixture of the two fluids. Liu and García (2008) constructed a local sediment scour model (in OpenFOAM) with free water surface and mesh deformation; in their study, they utilized a high resolution VOF method proposed by Ubbink and Issa (1999) to identify the water–air interface. Recently, Lee et al. (2017) developed a new rheology–based, three–phase sediment transport model in OpenFOAM and employed it to predict the local scour due to a submerged wall jet; in their study, a VOF method was proposed and successfully employed to identify the evolving water–air interface in the presence of suspended sediment.

In the VOF phase–fraction–based approach, a fraction function, α, is defined as the volume fraction of water in each computational cell. If the value of α is 0, the cell is occupied by air alone; if α is 1, the cell is filled with water; if α is between 0 and 1, the cell is bisected by the free water surface. The properties of the two–phase flow can be determined based on the fraction function; for example, the velocity $\mathbf{U}$, density ρ and dynamic viscosity μ of the mixed flow are determined by

$$\mathbf{U} = \alpha \mathbf{U}_w + (1-\alpha)\mathbf{U}_a \tag{2.7}$$

$$\rho = \alpha \rho_w + (1-\alpha)\rho_a \tag{2.8}$$

$$\mu = \alpha \mu_w + (1-\alpha)\mu_a \tag{2.9}$$

where $\mathbf{U}_w$ and $\mathbf{U}_a$ are the velocities of the water and air phases; ρ_w and ρ_a are the densities of the water and air phases; μ is the dynamic viscosity of the mixed flow; μ_w and μ_a are the dynamic viscosities of the water and air phases.

The standard transport equation for α is expressed as (Hirt and Nichols 1981):

$$\frac{\partial \alpha}{\partial t} + \nabla \cdot \left(\mathbf{U} \alpha \right) = 0 \tag{2.10}$$

An artificial compression term is introduced into the standard fraction function equation to solve the problems associated with the convection of a step function, so the final transport equation for α used in the present studies is given by (Rusche 2002)

$$\frac{\partial \alpha}{\partial t} + \nabla \cdot \left(\mathbf{U} \alpha \right) + \nabla \cdot \left(\mathbf{U_r} \alpha \left(1 - \alpha \right) \right) = 0 \tag{2.11}$$

where $\mathbf{U_r}$ is the relative velocity vector, an artificial velocity field used to compress the interface.

As for turbulence modelling, various techniques can be used, such as the direct numerical simulation (DNS), large eddy simulations (LES), or the Reynolds-Averaged Navier-Stokes (RANS) approach. Widespread application of DNS and LES approaches for sediment scour is still not feasible for many practical cases because of the heavy computational cost; thus, studies on the practice of RANS simulations are still quite meaningful in the field of hydraulic and environmental engineering. Therefore, this section focuses on the five most widely used RANS turbulence models (the standard *k-ε*, Re-Normalisation Group (RNG) *k-ε*, Realizable *k-ε*, *k-ω*, and *k-ω* SST). These equations can be expressed in different forms, and the expressions used in OpenFOAM are presented as follows.

The standard *k–ε* model:

$$\frac{\partial k}{\partial t} + \frac{\partial k u_i}{\partial x_i} - \frac{\partial}{\partial x_i}\left(D_{keff} \frac{\partial k}{\partial x_i} \right) = G - \varepsilon \tag{2.12}$$

$$\frac{\partial \varepsilon}{\partial t}+\frac{\partial \varepsilon u_i}{\partial x_i}-\frac{\partial}{\partial x_i}\left(D_{\varepsilon eff}\frac{\partial \varepsilon}{\partial x_i}\right)=c_{1\varepsilon}\frac{\varepsilon}{k}G-c_{2\varepsilon}\frac{\varepsilon^2}{k} \tag{2.13}$$

$$D_{keff}=\nu_t+\nu \tag{2.14}$$

$$D_{\varepsilon eff}=\frac{\nu_t}{\sigma_\varepsilon}+\nu \tag{2.15}$$

$$\nu_t=c_\mu\frac{k^2}{\varepsilon} \tag{2.16}$$

$$G=2\nu_t S_{ij}S_{ij} \tag{2.17}$$

$$S_{ij}=\frac{1}{2}\left(\frac{\partial u_j}{\partial x_i}+\frac{\partial u_i}{\partial x_j}\right) \tag{2.18}$$

where k is the turbulent kinetic energy; ε is the turbulent energy dissipation rate; u_i is the instantaneous velocity component in the direction x_i; D_{keff} and $D_{\varepsilon eff}$ are the effective diffusivity for k and ε, respectively; ν_t is the turbulent kinematic viscosity; ν is the kinematic viscosity; G is the production of turbulence due to shear; S_{ij} is the strain-rate tensor; *dev* denotes the deviatoric component; Ω_{ij} is the vorticity (spin) tensor;σ_ε, $c_{1\varepsilon}$, $c_{2\varepsilon}$, c_μ are model constants equal to 1.3, 1.44, 1.92, and 0.09, respectively.

The RNG k–ε model:

$$\frac{\partial k}{\partial t}+\frac{\partial k u_i}{\partial x_i}-\frac{\partial}{\partial x_i}\left(D_{keff}\frac{\partial k}{\partial x_i}\right)=G-\varepsilon \tag{2.19}$$

$$\frac{\partial \varepsilon}{\partial t}+\frac{\partial \varepsilon u_i}{\partial x_i}-\frac{\partial}{\partial x_i}\left(D_{\varepsilon eff}\frac{\partial \varepsilon}{\partial x_i}\right)=\left(c_{1\varepsilon}-R_\varepsilon\right)\frac{\varepsilon}{k}G-c_{2\varepsilon}\frac{\varepsilon^2}{k} \tag{2.20}$$

$$D_{keff}=\frac{\nu_t}{\sigma_k}+\nu \tag{2.21}$$

$$D_{\varepsilon eff} = \frac{\nu_t}{\sigma_\varepsilon} + \nu \tag{2.22}$$

$$\nu_t = c_\mu \frac{k^2}{\varepsilon} \tag{2.23}$$

$$G = \nu_t S_2 \tag{2.24}$$

$$S_2 = 2 S_{ij} S_{ij} \tag{2.25}$$

$$S_{ij} = \frac{1}{2}\left(\frac{\partial u_j}{\partial x_i} + \frac{\partial u_i}{\partial x_j} \right) \tag{2.26}$$

$$R_\varepsilon = \frac{\eta\left(1 - \eta/\eta_0\right)}{1 + \beta \eta^3} \tag{2.27}$$

$$\eta = \sqrt{S_2}\,\frac{k}{\varepsilon} \tag{2.28}$$

where σ_k, σ_ε, $c_{1\varepsilon}$, $c_{2\varepsilon}$, c_μ, η_0, and β are model constants equal to 0.71942, 0.71942, 1.42, 1.68, 0.0845, and 0.012 respectively.

The Realizable k–ε model:

$$\frac{\partial k}{\partial t} + \frac{\partial k u_i}{\partial x_i} - \frac{\partial}{\partial x_i}\left(D_{keff} \frac{\partial k}{\partial x_i} \right) = G - \varepsilon \tag{2.29}$$

$$\frac{\partial \varepsilon}{\partial t} + \frac{\partial \varepsilon u_i}{\partial x_i} - \frac{\partial}{\partial x_i}\left(D_{\varepsilon eff} \frac{\partial \varepsilon}{\partial x_i} \right) = \sqrt{2} c_{1\varepsilon} S_{ij} \varepsilon - c_{2\varepsilon} \frac{\varepsilon^2}{k + \sqrt{\nu \varepsilon}} \tag{2.30}$$

$$D_{keff} = \frac{\nu_t}{\sigma_k} + \nu \tag{2.31}$$

$$D_{\varepsilon eff} = \frac{\nu_t}{\sigma_\varepsilon} + \nu \tag{2.32}$$

$$\nu_t = C_{\mu r} \frac{k^2}{\varepsilon} \tag{2.33}$$

$$C_{\mu r} = \frac{1}{A_0 + A_s U_s \frac{k}{\varepsilon}} \tag{2.34}$$

$$A_s = \sqrt{6} \cos \varphi_s \tag{2.35}$$

$$\varphi_s = \frac{1}{3} \arccos \left\{ \min \left[\max \left(\sqrt{6} W, -1 \right), 1 \right] \right\} \tag{2.36}$$

$$W = \frac{2\sqrt{2} S_{ij} S_{jk} S_{ki}}{S_{mag} S_2} \tag{2.37}$$

$$S_{mag} = \sqrt{S_2} \tag{2.38}$$

$$S_2 = 2 \left(dev \left(S_{ij} \right) \right)^2 \tag{2.39}$$

$$S_{ij} = \frac{1}{2} \left(\frac{\partial u_j}{\partial x_i} + \frac{\partial u_i}{\partial x_j} \right) \tag{2.40}$$

$$U_s = \sqrt{\frac{S_2}{2} + \Omega_{ij} \Omega_{ij}} \tag{2.41}$$

$$\Omega_{ij} = \frac{1}{2} \left(\frac{\partial u_j}{\partial x_i} - \frac{\partial u_i}{\partial x_j} \right) \tag{2.42}$$

$$G = \nu_t S_2 \tag{2.43}$$

$$c_{1\varepsilon} = \max \left(\frac{\eta}{5 + \eta}, 0.43 \right) \tag{2.44}$$

$$\eta = S_{mag} \frac{k}{\varepsilon} \tag{2.45}$$

where σ_k, σ_ε, A_0, $c_{2\varepsilon}$ are model constants equal to 1, 1.2, 4, and 1.9 respectively.

The *k*– *ω* model:

$$\frac{\partial k}{\partial t}+\frac{\partial k u_i}{\partial x_i}-\frac{\partial}{\partial x_i}\left(D_{keff}\frac{\partial k}{\partial x_i}\right)=G-c_\mu k\omega \tag{2.46}$$

$$\frac{\partial \omega}{\partial t}+\frac{\partial \omega u_i}{\partial x_i}-\frac{\partial}{\partial x_i}\left(D_{\omega eff}\frac{\partial \omega}{\partial x_i}\right)=\alpha_{k\omega}G\frac{\omega}{k}-\beta\omega^2 \tag{2.47}$$

$$D_{keff}=\alpha_k\nu_t+\nu \tag{2.48}$$

$$D_{\omega eff}=\alpha_\omega\nu_t+\nu \tag{2.49}$$

$$\nu_t=\frac{k}{\omega} \tag{2.50}$$

$$G=2\nu_t S_{ij}S_{ij} \tag{2.51}$$

$$S_{ij}=\frac{1}{2}\left(\frac{\partial u_j}{\partial x_i}+\frac{\partial u_i}{\partial x_j}\right) \tag{2.52}$$

where ω is the specific dissipation rate; c_μ, α_k, α_ω, $\alpha_{k\omega}$, β are model constants equal to 0.09, 0.5, 0.5, 0.52 and 0.072 respectively.

The *k*– *ω* SST model:

$$\frac{\partial k}{\partial t}+\frac{\partial k u_i}{\partial x_i}-\frac{\partial}{\partial x_i}\left(D_{keffi}\frac{\partial k}{\partial x_i}\right)=\min\left(G,c_1\beta^* k\omega\right)-\beta^* k\omega \tag{2.53}$$

$$\begin{aligned}\frac{\partial \omega}{\partial t}+\frac{\partial \omega u_i}{\partial x_i}-\frac{\partial}{\partial x_i}\left(D_{\omega eff}\frac{\partial \omega}{\partial x_i}\right)=\gamma_i \min\left[S_2,\frac{c_1}{a_1}\beta^*\omega\max\left(a_1\omega,b_1F_{23}\sqrt{S_2}\right)\right]\\ -\beta\omega^2-\left(F_1-1\right)CD_{k\omega}\end{aligned} \tag{2.54}$$

$$D_{keff}=\alpha_{ki}\nu_t+\nu \tag{2.55}$$

$$D_{\omega effi}=\alpha_{\omega i}\nu_t+\nu \tag{2.56}$$

$$\nu_t = \frac{a_1 k}{\max\left(a_1\omega, b_1 F_{23}\sqrt{S_2}\right)} \tag{2.57}$$

$$S_2 = 2S_{ij}S_{ij} \tag{2.58}$$

$$S_{ij} = \frac{1}{2}\left(\frac{\partial u_j}{\partial x_i} + \frac{\partial u_i}{\partial x_j}\right) \tag{2.59}$$

$$G = 2\nu_t S_{ij} S_{ij} \tag{2.60}$$

$$CD_{k\omega} = 2\alpha_{\omega 2}\frac{\partial k}{\partial x_i}\frac{\partial \omega}{\partial x_i}\frac{1}{\omega} \tag{2.61}$$

where the subscript *i* can be either 1 or 2, depending on the blending functions in the model. α_{k1}, α_{k2}, $\alpha_{\omega 1}$, $\alpha_{\omega 2}$, α_1, b_1, c_1, β^*, γ_1, γ_2, are model constants equal to 0.85, 1, 0.5, 0.856, 0.31, 1, 10, 0.09, 5/9, 0.44. F_1 and F_{23} are blending functions.

2.2 Bed morphology equations

Bed elevation changes can be modelled using a bed morphology model, a classic one is the so-called Exner equation. The Exner equation describes the sediment continuity, which can be expressed as:

$$\frac{\partial \eta}{\partial t} = \frac{1}{1-n}\left[-\nabla \cdot \vec{q}_b + D - E\right] \tag{2.62}$$

where η is bed elevation; t is time; n is porosity of the bed; $\vec{q}_b$ is bed-load transport rate; D is deposition rate; E is entrainment rate.

The suspended load can be modelled using a standard convection diffusion equation:

$$\frac{\partial c}{\partial t} + \nabla \cdot \left(\vec{u} - v_s \frac{\vec{g}}{|g|} \right) c = \nabla \cdot \left(\nu_t \nabla c \right) \tag{2.63}$$

where c is sediment concentration; $\vec{u}$ is fluid velocity vector; v_s is sediment fall velocity; g is gravitational acceleration; ν_t is diffusivity which is taken as the same value as turbulence eddy viscosity.

To calculate the bed-load transport rate, numerous formulas have been proposed, and the subsequent sub-sections will classify these formulas into different categories based on their theoretical bases and provide details of these formulas.

2.2.1 Classification of the sediment transport formulas

Many different sediment transport formulas have been proposed and the principle difference among them is the method of bed-load transport rate simulation. Meng et al. (2016) classified all the formulas into two categories: empirical or semi-empirical; the author stated that the empirical formulas were based purely on regressive analysis of measured data, such as Meyer-Peter and Müller (1948), Parker (1978), and Knack and Shen (2015); semi-empirical formulas involve both theoretical derivations and statistical analysis, such as Bagnold (1973), Engelund and Fredsoe (1976), and Zhong et al. (2012). However, it is controversial to claim a formula is purely based on regressive analysis; for example, the Meyer-Peter and Müller (1948) formula indeed employed the shear stress theory to derive its basic form although the coefficients were mostly determined by regression analyses. Therefore, it is easier to categorize the formulas based on their theoretical bases; the present study classifies all the formulas into four different categories:

- Formulas based on the shear stress approach
- Formulas based on the probabilistic approach
- Formulas based on the stream power approach
- Formulas based on the discharge approach

In the rest of the section, these approaches and some representative formulas will be described.

2.2.2 Formulas based on the shear stress approach

The shear stress approach uses a concept of critical shear stress; namely, if the actual shear stress exceeds the critical shear stress, then erosion will occur, and the bedload rate is a function of the difference between the actual and critical shear stress. The formulas based on the shear stress approach include Meyer-Peter and Müller (1948), van Rijn (1984), and Wong and Parker (2006) equations. One of the most widely used formulas based on the shear stress approach is the Meyer-Peter and Müller (1948) equation, the core equations of which can be expressed as:

$$q_b = \Phi\left[g\left(s-1\right)d^3\right]^{\frac{1}{2}} \tag{2.64}$$

$$\Phi = B\left(\theta-\theta_c\right)^{1.5} \tag{2.65}$$

$$\theta = \frac{\tau}{gd\left(\rho_s-\rho_f\right)} \tag{2.66}$$

$$\theta_c = \frac{\tau_c}{gd\left(\rho_s - \rho_f\right)} \tag{2.67}$$

where q_b is the bedload transport rate; Φ is the dimensionless form of the bedload transport rate; g is gravitational acceleration; s is the excess density; d is sediment diameter; B is bedload coefficient, which is generally 5.0 ~ 5.7 for low transport, around 8.0 for intermediate transport, and up to 13.0 for very high transport (Wei et al. 2014). θ is Shields parameter; θ_c is critical Shields parameter, which can be determined from the Soulsby-Whitehouse equation (Soulsby and Whitehouse, 1997); τ is shear stress; τ_c is critical shear stress; ρ_s is density of sediment; ρ_f is density of fluid.

A simplified version of the Meyer-Peter and Müller (1948) can be written as

$$\Phi = 8\left(\theta_i - \theta_c\right)^{3/2} \tag{2.68}$$

The Engelund and Fredsøe formula (1976) can be expressed as

$$\Phi = \begin{cases} 18.74\left(\theta_i - \theta_c\right)\left[\sqrt{\theta_i} - 0.7\sqrt{\theta_c}\right] & if \;\; \theta_i > \theta_c \\ 0 & if \;\; \theta_i \le \theta_c \end{cases} \tag{2.69}$$

The Nielsen formula (1992) is

$$\Phi = 12\theta_i^{1/2}\left(\theta_i - \theta_c\right) \tag{2.70}$$

The Camenen and Larson formula (2006) is

$$\Phi = 12\theta_i^{3/2}\exp\left(-4.5\frac{\theta_{cr}}{\theta}\right) \tag{2.71}$$

2.2.3 Formulas based on the probabilistic approach

The probabilistic approach estimates the sediment transport rate based on the fluctuations in the turbulent flow (Einstein 1950). The relatively complex model developed by Einstein was simplified (Brown 1950) by fitting data for non-dimensional bedload transport rate versus non-dimensional shear stress to yield the Einstein-Brown equation. Parker (1982) used a similar approach. The Einstein-Brown equation (Brown 1950) can be expressed as (López et al. 2014):

$$\varphi = \frac{g_b}{F_1 \rho_s \sqrt{g\left(S-1\right)d^3}} = \begin{cases} 2.15 \exp\left(\dfrac{-0.391}{\tau^*_{d_{50}}}\right) & \tau^*_{d_{50}} < 0.093 \\ 40\left(\tau^*_{d_{50}}\right)^3 & \tau^*_{d_{50}} \geq 0.093 \end{cases} \tag{2.72}$$

$$F_1 = \sqrt{\frac{2}{3} + \frac{36\nu^2}{gd^3\left(S-1\right)}} - \sqrt{\frac{36\nu^2}{gd^3\left(S-1\right)}} \tag{2.73}$$

$$\tau^*_{d_{50}} = \frac{\tau}{(\rho_s - \rho)gd_{50}} \tag{2.74}$$

where ν is fluid viscosity.

2.2.4 Formulas based on the stream power approach

The stream power approach estimates the sediment transport rate utilizing the stream power per unit bed area or the power available per unit weight of fluid (López et al. 2014). Examples of formulas based on the stream power approach include Bagnold (1973), Ackers (1993), and Yang (1984) equations. One of the most widely used formulas based on the stream power approach is the Bagnold (1980) equation, the core equations of which can be expressed as:

$$q_b = \frac{\rho_s}{\rho_s - \rho_f} q_{sr} \left[\frac{\omega - \omega_c}{(\omega - \omega_c)_r} \right]^{3/2} \left[\frac{y}{y_r} \right]^{-2/3} \left[\frac{D_{50}}{D_{50r}} \right]^{-1/2} \tag{2.75}$$

where q_{sr} is the reference transport rate, which is 0.1 kg/(m·s); ω is the stream power per unit bed area; ω_c is the critical unit stream power at the beginning of movement; $(\omega - \omega_c)_r$ is the reference excess stress power, which is 0.5 kg/(m·s); y is the mean flow depth; y_r is the reference stream depth, which is 0.1 m; D_{50} is the particle size for which 50% of the bed material is finer; D_{50r} is the reference particle size, which is 0.0011 m.

2.2.5 Formulas based on the discharge approach

The discharge approach employs critical water discharge as the criterion for determining particle entrainment and it uses some basic field parameters, such as river channel slope and sediment diameter (López et al. 2014). Examples of formulas based on the discharge approach include the Schoklitsch (1962) and the Bathurst (2007) equations. The Bathurst (2007) equation can be expressed as:

$$q_b = a\rho_f \left(q - q_{c2} \right) \tag{2.76}$$

$$a = 29.2 S_l^{1.5} \left(\frac{d_{50}}{d_{50s}} \right)^{-3.3} \tag{2.77}$$

$$q_{c2} = 0.5\left(0.0513 g^{0.5} d_{50}^{1.5} S_l^{-1.2} + 0.0133 g^{0.5} d_{84}^{1.5} S_l^{-1.23} \right) \tag{2.78}$$

where a is a dimensionless coefficient that represent the rate of change of bed load discharge with water mass discharge; q is the water discharge per unit width; q_{c2} is the threshold or critical water discharge per unit width for transport of material as the armor layer breaks up; S_l is channel slope; d_{50s} is the median diameter.

2.2.6 Selection of suitable formulas

The selection of sediment transport formulas has been a key research interest in hydraulic community in the past several decades. Gomez and Church (1989) tested 12 bed load sediment transport formulae developed for use in gravel bed channels using four sets of river data and three sets of flume data, covering a range of eight orders of magnitude in unit bed load transport rate. The tests revealed that no formula performed consistently well. The study concluded that the stream power equations should be used to estimate the magnitude of transport with limited information because this method provided the most straightforward scale correlation of the phenomenon; and a formula that is sensitive to bed state or grain size distribution should be selected when local hydraulic information is available. Nakato (1990) tested eleven existing sediment transport formulas against the field data measured at two United States Geological Survey gauging stations along the Sacramento River in California, where the bed-material ranges from fine sand to coarse gravel. The tests clearly demonstrated how difficult a task it is to predict sediment discharges in natural rivers as none of the formulas produced satisfactory results; therefore, the authors suggested hydraulic engineers develop the habit of looking up several sediment transport formulas and evaluating them on the basis of the field data before making their final choice. Haddadchi et al. (2013) rated 12 predictive bedload sediment transport equations against 14 sets of gravel-bed river field data collected by handheld bedload sampler in Narmab River, northeastern Iran. The authors stated that the results presented in their paper can be used to find the suitable bedload formula for a gravel bed river with a mild slope. Besides, the authors found that the Engelund and Hansen, Van Rijn and Einstein equations performed well with bed material grain size, while the equations of Shocklitsch, Meyer-Peter and Müller, and Frijlink yield the best results utilizing the bedload grain size. Mil-Homens et al. (2013) evaluated the predictive skill of three of the most commonly used bulk longshore sediment transport formulas using the most extensive longshore sediment transport data set. They improved the calibration coefficients in the three formulas using a least-squares optimization algorithm, resulting in a significant improvement in the predictive skill of all three formulas. Due to the calibration and improvement, the performance of all three improved formulas became very similar. López et al. (2014) tested the predictive power of 10 bed load formulas against bed load rates obtained for a regulated river, namely River Ebro, the armor layer of which is subject to repeated cycles of break-up and reestablishment. The results showed that the difference in performances of different formulas was significant. The formulae of Yang (1984) and Parker et al. (1982) presented the better levels of agreement with the observed bed load discharges in their study; however, there was no evident relationship between performance and theoretical approach. Sasal et al. (2009) developed an Artificial Neural Network (ANN) model for bedload estimation in alluvial rivers and the predictions were compared with those provided by the models of Parker et al. (1982), Bagnold (1980), and van Rijn (1984). The results showed that the ANN model significantly outperformed the traditional models. Kitsikoudis (2015) utilized machine learning techniques to evaluate the performance of various sediment transport approaches. A total of three machine learning techniques were employed, namely artificial neural networks, symbolic regression based on genetic programming and an adaptive-network-based fuzzy inference system. The machine learning techniques were used to derive sediment transport formulas from field and laboratory flume data based on different approaches, such as shear stress, stream power and unit stream power approaches. The results showed that each of these sediment transport quantification approaches had its own merit.

As can be concluded from the above review of literature, the topic of choosing a suitable sediment transport formula has been significantly studied during the past several decades; but unfortunately, almost no general accepted rule of formula selection has been drawn. There might be two major reasons for the difficulty in determining a suitable sediment transport formula: first, many of the sediment transport formula require calibration, so the performance of formulas would largely depend on the calibration technique, tolerance of errors, and data quality; second, the sediment transport mechanism is still far from well understood, so almost every existing sediment transport formulas has some assumptions, implying that the accuracy of a formula for a specific case is even random to a great degree. Since it is almost impossible to draw a general conclusion on the selection of suitable sediment transport formula at this stage, three suggestions are provided:

- it is necessary to conduct further investigations on developing or evaluating sediment transport formulas with the increase of knowledge about the mechanism of sediment transport phenomenon;

- the performances of different sediment transport formulas must be evaluated before applied to a certain case;
- and it might be a good measure to use the average results from different sediment transport formulas as the final results if no calibration data is available.

In the present project, the models based on the shear stress approach are employed because they are very straightforward in terms of their physical mechanisms. The numerical results are compared with experimental data to evaluate the performances of the adopted sediment transport formulas. In future studies, the other sediment transport models can be assessed and new sediment transport formulas can be developed.

2.3 Sediment scour models based on moving-grid methods

The existing sediment scour models can be generally classified into two categories, depending on the methodology used to identify the dynamic location of fluid-sediment interfaces: interface–tracking (moving-grid) and interface–capturing (fixed-grid) models (Charin et al., 2017). In this section, some well-known models based on moving-grid methods are reviewed. In a moving-grid method, the computational grids are moved or deformed with the flow field to “track” or explicitly describe the surface. It has more advantages than fixed-grid methods regarding the mass conservation and discontinuities across the interface, is less sensitive to the size of computational grids around the interface, and can produce more accurate results at comparable levels of mesh resolution (Watts et al. 2005; Tezduyar 2006; Mirjalili et al. 2017).

Brørs (1999) developed a numerical to simulate flow and scour at pipelines. The model solves the Reynolds-averaged equations for continuity and momentum and sediment continuity equation. A transport equation for the concentration of suspended load has also been incorporated in the model and the density effects on the mean flow and turbulence were considered. A sample computational mesh near the pipeline is shown in Figure 2.1. The simulations used different time steps for hydrodynamic and bed morphology calculations. The simulations first performed the hydrodynamic calculations for a number of time steps, then calculated the changes in bed elevations, and finally updated the sediment bed profile and initial grids. The model only moves the grids below the center of the pipeline. The points at the sediment bed only move vertically, and the initial mesh grids also move vertically according to the positions of the grids at the sediment bed in the same columns. The model was used to simulate the scour at a pipeline in steady flow, and the numerical results were found in good agreement with the experimental data reported by Mao (1986).

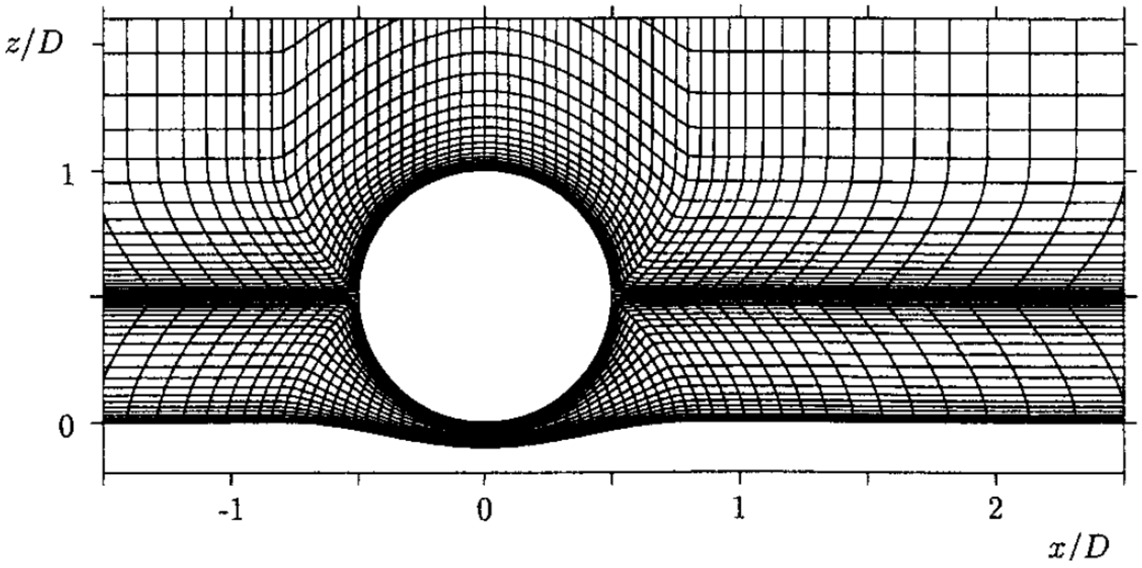

Figure 2.1 Computational mesh used in scour simulation. Detail of mesh (initial shape) close to pipeline (Brørs 1999)

Liang et al. (2005) presented a 2D numerical model for local scour below offshore pipelines in steady currents. The model solves the governing equations for hydrodynamics and sediment transport using a finite difference approach. The model uses a general curvilinear coordinate system. The study used boundary-fitted meshes, and sample meshes at different levels of resolution near the pipe are shown in Figure 2.2. The model performs simulations using the following procedure: 1) solve the governing equations for the flow and suspended load to obtain the hydrodynamic variables and suspended sediment concentration; 2) calculate the bed load and suspended load rates; 3) determine the bed profile based on the sediment continuity equation; 4) perform a sand-slide model; 5) move the initial grids according to the new bed profile; and 6) repeat the same steps for the subsequent calculations.

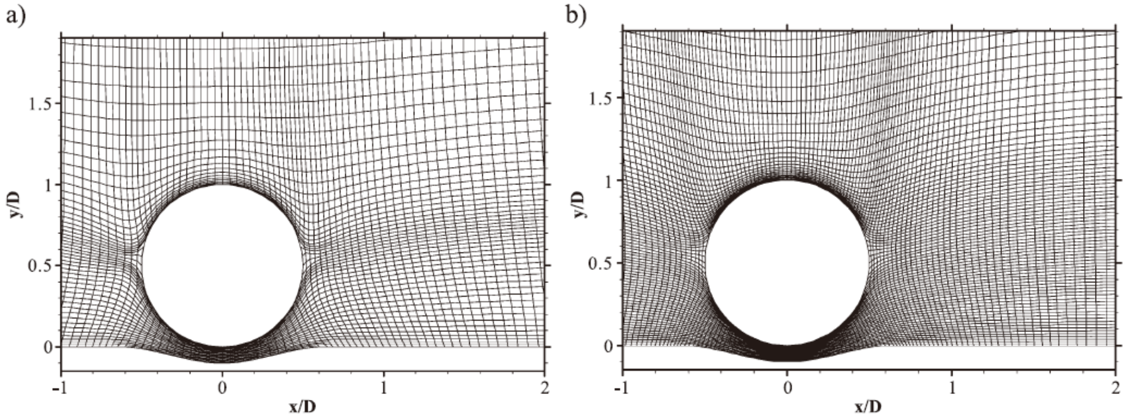

Figure 2.2 Local computational meshes near the pipe: (a) medium mesh; (b) fine mesh (Liang et al. 2005)

Liang et al. (2005) proposed new time marching schemes for hydrodynamic and bed morphology calculations to reduce the computational costs, as illustrated in Figure 2.3. The model uses a larger time step for bed morphology and a smaller time step for hydrodynamics because the time scale of the erosion process is typically larger than that of the flow process. The model performs several numbers of flow time steps, and then uses the results at the last time step to compute the bed changes. Liang et al. (2005) found that the influence of the time marching scheme became negligible after the number of time steps for hydrodynamics exceeded a critical number. The model has been validated against the experiment of net entrainment by van Rijn (1986), the zero entrainment test by Wang and Ribberink (1986), and the clear-water and live-bed scour experiments by Mao (1986). The results showed that the numerical model can reproduce the experimental measurements very well, with the standard k-ε turbulence model performing better than the Smagorinsky subgrid scale (SGS) model.

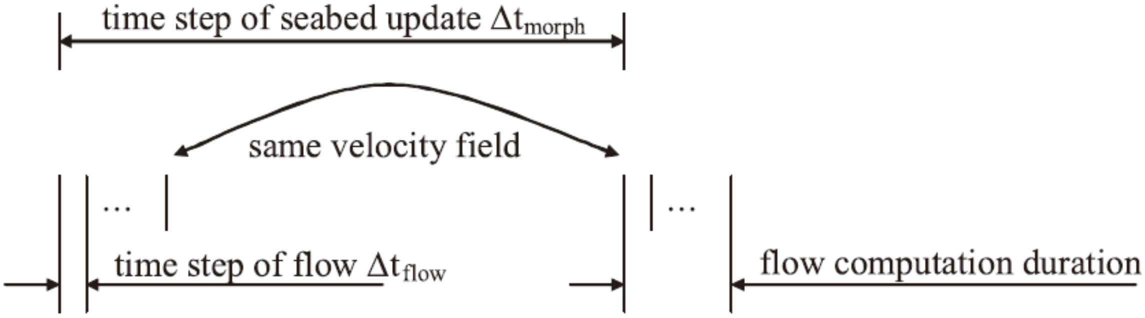

Figure 2.3 Illustration of time marching schemes for flow and scour updates (Liang et al. 2005)

Apsley and Stansby (2008) have implemented a sediment scour model within a RANS solver to simulate bed-load sediment transport on large slopes. For hydrodynamic simulations, they utilized the flow solver STREAM, which is a general-purpose finite volume RANS solve and can perform both 2D and 3D simulations. The flow simulation was coupled to the sediment continuity equation to simulate the bed motions. In their model, a finite-volume moving-mesh technique was used. As shown in Figure 2.4, the computational cells were defined by the vertices, but the mesh motion calculations were performed at the control points. These control points coincided with the cell centers. The model first calculates the locations of control points, then determines the locations of the vertices by interpolation, and then moves the vertices. In the model, the computational grids between the water-sediment interface and water-air interface are stretched to keep the fractions of local flow depth unchanged.

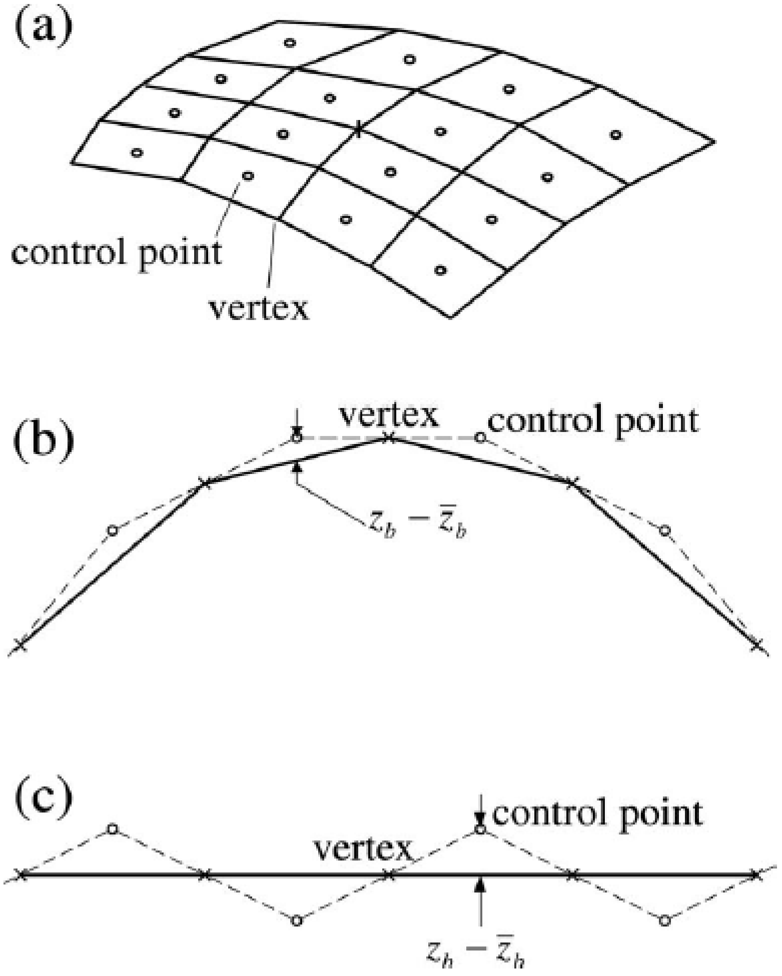

Figure 2.4 Control points and cell vertices: (a) arrangement; (b) constant curvature (in two dimensions); and (c) "sawtooth" pattern (Apsley and Stansby 2008)

Liu and García (2008) implemented a three-dimensional numerical model with the automatic mesh deformation technique for mesh motions, which can solve the Laplacian equation for grid motion using the finite-volume method. They have successfully simulated a wall jet scour case and a case of wave scour near a vertical cylinder. This typical automatic mesh deformation technique cannot accommodate large deformation, limiting its widespread usage. As can be seen in Figure 2.5, Liu and García (2008) avoided the mesh failure problem by adding an artificial geometric discontinuity into the domain. Although their model produced results that matched very well with the experimental measurements, the model has two disadvantages. First, the application of the method is strictly limited. The artificial modification worked with the benchmark test that was utilized to validate the model but may not work with a case with a different magnitude of bed deformation. Apparently, modelers could not properly determine the required artificial geometric discontinuity unless they knew in advance the final bed profiles. Second, the effects of the artificial geometry on the results are non-negligible, so numerical predictions obtained by a model with artificial geometry modifications are somewhat unreliable.

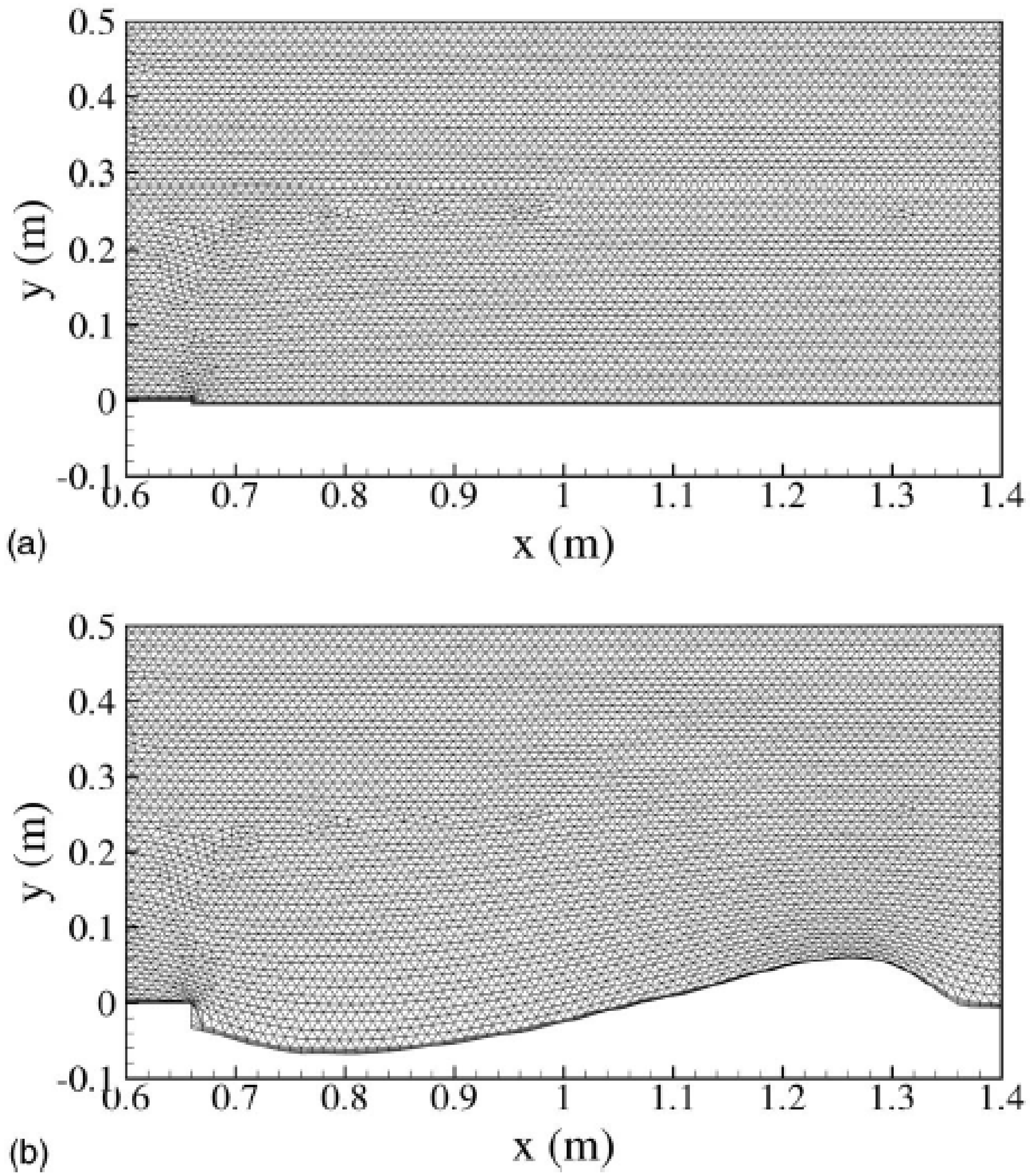

Figure 2.5 Turbulent wall jet scour mesh deformation: (a) initial; (b) equilibrium (Liu and García 2008)

Marsooli and Wu (2014) developed a 3D numerical model to simulate dam-break flows with sediment transport over erodible beds. The model uses the finite-volume method to solve the 3D Reynolds-Averaged Navier-Stokes equations. The simulations were conducted using collocated hexahedral meshes. The computational meshes were generated by two steps: first, a 2D mesh for the sediment bed was generated, and second, the 2D mesh was copied in the vertical direction to form a 3D mesh. As can be seen in Figure 2.6, the model uses unit normal vectors for the cell faces to determine the geometric properties of control volumes. The performance of the model has been validated using several experiments of dam-break flows on movable beds.

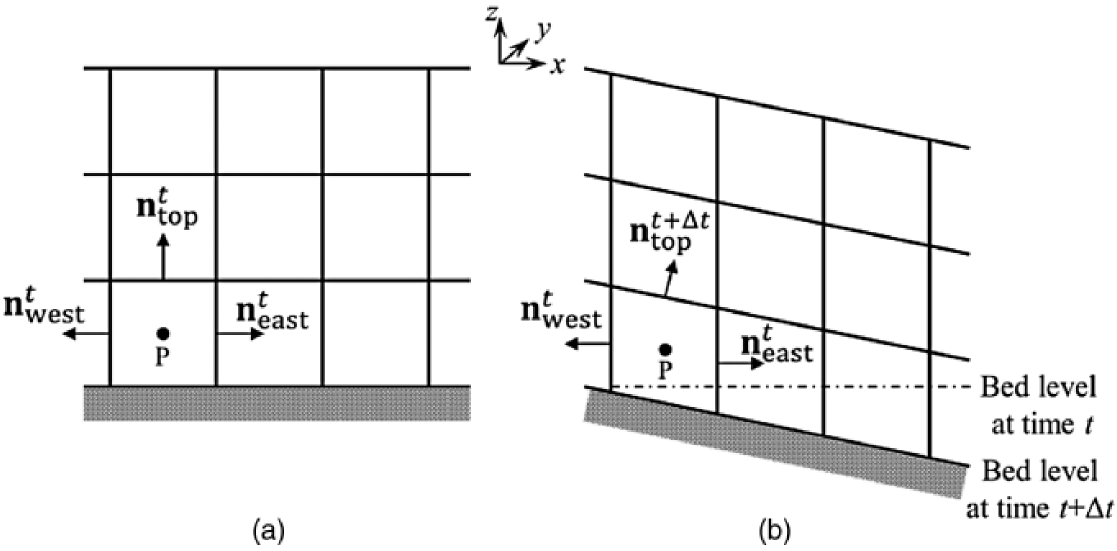

Figure 2.6 Side views of unit normal vector of cell faces: (a) time = t; (b) time = t+Δt (Marsooli and Wu 2014)

Zhao et al. (2010) have developed a 3D numerical model to simulate local scour around a submerged vertical circular cylinder in steady currents. The model is based on the finite element method. It uses the Arbitrary Lagrangian Eulerian (ALE) scheme to solve the governing equations with the moving boundary considered. A typical computational mesh near the cylinder is shown in Figure 2.7. The positions of the mesh nodes move in each step of boundary motion. The comparisons between the experimental and numerical results showed that the model can well predict the main mechanisms of the erosion, such as the horseshow vortex and vortex shedding, but the model underestimated the scour depth by about 10 to 20%.

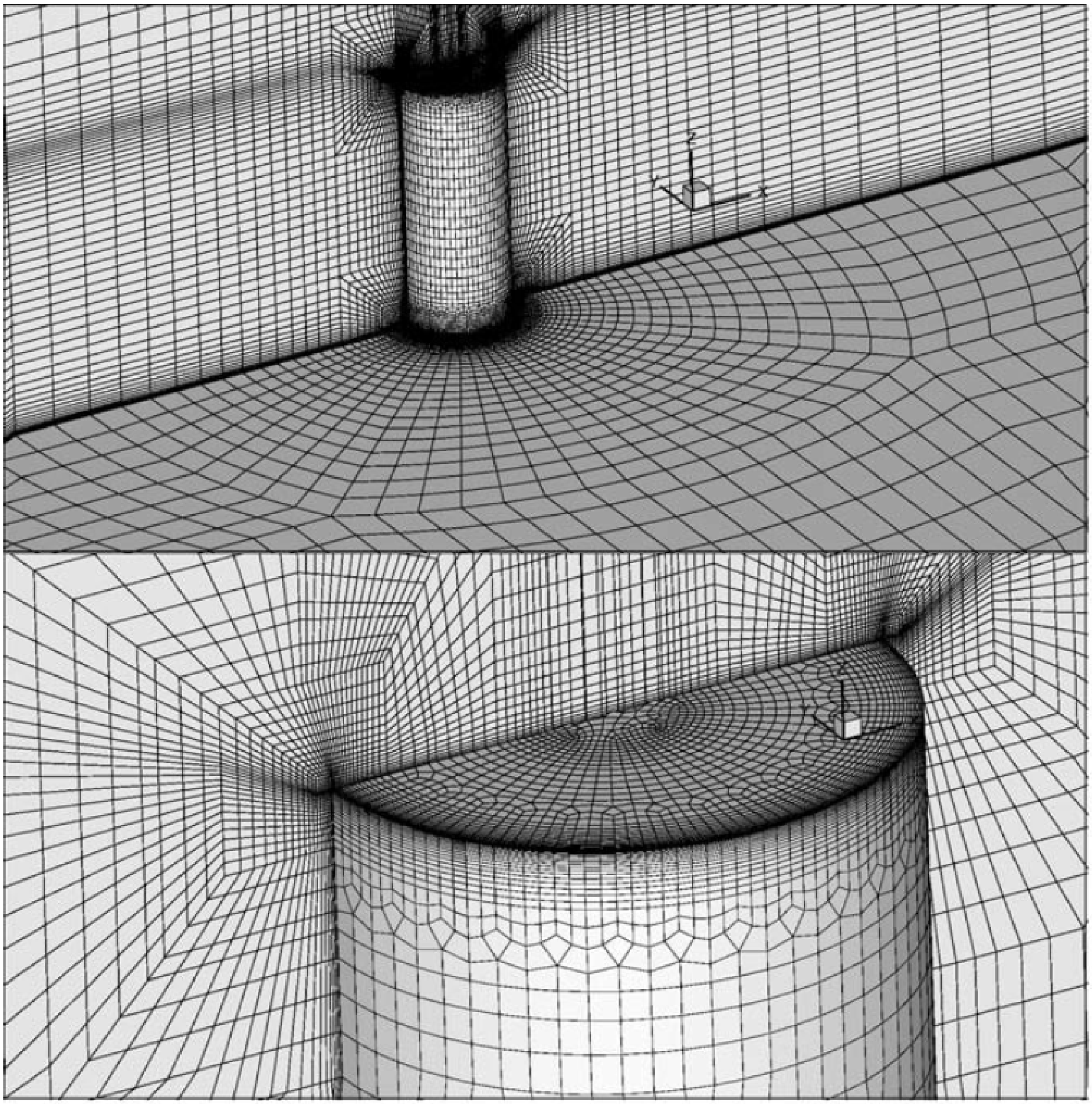

Figure 2.7 Computational meshes around the circular cylinder (Zhao et al. 2010)

2.4 Sediment scour models based on fixed-grid methods

In a fixed-grid (interface-capturing) method, the computations are carried out on a non–moving mesh, where an interface or fraction function is solved to “capture” or implicitly describe the interface.

Zhao and Fernando (2007) used an Euler-Euler coupled two-phase model within the package FLUENT to simulate scour around pipelines. The model considers two phases: fluid and sediment particles and it considers both flow-particle and particle-particle interactions. The model solves the governing equations for the water and sediment phases, and can determine the fluid-sediment interface based on the volume fraction. The mesh for the two-phase model calculations is shown in Figure 2.8. The mesh had two zones: water zone and sediment zone. To increase the model accuracy, Zhao and Fernando (2007) used an independent single-phase model instead of the two-phase model to simulate the flow field. They determined the water-sediment interface at an intermediate time instant according to the sediment volume fractions simulated by the two-phase model, then regenerated the grid for the single-phase model and performed the hydrodynamic simulations, and finally used the results of hydrodynamic simulations as inputs of the two-phase model to simulate the movements of sediment particles in a subsequent time step. The model provided satisfactory prediction of the bed profiles corresponding to the experiment by Mao (1986).

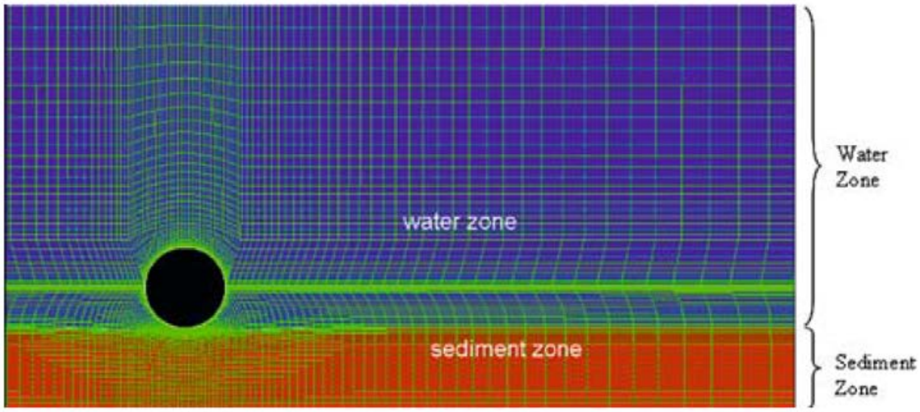

Figure 2.8 The grid for the two-phase model calculations (Zhao and Fernando 2007)

Amoudry and Liu (2009) developed a 2D two-phase model for non-cohesive sediment transport. The model considers two phases: fluid and sediment phases. It uses drag forces to simulate the interphase momentum transfer and a collisional theory to calculate sediment stresses. The model has been applied to simulate scouring downstream of an apron, and the comparisons between the experimental measurements and numerical predictions demonstrated that the model is a promising tool. However, the authors have acknowledged two major weaknesses of the model: first, the proposed method is much more expensive than the traditional method that considers dilute flow and solves the sediment continuity equation to locate the water-sediment interface. Second, the model only considers collisional particle interactions while non-collisional particle interactions may also be important.

Khosronejad et al. (2011) proposed a model for sediment transport phenomena based on the curvilinear immersed boundary method. The schematic of the method is illustrated in Figure 2.9. The simulations used a structured curvilinear mesh as a background mesh and an unstructured triangular mesh to track the immersed boundary (the water-sediment interface). The unstructured triangular mesh was Lagrangian, and the model used the sediment continuity equation and the hydrodynamic variables to locate the evolution of the fluid-sediment interface. The information on the location of the fluid-sediment interface was then transferred back to the hydrodynamic module, which used the structured curvilinear mesh to calculate the hydrodynamic variables. A major advantage of the model is that it does not require mesh updates for the hydrodynamic computations. The model has been validated against experiments on bed-load sediment transport in 90° and 135° channel bends, and the model satisfactorily predicted the main flow and scouring features.

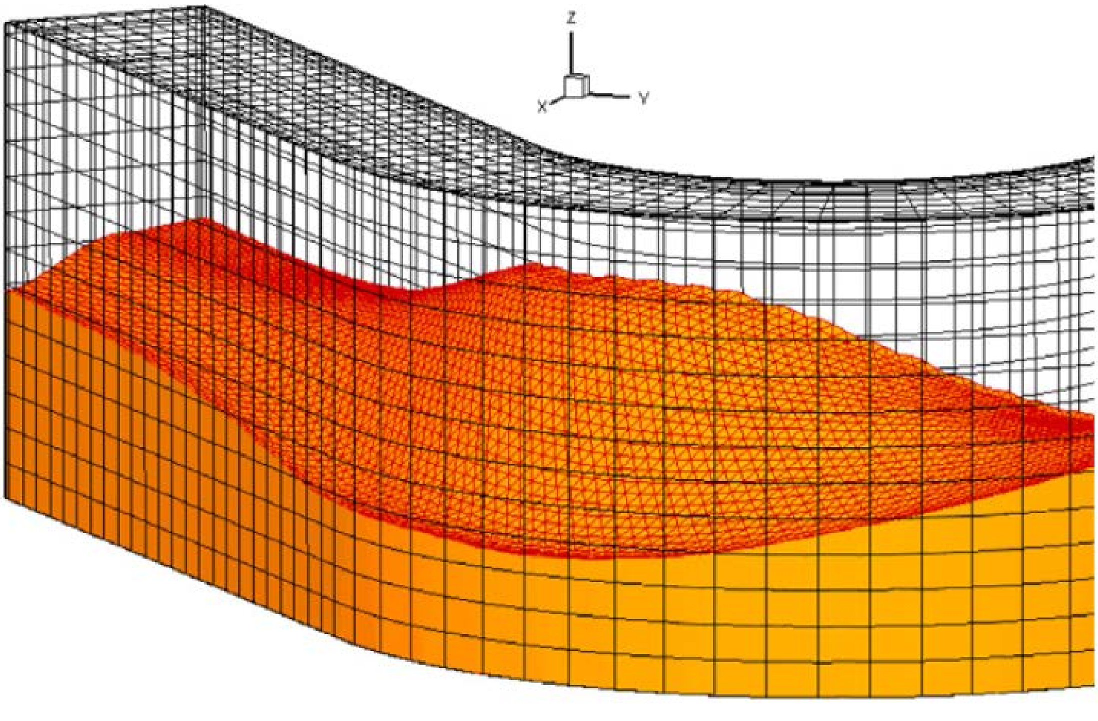

Figure 2.9 Schematic of the proposed approach (Khosronejad et al. 2011)

Lee et al. (2016) a developed a multi–dimensional, rheology–based, two–phase model for sediment transport and applied the model to problems concerning sheet flow and scour under a pipeline. Similar to the mode presented by Amoudry and Liu (2009), it also considers the fluid and sediment particles as two phases. A volume fraction of 0.5 was used to identify the fluid-sediment interface. The mesh in the vicinity of the pipeline in the simulation is shown in Figure 2.10. The model uses volume fraction to capture the fluid-sediment interface, so it does not need to update the grids. The model can rigorously model the fluid-sediment interaction and inter-sediment interaction. The model also incorporates rheological characteristics. The model was validated against two benchmark tests: sheet flow and scour under a pipeline, and the results were satisfactory. The authors have acknowledged two important shortcomings: first, there was a fitting parameter for the influence of sediment on turbulence, but it had not been well studied; second, the model overestimated the deposition behind the pipeline, probably because the k-ε model was used for turbulence modeling, and thus the vortex shedding cannot be well predicted.

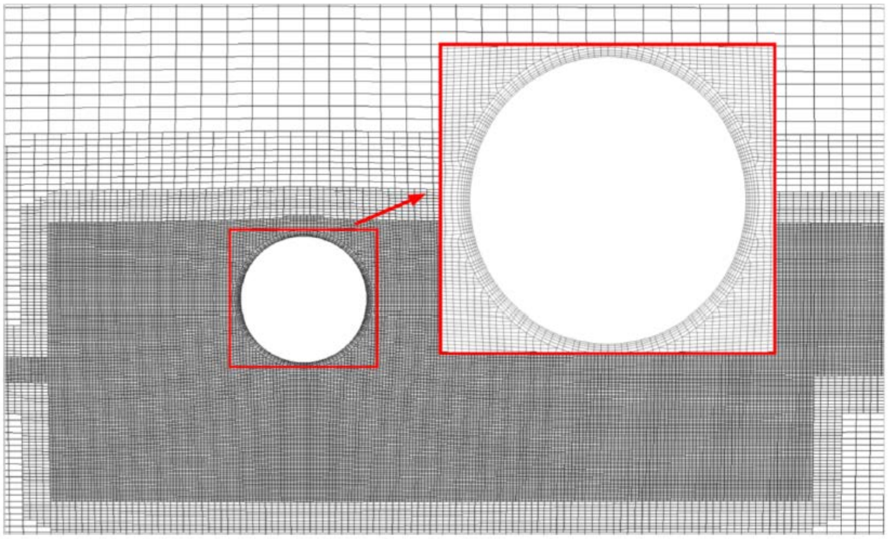

Figure 2.10 Mesh in the vicinity of the pipeline (Lee et al. 2016)

Lee et al. (2017) extended the model presented by Lee et al. (2016) by incorporating a third phase. Thus, the proposed model was a rheology-based three-phase flow model. Therefore, the newly proposed model can capture both the flow-sediment and flow-air interfaces. The model also uses a modified k-ε model, which can simulate the turbulence modulation because of water-sediment interaction. The model was applied to simulating a case with sediment transport under 1D open-channel flow condition and a case with local erosion due to wall jets from a sluice gate. The mesh for the wall jet scour case is shown in Figure 2.11. The model regarded sediment particles as a special phase and can directly calculate the concentration of the sediment particles, so the mesh can be kept unchanged during the simulations. It was found that the model can accurately reproduce the scour hole but it slightly underestimated the downstream dune. The model has also been found capable of simulating sediment avalanche events.

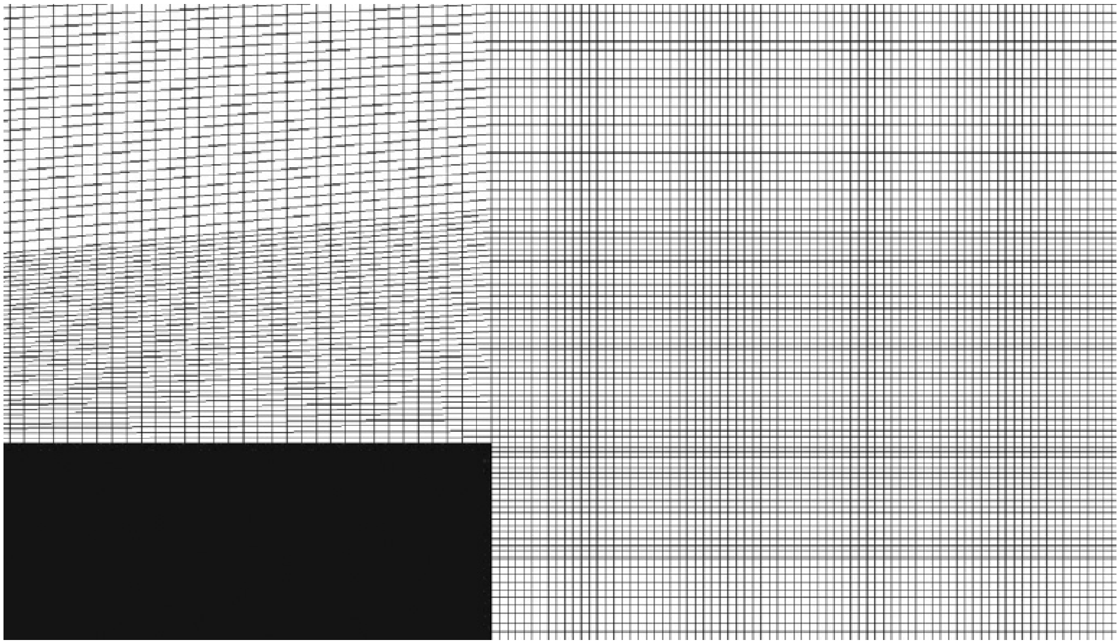

Figure 2.11 The mesh configuration (Lee et al. 2017)

Cheng et al. (2017) presented a multi-dimensional Eulerian two-phase model for sediment transport. Similar to the models presented by Amoudry and Liu (2009) and Lee et al. (2016), the model presented by Cheng et al. (2017) also considered two phases: fluid and sediment. A sample snapshot is shown in Figure 2.12. As can be seen, the model can simulate the concentration of the sediment particles, and it can present the sediment particles like fluids. The model incorporated closures of particle stresses and water-sediment interactions, so it can simulate both the interactions between the particles and the interactions between the particles and fluid. A key advantage of this approach is that the model does not need to use the bedload/suspended load assumptions. The model has been validated against a case with steady and oscillatory sheet flows and a case with scour downstream of an apron. As mentioned by Cheng et al. (2017), the closure coefficients for describing turbulence-sediment interactions can influence the predictions, and reasonably determining these coefficients may require further investigations.

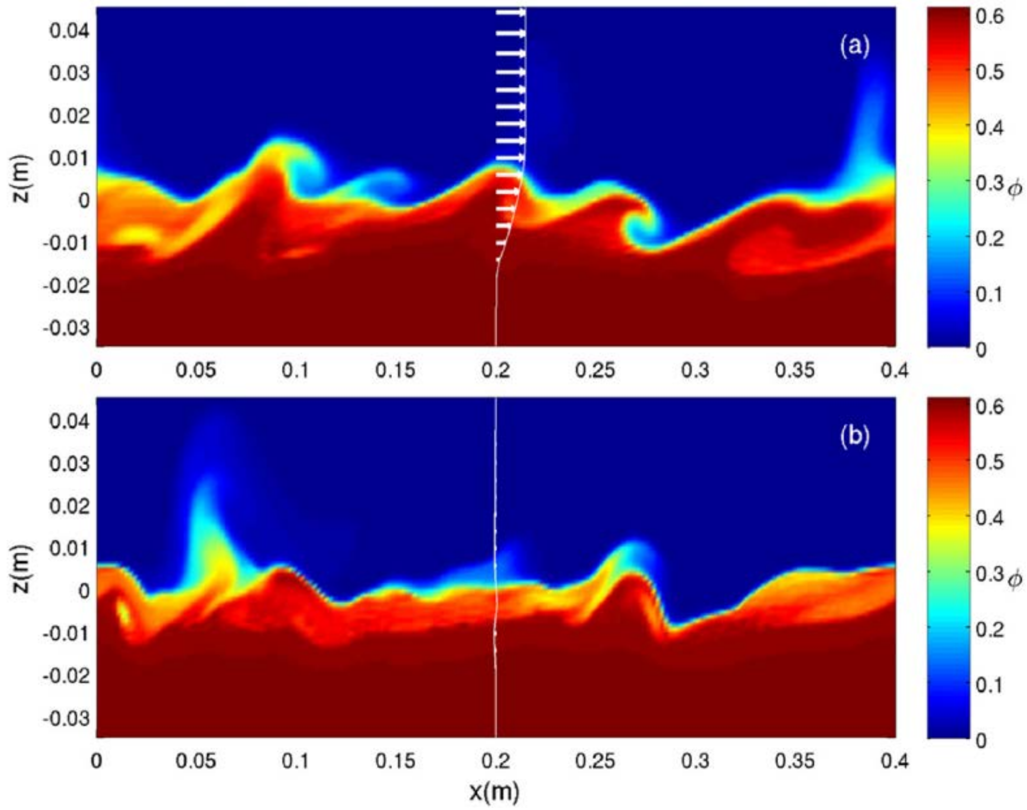

Figure 2.12 Snapshot of concentration field at (a) flow peak (t = 0.45 s) and (b) flow reversal (t = 0.9 s) for a sample case; white arrows denote the plan-averaged velocity vectors (Cheng et al. 2017)

2.5 Concluding remarks

The present literature review summarizes the governing equations, turbulence models, sediment scour equations, some previous models based on the moving-mesh approach, and previous models based on the fixed-grid approach.

The governing equations have been widely validated and thus do not require re-evaluations. There are some clear uncertainties regarding turbulence models. For example, different turbulence closures use different equations to calculate the eddy viscosity and the inverse effective Prandtl number. Therefore, a numerical model must be validated against experiments. In the present study, the implemented models are validated against both newly conducted experiments and benchmark experimental data published in the literature. A detailed comparison of different turbulence models is out of the focus of the present project because a sediment scour model also has some other uncertain parameters, such as the roughness height coefficient and sand-slide models, and the existence of these uncertain parameters may lead to misunderstandings about the performance of a turbulence model.

In terms of bedload modeling, the present literature review classifies the sediment scour models into four categories: formulas based on the shear stress approach, formulas based on the probabilistic approach, formulas based on the stream power approach, and formulas based on the discharge approach. A review of the literature reveals that no formula performed consistently well and no general accepted rule of formula selection has been drawn. The present project focuses on the shear stress approach because it is very straightforward in terms of its physical mechanisms. The other sediment transport models can be evaluated in future studies.

The present literature review classified the previous sediment scour models into two categories: moving-mesh and fixed-grid. Moving-mesh methods have some advantages regarding the mass conservation and discontinuities across the interface, are less sensitive to the size of computational grids around the interface, and can produce more accurate results at comparable levels of mesh resolution. However, as can be seen in the figures of computational meshes for the moving-mesh models, the complexity of the computational mesh significantly increases with increasing complexity of the geometry. Therefore, it can be speculated that the traditional moving-mesh approach cannot be used for problems with a complicated geometry. For a simple case, such as the wall jet scour one, modeling the phenomenon using a traditional moving-mesh approach is possible if slightly modifying the geometry is believed acceptable. However, for a relatively complicated case, extensively modifying the geometry to ensure a satisfactory mesh quality may cause unacceptable uncertainties.

The fixed-grid approach can eliminate the problem of mesh quality. However, it is typically less accurate than the moving-mesh approach in describing the water-sediment interface. The immersed boundary method is very promising, but it requires the user to accurately estimate the maximum scour depth prior to the simulations; if not, the computational domain will be too large or too small because the physical domain varies with time. Multi-phase models are also very promising especially because they can directly model the interactions between the sediment particles and interactions between water and sediment particles. However, the mechanisms for the interactions are very complicated and far from well understood, so accurately modeling them is difficult to happen in the near future. As mentioned in the review, the closure coefficients for describing turbulence-sediment interactions can influence the predictions, and reasonably determining these coefficients may require further investigations. Furthermore, modeling the complicated details regarding the interactions can be very computationally expensive and is thus difficult to use in practical applications in the near future.

Therefore, it is very beneficial to propose a new approach that can combine the best properties of the traditional moving-mesh and fixed-grid methods, which is a major purpose of the present study.

Chapter 3 Numerical modeling of local scour due to submerged wall jets using a strict vertex-based, terrain conformal, moving-mesh technique in OpenFOAM

Published in the International Journal of Sediment Research: 2020, 35(3), 237-248.
DOI: 10.1016/j.ijsrc.2019.12.007.

Yan, X., Mohammadian, A., and Rennie, C. D.

Abstract: This study presents the implementation and validation of a new sediment-scour model with a strict vertex-based, terrain conformal, moving-mesh technique within the framework of OpenFOAM. OpenFOAM lacks the ability to simulate large-amplitude motion needed for analysis of sediment-scour problems, and, thus, its application normally is restricted to small-amplitude cases to prevent computational divergence due to mesh deterioration. The proposed simple, moving-mesh technique in OpenFOAM is implemented to overcome the shortcomings of the conventional automatic mesh-motion techniques in handling large-amplitude moving geometries. The model is used to simulate a simple case of prescribed boundary motion, a previous experiment in the literature, and a new laboratory experiment for local scour due to submerged wall jets. The results are compared with both the experimental and other numerical results. The comparisons demonstrate that the proposed model has the novel advantage of allowing for more severe topographic variations, and can provide more reliable predictions for the key characteristics and evolution of the bed profiles in wall jet scour problems. Furthermore, to improve the practice of modeling wall jet scour, various turbulence modeling approaches and bedload equations also are evaluated and compared.

Keywords: Numerical modeling; Sediment scour; Submerged wall jets; Moving mesh; OpenFOAM; Bed evolution

3.1 Introduction

Flows often pass hydraulic structures in the form of turbulent jets; examples include jets discharged at underflow gates, outlet works, and reservoir spillways (Habibzadeh and Rajaratnam, 2016; Khosronejad and Rennie, 2010; Melville and Lim, 2013). Turbulent jets can occur as submerged wall jets, such as the jets issuing from sluice gates. These types of jets usually cause severe local erosion of streambed material, which can jeopardize the safety of the hydraulic structures (Dey and Sarkar, 2006; Rajaratnam and Macdougall, 1983; Rajaratnam, 1981; Sarathi et al., 2008; Wu et al., 2018). Therefore, it is desirable to better understand the processes and characteristics of local scour caused by submerged wall jets to ensure streambed stability and the safety of the nearby hydraulic structures, and, thus, it is of primary importance for researchers to propose better research methodologies or numerical models.

Sediment-scour and deposition phenomena can be efficiently simulated using computational fluid dynamics (CFD) models (Franz et al., 2017; Jian et al., 2015; Khosronejad et al., 2007; Langendoen et al., 2016; Mendoza et al., 2016). Depending on the methodology used to identify the dynamic location of fluid-sediment interfaces, these models can be categorized into interface–capturing (fixed-grid) and interface–tracking (moving-grid) models (Charin et al., 2017). In an interface–capturing method (e.g., Amoudry and Liu, 2009; Cheng et al., 2017; Lee et al., 2016, 2017), the computations are done on a non–moving mesh, where an interface or fraction function is solved to “capture” or implicitly describe the interface. In an interface–tracking method (e.g., Fang and Rodi, 2003; Fang and Wang, 2000; Apsley and Stansby, 2008; Liu and García, 2008; Marsooli and Wu, 2014; Zhao et al., 2010), the computational grids are moved or deformed with the flow field to “track” or explicitly describe the surface.

The interface-tracking method has more advantages than interface-capturing methods regarding the mass conservation and discontinuities across the interface, is less sensitive to the size of computational grids around the interface, and can produce more accurate results at comparable levels of mesh resolution (Mirjalili et al., 2017; Tezduyar, 2006; Watts et al., 2005). It has also been successfully utilized in actual cases. For example, a three-dimensional (3D) numerical model based on the interface-tracking method has been developed and utilized to simulate the flow and sediment transport for the Three Gorges Project (Fang and Rodi, 2003; Fang and Wang, 2000), and the numerical predictions closely matched the measurements. Therefore, this study focuses on the interface-tracking method. A deficiency of the interface-tracking method is that the mesh quality often severely deteriorates due to grid updates. This is a very common and serious problem that has been troubling the community of sediment-scour analysts for many years and has significantly hindered the wider use of the interface-tracking approach, and, thus, this problem requires further investigation.

New numerical techniques or models can be implemented within the framework of OpenFOAM. It is attractive for sediment-scour applications because of its high-quality hydrodynamic solvers and turbulence models, and its advantages of being open source and readily modifiable and extendable. However, the existing automatic mesh-deforming techniques in OpenFOAM lack the ability to do the large-amplitude motions needed for sediment-scour problems because of the reasons mentioned earlier, and, thus, its application is normally restricted to small-amplitude cases to prevent divergence due to mesh deterioration (Shen et al., 2015). To the authors' knowledge, the only published study that successfully simulated the wall jet scour phenomenon using an interface-tracking approach in OpenFOAM is Liu and García (2008). Liu and García (2008) implemented a sediment-scour model that uses a standard automatic mesh-motion technique available in OpenFOAM, and modified the model geometry by adding an artificial geometric discontinuity into the domain to prevent divergence caused by excess mesh deformation. Although reasonable results were obtained for the specific tested cases, artificially manipulating case geometries usually causes unacceptable uncertainties. Therefore, it is better to implement a model that can directly simulatelarge-amplitude motions in a more practical and reliable way. Recently, Shen et al. (2015) implemented the dynamic overset grid technique into OpenFOAM and applied the model to KRISO Container Ship (KSC) self-propulsion and maneuvering. This technique permits separate grids to overlap and interpolates the information between the grids. It uses the code Suggar to calculate the domain connectivity information dynamically at run time. It has opened the possibility of simulating cases with arbitrarily large boundary deformation in OpenFOAM, but the complex theory and dynamic data exchange between Suggar and OpenFOAM make the models too complicated and computationally expensive for practical sediment-scour applications. Therefore, a relatively simpler moving-mesh technique is desired.

The primary objective of the current study is to implement and validate a new sediment-scour model in OpenFOAM that uses a strict vertex-based terrain conformal moving-mesh technique. A total of six additional models using the conventional moving-mesh techniques available in OpenFOAM have also been implemented. The results for a simple case of prescribed boundary motion show that the proposed model has the novel advantage of allowing for more severe topographic variations. To evaluate the accuracy of model predictions, the experiment by Chatterjee et al. (1994) was simulated using the proposed model. The comparisons with the experimental and previous numerical results demonstrate that the proposed model can provide promising predictions for sediment-scour problems compared with current modeling practice. To gain more confidence in the implementation and provide more insight, a new laboratory experiment was done and simulated using the proposed model. The good agreement between the experimental and numerical results confirmed that the model can be used as a reliable tool to simulate local scour problems due to submerged wall jets. Furthermore, various turbulence modeling approaches and bedload equations also are evaluated to improve the practice of modeling wall jet scour.

3.2 Methodology

3.2.1 Hydrodynamic model

The governing equations are the three–dimensional Reynolds–Averaged Navier–Stokes equations (RANS) for incompressible flows as follows:

$$\nabla \cdot \mathbf{U} = 0 \tag{3.1}$$

$$\frac{\partial \rho \mathbf{U}}{\partial t} + \nabla \cdot \left(\rho \mathbf{U} \mathbf{U} \right) = \nabla \cdot \mathbf{T} + \rho \mathbf{g} - \nabla p \tag{3.2}$$

where $\mathbf{U}$ is the flow velocity vector; ρ is the density; t is the time; $\mathbf{T}$ is the viscous stresses tensor; $\mathbf{g}$ is the gravitational acceleration vector; and p is the pressure.

A Volume of Fluid (VOF) phase–fraction–based Eulerian interface–capturing approach (Hirt and Nichols, 1981; Rusche, 2002) is used to capture the water–air interface. There are many turbulence models available in OpenFOAM. Among them, the standard k–ε model (Jones and Launder, 1972) is one of the most widely used, and can provide a good balance between accuracy and efficiency for simulations of turbulent jets (Yan and Mohammadian, 2017).The model can be expressed as:

$$\frac{\partial k}{\partial t} + \nabla \cdot \left(\mathbf{U}k\right) - \nabla\left[(\frac{\nu_t}{\sigma_k} + \nu)\nabla k \right] = G - \varepsilon \tag{3.3}$$

$$\frac{\partial \varepsilon}{\partial t} + \nabla \cdot \left(\mathbf{U}\varepsilon\right) - \nabla\left[(\frac{\nu_t}{\sigma_\varepsilon} + \nu)\nabla \varepsilon \right] = c_{1\varepsilon} G \frac{\varepsilon}{k} - c_{2\varepsilon} \frac{\varepsilon^2}{k} \tag{3.4}$$

$$\nu_t = c_\mu \frac{k^2}{\varepsilon} \tag{3.5}$$

where k is the turbulent kinetic energy; ε is the turbulent energy dissipation rate; ν_t is the turbulent kinematic viscosity; ν is the kinematic viscosity; G is the production of turbulence due to shear; σ_k, σ_ε, $c_{1\varepsilon}$, $c_{2\varepsilon}$, c_μ are model constants equal to 1.0, 1.3, 1.44, 1.92, and 0.09, respectively. The other turbulence models are not explicitly described here, for the sake of brevity.

3.2.2 Bed morphology model

The temporal changes in the bed elevation are governed by the sediment continuity equation, which can be expressed as (Khosronejad et al., 2011; Liu and García, 2008;

Paola and Voller, 2005)

$$(1-\gamma)\frac{\partial z_b}{\partial t} = -\nabla \cdot \mathbf{q}_B + D - E \tag{3.6}$$

where γ is the bed material porosity; z_b is the bed elevation; $\mathbf{q}_B$ is the bed–load flux vector, D is the deposition rate and E is the entrainment rate. For the cases considered in the present study, the dominant mode of transport is bedload; thus, D and E were not modeled because the modeling of these variables is computationally expensive, with minimal value added for cases with minimal suspended sediment transport. Four widely accepted and relatively simple bedload equations have been implemented: Meyer-Peter and Müller formula (1948), Engelund and Fredsøe (1976), Nielsen (1992), and Camenen and Larson formula (2006). The Shields number, θ_i, and the critical Shields number for sediment entrainment, θ_c, can be determined from the Soulsby-Whitehouse equation (Soulsby and Whitehouse, 1997). A standard rough wall function in OpenFOAM is used to calculate the turbulent viscosity. The sand–grain roughness height, k_s, can usually be estimated based on the sediment diameter d_χ (χ represents the percentage of sediment that is finer). It can be defined as

$$k_s = \delta d_{50} \tag{3.7}$$

where d_{50} is the median grain size (Wren et al., 2018), δ is an empirical coefficient (typically ranging from 1 to 6.8) that mainly accounts for the effect of form roughness. In the present study, various simulations with different values of δ (from 1 to 6.8) have been performed, and the best performing value of δ was determined by comparing the simulated results to the experimental data at the first minute and validating the model and configurations using the remaining data.

In addition to the equations mentioned above, a sand-slide algorithm, based on the equations used by Khosronejad et al. (2011), the Koch and Flokstra (1981) equation for the effects of bed slope, and a vertex-based moving mesh scheme were also implemented in the model.

3.2.3 Implementation of the mesh-motion module

The current study develops a new vertex–based, terrain conformal, moving–mesh module within the OpenFOAM framework. In order to calculate mesh motions at nodal vertices, flow variables are interpolated to mesh nodes and then sediment transport is calculated at the mesh nodes. This ensures that mesh adjustments correctly reflect bathymetric changes while avoiding mesh intersections, even in relatively steep and complex topography.

The model moves the internal grids based on the following equation (assuming that the initial vertical coordinate of the bottom patch point is zero):

$$y_{new} = Y_{top} - \frac{Y_{top} - y_{initial}}{Y_{top}} \times \left(Y_{top} - y_{bottom} \right) \tag{3.8}$$

where y_{new} is the new vertical coordinate of an internal node; Y_{top} is the vertical coordinate of the top boundary in the water column; $y_{initial}$ is the initial vertical coordinate of the node; and y_{bottom} is the vertical coordinate of the bottom boundary in the water column.

A time-marching scheme, similar to that utilized by Liang et al. (2005), has been developed, that assigns different time steps to the flow and bed morphology calculations; for example, a larger time step for a bed morphology module can be used to save computational time. To increase the accuracy and reduce the uncertainty of the numerical predictions, however, the time steps for the two modules in the current study were set to be equal. The moving-mesh module is activated when the hydrodynamic solver performs the first iteration of the PIMPLE pressure-velocity loop, which is an option in the OpenFOAM platform. The detailed procedures are illustrated in Figure 3.1.

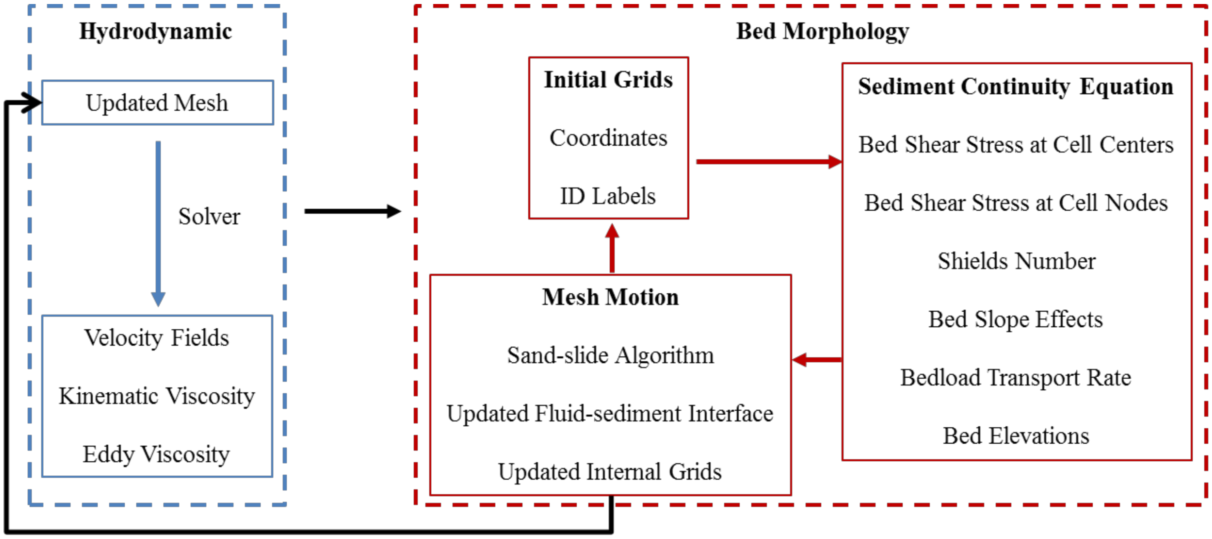

Figure 3.1 Flow chart of the modeling procedures

3.2.4 Model setup

A schematic diagram of the problem of interest is shown in Figure 3.2: a vertical sluice gate, L_g thick, is placed above an apron, and the gate opening from the top surface of the apron is h_0. An overflow weir, h_w in height and L_w in thickness, is positioned at the downstream end of the flume, which controls the tail water level, h_d. The upstream and downstream ends of the apron are located L_r and L_a from the sluice gate, respectively. A submerged wall jet is formed under the sluice gate due to the difference between the upstream water depth, h_u, and downstream water depth, h_d. The jet moves and diffuses along the apron, and then erodes the sediment bed as the local shear stresses caused by the flow exceed the critical shear stress. The sediment bed is originally L_s long and h_b deep, but a scour hole and dune are formed because of the process of sediment erosion and deposition.

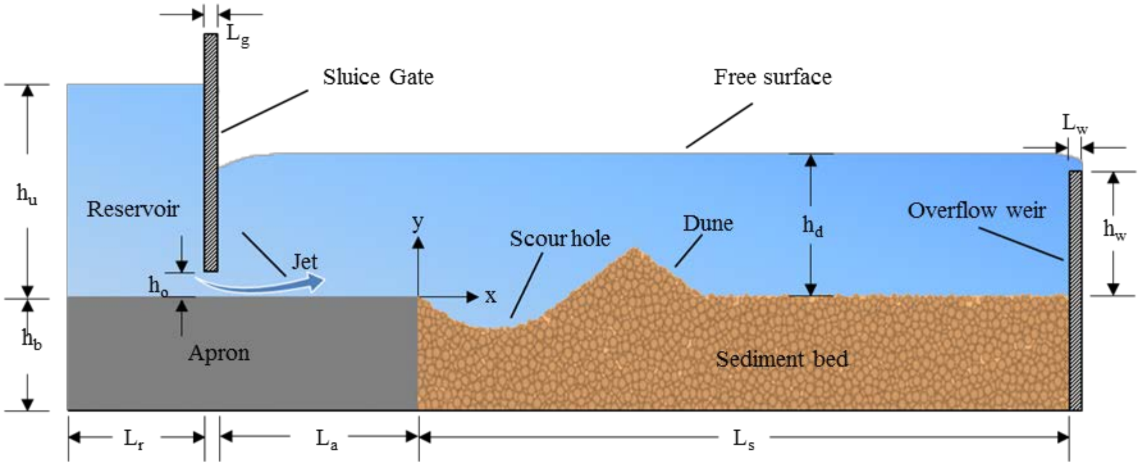

Figure 3.2 Schematic diagram of a submerged wall jet

A uniform stream–wise velocity, which was calculated by the flow discharge and the area of the inlet patch, was specified at the inlet. A rigid lid, rather than a free surface condition, was specified at the top patch upstream of the sluice gate, as the free surface in the upstream region is not of interest. The "inletOutlet" boundary condition in OpenFOAM was assigned to the atmosphere (i.e. the top patch of the computational domain) as explained in the following (Yan and Mohammadian, 2017). For this boundary condition function, when there is no backward flow, the boundary condition becomes the zero–gradient open boundary condition. When there is backward flow, the boundary condition automatically becomes a fixed–value boundary condition. A zero–gradient open boundary condition was used for the outlet. The sluice gate, apron, and overflow weir are regarded as smooth walls, and the sediment bed as a rough wall. The boundary conditions at the front and back patches were set to "empty" so the simulation was reduced to a two-dimensional (2D) case.

Table 3.1 Parameters of the simulated cases

Simulation	Case	Moving Mesh	Turbulence	Bedload equations
S01C1P1	Prescribed boundary motion	Uniform	RANS	—
S02C1P2	Prescribed boundary motion	Inverse-distance	RANS	—
S03C1P3	Prescribed boundary motion	Quadratic-inverse-distance	RANS	—
S04C1P4	Prescribed boundary motion	Inverse-face-distance	RANS	—
S05C1P5	Prescribed boundary motion	Inverse-volume	RANS	—
S06C1P6	Prescribed boundary motion	Directional	RANS	—
S07C1P7	Prescribed boundary motion	Present scheme	RANS	—
S08C2C1	Chatterjee et al. (1994)	Present scheme	RANS	Meyer-Peter and Müller
S09C2C2	Chatterjee et al. (1994)	Present scheme	RANS	Engelund and Fredsøe
S10C2C3	Chatterjee et al. (1994)	Present scheme	RANS	Nielsen
S11C2C4	Chatterjee et al. (1994)	Present scheme	RANS	Camenen and Larson
S12C2C5	Chatterjee et al. (1994)	Present scheme	LES	Engelund and Fredsøe
S13C2C6	Chatterjee et al. (1994)	Present scheme	DDES	Engelund and Fredsøe
S14C2C7	Chatterjee et al. (1994)	Present scheme	IDDES	Engelund and Fredsøe
S15C3T1	The present experiment	Present scheme	RANS	Engelund and Fredsøe

Structured meshes with local refinements were used in the current study, and the mesh resolution was determined following the mesh sensitivity analysis procedures used by Yan and Mohammadian (2017) with a confidence criterion of ± 0.001 m. A disadvantage of the interface-tracking approach is that the sizes of the computational grids vary with the moving interface, which can cause the size of the first grid near the wall to be too big when the calculation time is approaching completion. To avoid this problem, the standard rough wall function in OpenFOAM was utilized, which eliminated the need to resolve the boundary layer, and mesh sensitivity analyses were done to ensure that the first cell size was sufficiently small at the end of the scour process. A value of 1 was assigned as the maximum Courant number. In the current study, the time step was set to be 0.001 s for both the hydrodynamic and bed morphology simulations in all simulations (fully coupled). Additional simulations were done with smaller values for the time step, and the results were found to be almost identical to the final results with the 0.001 s time step.

The parameters for the important simulations are listed in Table 3.1. In the nomenclature used for the numerical simulations, the number after "S" denotes the simulation number. The second number (after the first "C") denotes the case number. The last number (after the key letter of the case name) denotes the simulation number for a case.

3.2.5 Experimental setup

The present experimental methodology was very similar to that of Chatterjee et al. (1994), but used different experimental parameters. Part of a straight rectangular channel, 12 m long, 0.38 m wide, and 0.6 m deep, with glass side walls and a steel bottom, was used. The inlet discharge per unit width was 0.0143 m^2/s, measured by an electronic flowmeter, and automatically adjusted by a valve on the inlet pipe. In the experiment, h_0 was 0.02 m, h_b was 0.15 m, L_a was 0.66 m, and L_s was 2.4 m. The sediment bed consisted of quartz sand, the median grain diameter of which was 0.689×10^{-3} m; and the critical Shields parameter was 0.0299. An overflow weir, 0.275 m in height (0.125 m higher than the sediment bed), was placed at the downstream end of the experimental area, which maintained the tail water depth at 0.15 m. At the beginning of the experiment, a very small flowrate was supplied, so the water slowly entered the flume without causing sediment scouring. When the downstream water level reached the top surface of the overflow weir, the discharge rate was suddenly increased to the target rate. The local bed profiles for different time sequences were captured using a digital single–lens reflex camera. A free and open–source image editor, the GNU Image Manipulation Program (GIMP), was used to correct image perspective distortion, according to several measured reference points. The experimental data were obtained by digitizing the sediment and water surfaces in the images. Velocity measurements were taken using a Nortek Acoustic Doppler Velocimeter (ADV), which is the profiling version of the Vectrino system, for the purpose of validating the initial wall jet. Each of the measurements was taken at the equilibrium stage for two minutes at a sampling rate of 25 Hz, and the results were averaged to obtain the mean flow velocity. Further details about the ADV measurements, such as the measurement accuracy and post-processing procedures, can be found in previous studies (Jamieson et al., 2013; Kashyap et al., 2012).

3.3 Results and discussion

3.3.1 Case A: a prescribed boundary motion case

To test the moving mesh strategies, a simple 2D case of prescribed boundary motion was designed. The length, height, and width of the computational domain were 0.2 m, 0.06 m, and 0.005 m, respectively. The bottom patch was designed to mimic an apron (fixed boundary) and sediment bed (moving boundary). The first 0.05 m of the patch was fixed, while the remaining 0.15 m moved in the vertical direction based on the following equation:

$$U_{\text{Prescribed}} = -\sin\left(31.4x - 1.57\right) \tag{3.9}$$

where $U_{prescribed}$ is the prescribed boundary motion velocity and x is the stream–wise coordinate. The time step, Δt, was set to be 0.001 s. The original vertical coordinates of the grid points on the moving boundary were zero. In each computational step, the model calculated the new coordinates of the moving boundary points using the sediment continuity equation.

In addition to the newly implemented model, six additional models, which applied various automatic mesh-motion techniques available in OpenFOAM, also were developed and evaluated, including the uniform, inverse-distance, quadratic-inverse-distance, inverse-face-distance, inverse-volume, and directional models. In these models, a Laplacian equation acts as the mesh motion equation, which can be expressed as

$$\nabla \cdot \left(\gamma_d \nabla \vec{u}\right) = 0 \tag{3.10}$$

where $\vec{u}$ is the grid motion velocity field and γ_d is the diffusion field.

The tested models required different equations to solve the diffusion field; for example, the uniform model assumes that the diffusion field is a constant, and the inverse-distance model calculates the diffusion field as the inverse of the distance of a computational cell center to the nearest selected interface. Further details about these models can be found in the source codes of OpenFOAM (OpenCFD Limited, 2014) and the relevant literature (Jasak, 2009; Jasak and Tukovic, 2006). All of the results showed a similar mesh failure mode, namely, an internal level intersected the boundary patch. These models perform differently when accommodating large-amplitude mesh motions, thus, the mesh failure occurred at different time steps with the different models. The uniform and quadratic-inverse-distance models failed at the seventh time step. The inverse-distance model was slightly better, which stopped at the eighth time step. The other models can last for nine time steps.

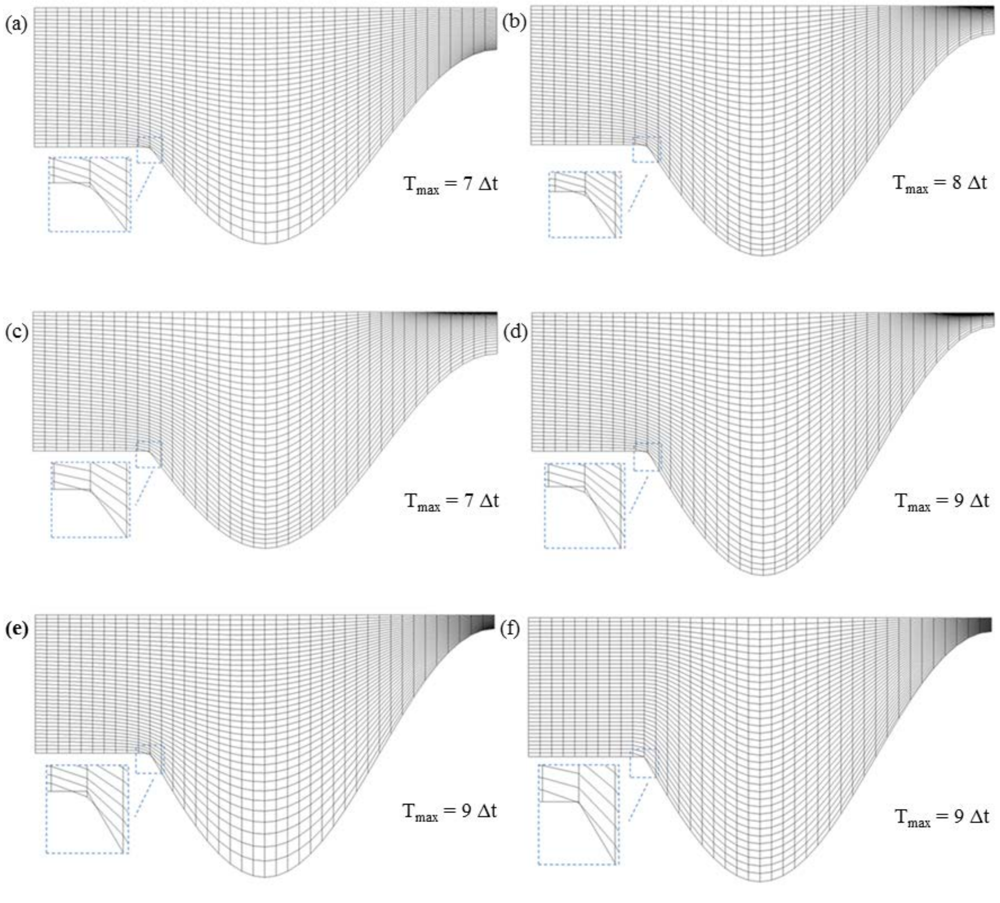

Figure 3.3 Meshes deformed using various moving-mesh models: (a) the uniform model; (b) the inverse-distance model; (c) the quadratic-inverse-distance model; (d) the inverse-face-distance model; (e) the inverse-volume model; (f) the directional

model. For each model, the subplot shows the mesh intersection failure

The deformed meshes at the last time step before mesh failure are shown in Figure 3.3. As can be seen in the figure, none of the evaluated models can effectively accommodate large deformation, including the uniform model, which was used by Liu and García (2008). This case demonstrates that the applications of the currently available moving-mesh schemes are strictly limited.

One possible solution is to adjust some of the parameters in the moving-mesh models, such as the exponent in a distance–based model, but this is not practical because the trial–and–error process may be quite time consuming, particularly when the magnitude of the interface deformation is unknown. Another possible solution is to modify the Laplacian equation. The authors added one more diffusion term into the Laplacian equation, but it can only improve the performance to a certain degree. Finally, the current vertex–based, terrain conformal, moving–mesh module within the OpenFOAM framework was developed herein (see Section 3.A for detailed description). The meshes deformed using the current moving–mesh model at different time sequences are shown in Figure 3.4. As seen in the figures, the problem of mesh intersection was completely avoided.

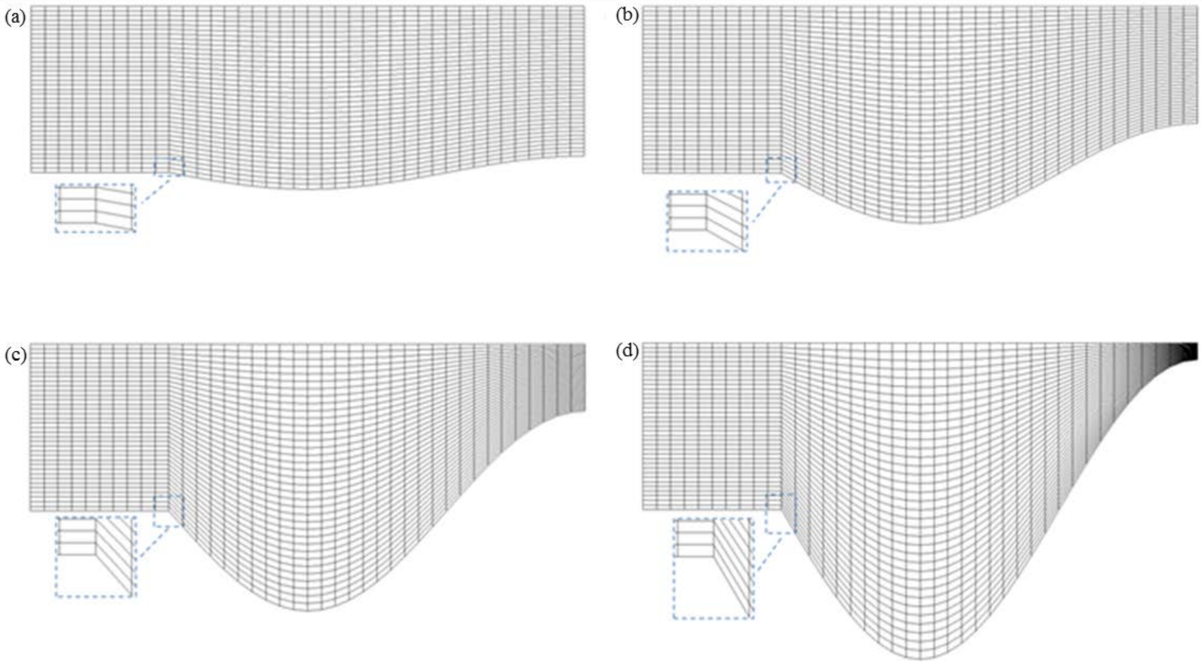

Figure 3.4 Meshes deformed using the present moving-mesh model at different time sequences: (a) t = 1Δt; (b) t = 3Δt; (c) t = 6Δt; (d) t = 9Δt

3.3.2 Case B: The experiment of Chatterjee et al. (1994)

The results of Run 2 in the experiments of Chatterjee et al. (1994) were used to evaluate the performance of the proposed model. The numerical setup was mainly determined based on the experimental conditions. The length, height, and width of the computational domain were 3.945 m, 0.414 m, and 0.005 m, respectively. As previously mentioned, a structured mesh with local refinements was used and the sizes of the computational grids varied with the moving interface. The number of computational cells was 73,976. The maximum size of the grid nearest the wall at the beginning and end of the simulation for Case B was 0.00125 m and 0.00142 m, respectively. The median sediment size was 0.76×10^{-3} m, the critical Shields parameter was 0.0300, the optimal value of δ was 3.5, the angle of repose was set to 29° (Liu and García, 2008), the unit inflow discharge rate was 0.0204 m^2/s, the gate opening was 0.02 m, the length of the apron downstream of the sluice gate was 0.66 m, and the length of the sediment bed was 3 m.

As for turbulence modeling, three more advanced techniques, large–eddy simulation (LES), delayed detached–eddy simulation (DDES), and improved delayed detached eddy simulation (IDDES), were tested in addition to the RANS simulation. The DDES computation was not numerically stable. The results at the first time instant (t = 60 s) obtained by the RANS (S09C2C2) turbulence modeling approaches are shown in Figure 3.5.

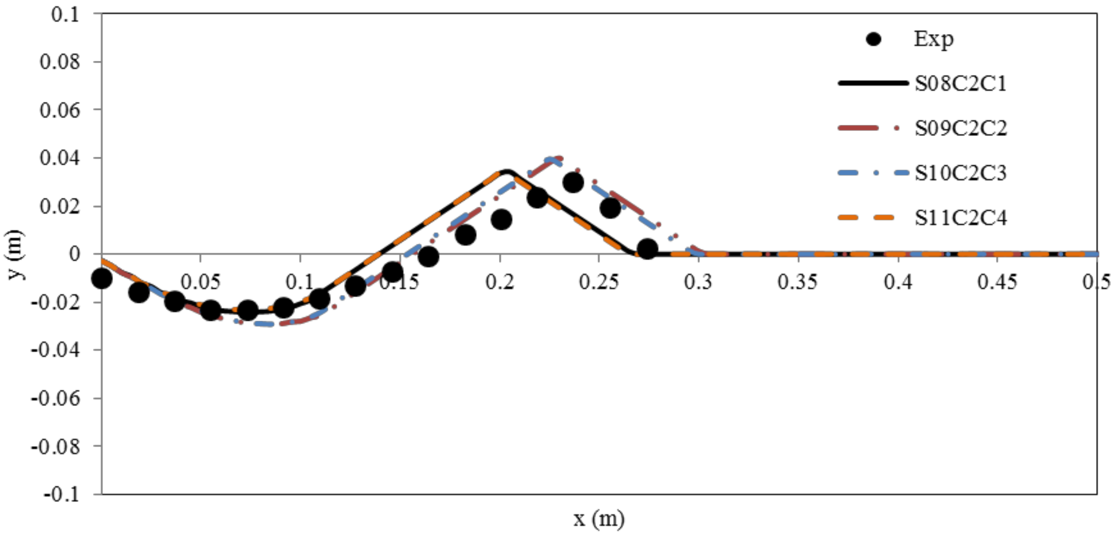

Figure 3.5 The bed profiles measured by the experiment and simulated by using various turbulence modeling approaches and bedload equations

Contrary to the commonly held view that advanced turbulence models will result in better simulations, the results obtained by these more advanced models were not reasonable (not shown). First, the magnitudes of local scour predicted by the LES and

IDDES models were much smaller than the measured values. Second, the LES and IDDES models predicted several scour holes and deposition dunes in the downstream region, which were not observed in the experiment. A possible reason is that the current simulations were 2D, and these advanced turbulence modeling techniques become less applicable for 2D cases. In the future, when more advanced computational techniques and powerful computing resources become available, 3D numerical modeling of local scour resulting from submerged wall jets using more advanced turbulence modeling approaches may be an interesting research topic. Moreover, the pattern of bed profiles implies that the LES and IDDES models predicted too many circulation cells or eddies in the flow, so a modified eddy filtering technique could be proposed for 2D simulations in future work.

The results simulated using the Meyer-Peter and Müller (S08C2C1), Engelund and Fredsøe (S09C2C2), Nielsen (S10C2C3), and Camenen and Larson (S11C2C4) bedload models also are shown in Figure 3.5. The Engelund and Fredsøe (1976) and the Nielsen (1992) models slightly overestimated, while the Meyer-Peter and Müller (1948) and the Camenen and Larson (2006) models slightly underestimated the magnitudes of erosion and deposition. Overall, the results obtained using the different bedload equations were quite close. Since the Engelund and Fredsøe model is more generally used and the results were closer to the measurements, it was used for the remaining simulations done in the current study.

The details of the early stages of flow development and streambed evolution are quite difficult to capture using experimental methods due to the rapid flow variations. Transient numerical modeling approaches can be used to capture details of the flow field as the bed evolves. The simulated flow field for different times during the early stages are shown in Figure 3.6.

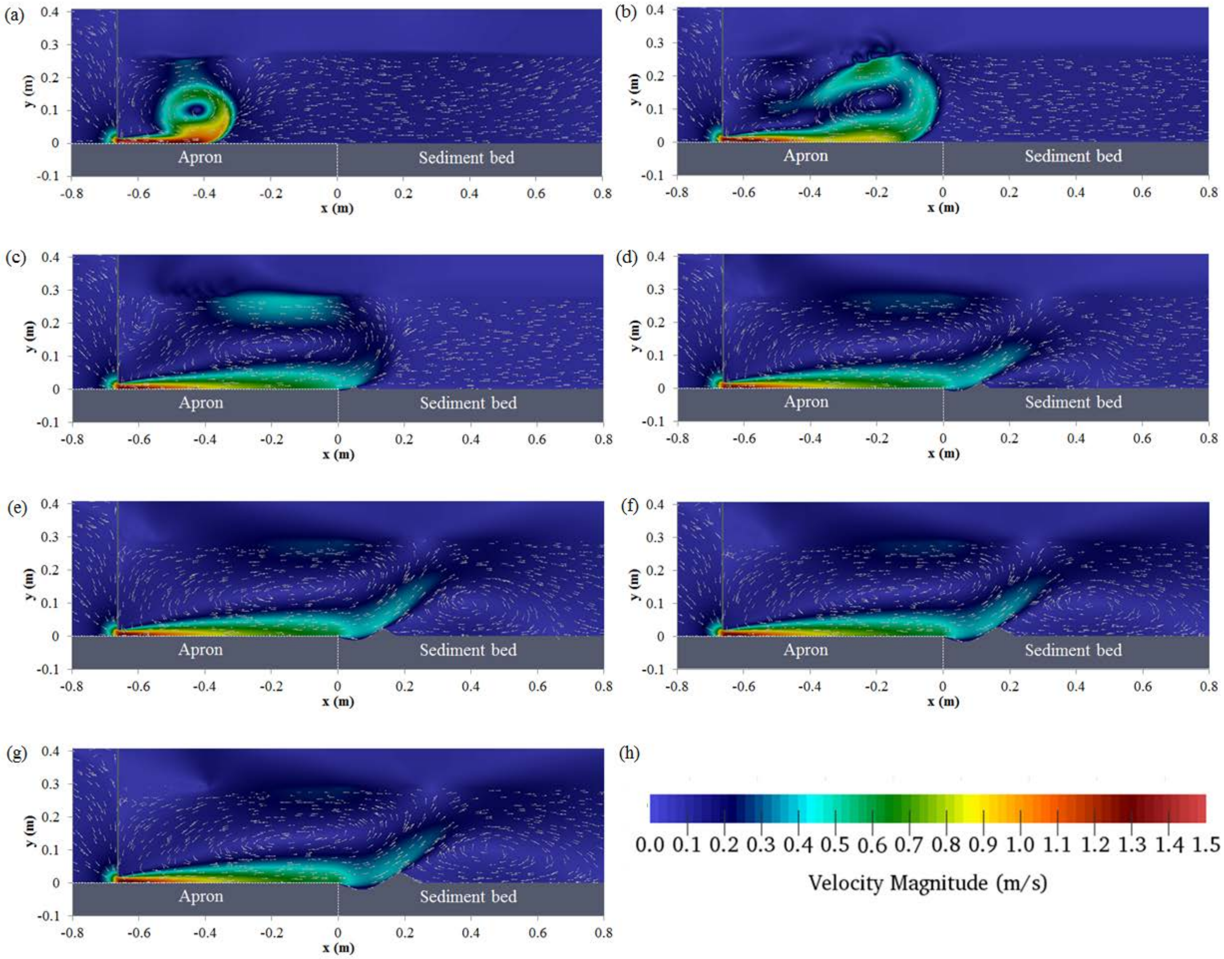

Figure 3.6 Simulated flow fields during the early stages of flow development and streambed evolution: (a) t = 1 s; (b) t = 3 s; (c) t = 5 s; (d) t = 8 s; (e) t = 12 s; (f) t = 20 s; (g) t = 30 s. The velocity color bar is shown in (h)

In the first second, the flow is discharged under the sluice gate and a submerged wall jet is formed. The flow velocity over the sediment bed is very low, so the local shear stresses caused by the flow are smaller than the critical shear stress, and, thus, no sediment scouring is observed. During the subsequent few seconds, the jet behaves like a typical submerged wall jet for a fixed bed problem, the flow velocity is higher near the sluice gate opening because of the contracted jet, and a recirculation zone arises above the jet due to the shear stresses induced by the jet, which is consistent with experimental observations by Demirel (2015). The jet diffuses as it moves along the apron because its velocity is reduced and the ambient fluid is entrained into it (Dissanayake et al., 2014), which has also been reported by Aamir and Ahmad (2016). At about the fifth second, the flow velocity over the erodible bed becomes higher, as the jet is continuously issued from the sluice gate, and a local scour hole is formed, since the shear stresses exceed the critical shear stress for sediment erosion. The flow over the sediment bed is redirected due to the existence of the bed slope, and so the submerged jet downstream of the sediment scour hole behaves like a free jet. As the jet detaches from the horizontal bed, a downstream circulation zone is formed because of the shear stresses developed at the interface between the lower boundary of the jet and the ambient fluid below the jet, which is consistent with the study of Lee et al. (2017). From about the eighth second, the flow pattern is almost steady, but the flow properties, such as the jet trajectories and circulation zones, gradually vary as the flow develops and the streambed evolves.

Figure 3.7 shows the experimental and simulated results at various times during the development of the scour hole. Chatterjee et al. (1994) reported that the downstream flow depth was 0.291 m, and the simulated water–air interface was close to this. The measured data for the bed elevations were digitized from the figures presented by Chatterjee et al. (1994), and are marked on the corresponding plots. Similarly, the previous numerical data obtained by different methods also were digitized and are shown in Figure 3.7. The experimental and numerical results showed that a scour hole occurred immediately downstream of the apron, and a sand dune formed behind the scour hole. The speed of the sediment bed evolution was very high during the early stages, and then gradually decreased. In the early stages, the agreement between experimental and proposed numerical results was quite good, except in the apron–sediment interaction zone and the dune crest. Around these two sharp corners, there are abrupt changes in velocity, eddy viscosity, and bed shear stress, which are relatively difficult for a numerical model to reproduce. After about 1,200 s, the discrepancies became more obvious. Apart from the hydrodynamic model being potentially limited in modeling the details around very sharp corners, uncertainty in the angle of repose could also contribute to these discrepancies. In the experiment, the angle of bed slope changed significantly, ranging from about 24 ° at 180 s to 50 ° at 60 s. In an experiment, the angle of bed slope may exceed the bed material angle of repose, due to the transient nature of bed evolution. In the numerical model, however, the angle of bed slope is always limited to the angle of repose, which is considered to be a fixed value for a given sand bed. Therefore, the bed slopes obtained by the numerical model were more stable than the experimental measurements. The mean root-mean square error (RMSE) was 0.0075 m, and the coefficient of determination (R^2) was 0.97. Overall, the proposed model satisfactorily reproduced the temporal variation of the bed profiles.

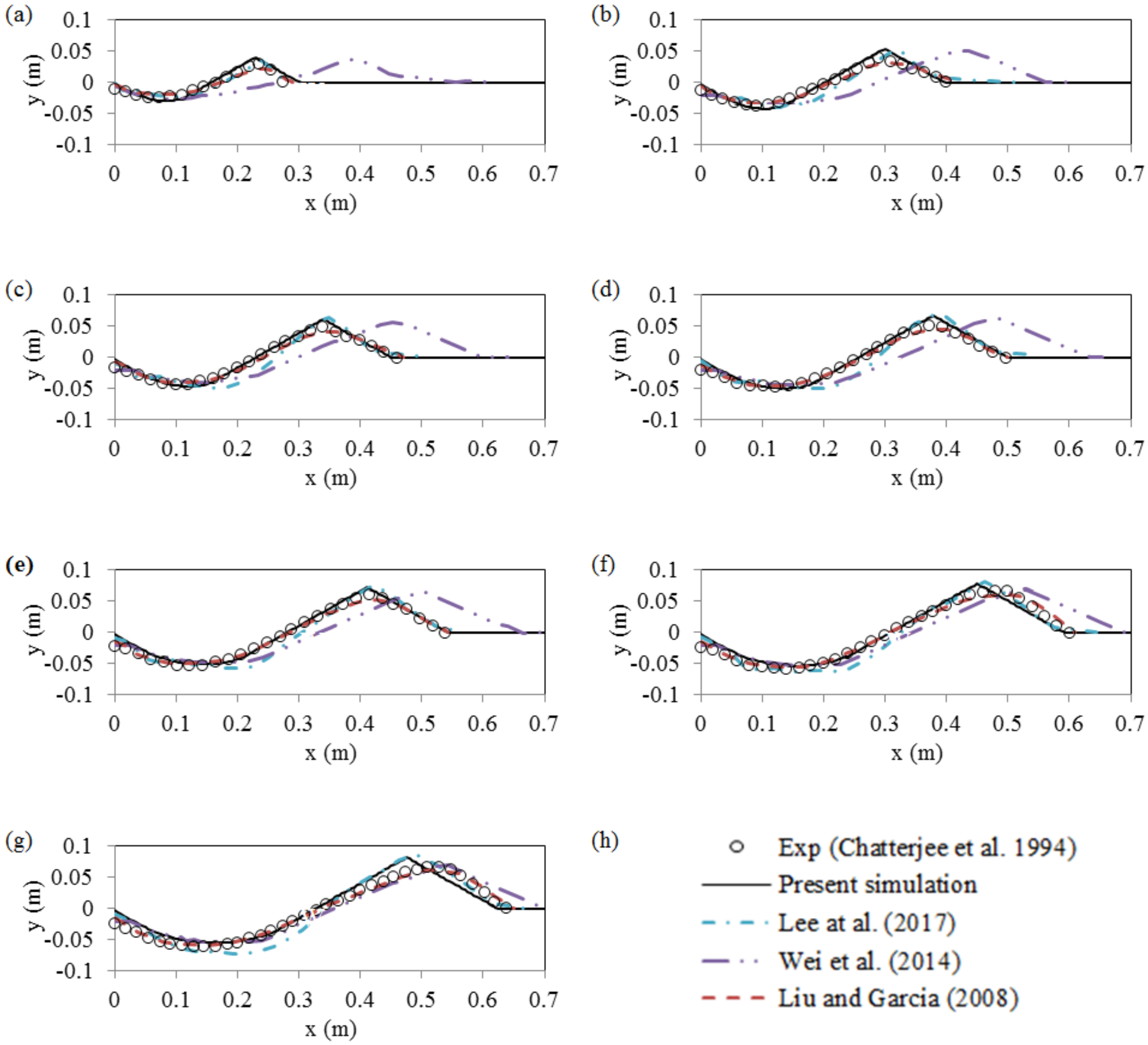

Figure 3.7 Experimental and numerical results of bed profiles at different time sequences: (a) t = 60 s; (b) t = 180 s; (c) t = 300 s; (d) t = 480 s; (e) t = 720 s; (f) t = 1200 s; (g) t = 1800 s. The legend is shown in (h)

Wei et al. (2014) used the commercial software FLOW-3D to simulate the same case, but the results substantially diverged from the measurements compared to the other results, as shown in Figure 3.7. In the simulations by Wei et al. (2014), the fractional area-volume obstacle representation (FAVOR) technique, which is an interface-capturing approach, was applied to simulate the fluid-sediment interfaces. It is well known that an interface-capturing approach typically produces less accurate results than an interface-tracking approach, thus, the proposed model obviously outperformed the FAVOR technique. The bed profiles predicted by Lee et al. (2017) and Liu and Garcia (2008) were close to the current ones.

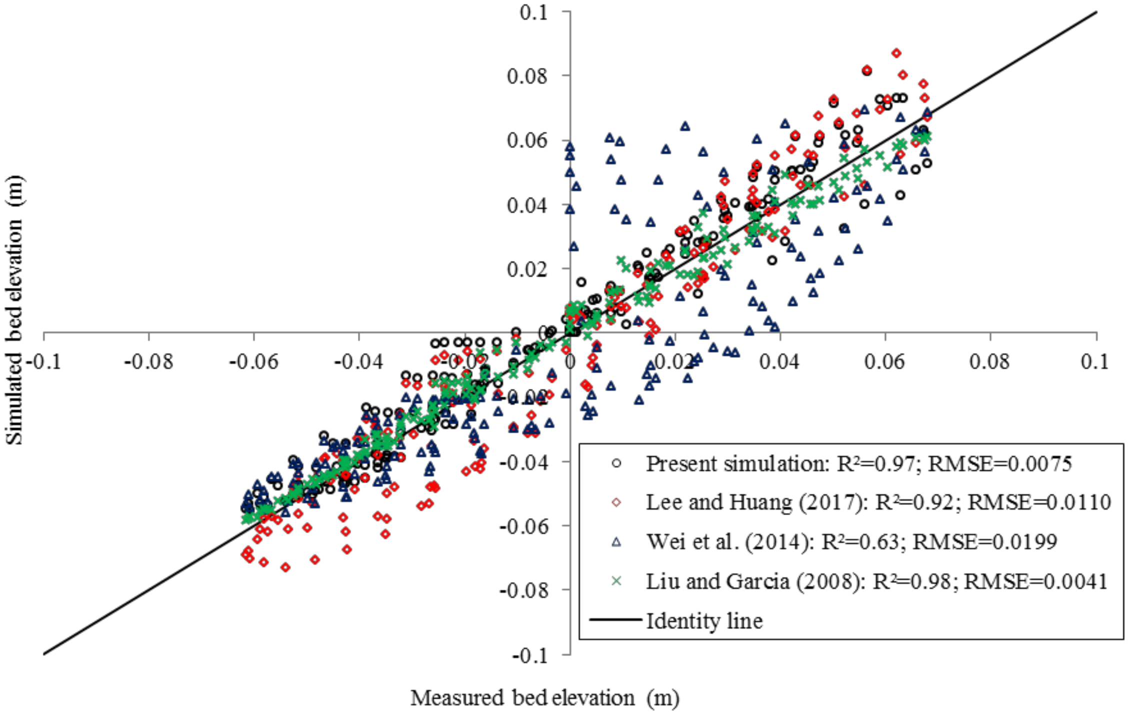

Figure 3.8 Measured versus simulated bed elevations

To obtain a clear quantitative measure of the differences between experimental data and predictions obtained using different types of models, a scatter plot of measured versus simulated bed profile elevations is shown in Figure 3.8. The values of RMSE and R^2 also are shown in the figure. Lee et al. (2017) used a three-phase model to simulate the same benchmark case; this is one of the most recent and advanced multiphase-type sediment-scour models, but its results were inferior compared to the current results. The predictions provided by Liu and Garcia (2008) were very close to and slightly better than those obtained by the current simulation. However, as stated before, the newly implemented model does not require artificial modification of the geometry, so its predictions are more objective. Overall, these results demonstrate that the capability of the proposed model is comparable to the current level of modeling practice.

3.3.3 Case C: The present experiment

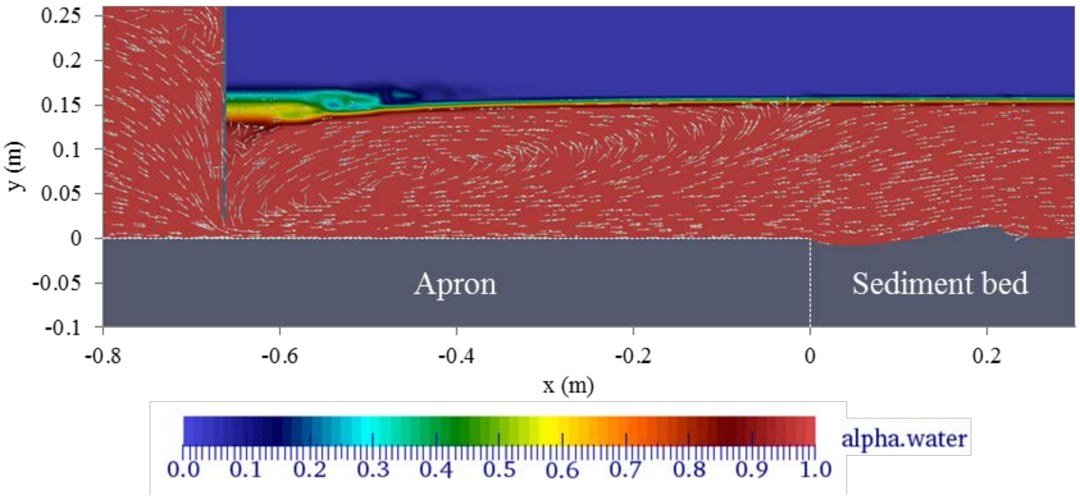

Figure 3.9 Simulated flow field and bed profile at t = 1800 s for the present experiment

The length, height, and width of the computational domain for Case C were 3.345 m, 0.265 m, and 0.005 m, respectively. The number of computational cells was 43,349. The maximum size of the grid nearest the wall at the beginning and end of the simulation for Case C was 0.00125 and 0.00129 m, respectively. The optimal value of δ was 3.5. The initial development of flow and sediment bed was similar to Case B. Two circulation zones can be observed in the simulated flow field, and the simulated location of the water–air interface was close to that of the measured interface, 0.15 m above the original water–sediment interface (Figure 3.9).

The ADV measurements and simulated velocity profiles in the equilibrium stage for the locations 0.3 and 0.4 m downstream of the sluice gate are shown in Figure 3.10. The results showed good matches between the experimental measurements and numerical predictions, thus, validating the model's capability to accurately model the submerged wall jet. The sudden reversal of the velocity profiles at approximately *y* = 0.15 m confirmed that the numerical model can predict the water-air interface very well.

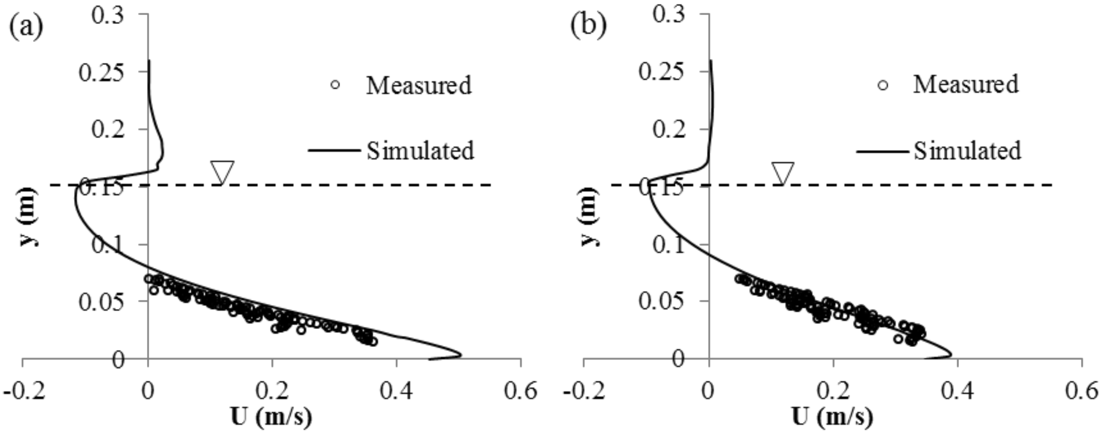

Figure 3.10 Measured and simulated flow velocity profiles: (a) at 0.3 m downstream of the sluice gate, and (b) at 0.4 m downstream of the sluice gate

The scour depth and dune height were much smaller than the flow depth, so it was quite difficult to observe the differences between the experimental and numerical results in the figures with a 1:1 ratio axis scale (as was used in Figure 3.6 for Case B). Therefore, a comparison plot, with the vertical axis stretched, was prepared (Figure 3.11).

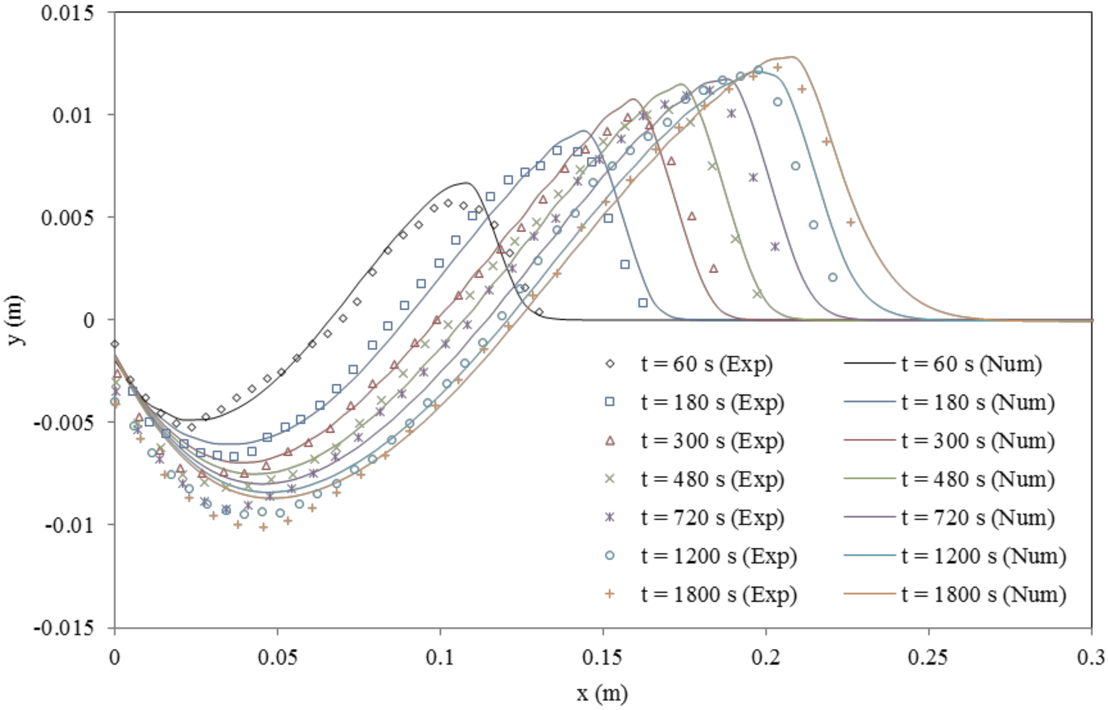

Figure 3.11 Experimental (Exp) and numerical (Num) results of bed profiles at different time sequences for the present experiment

As can be seen in Figure 3.11, the model satisfactorily captured the general trend of bed evolution. The performance of the model was relatively poor near the start of the sediment bed and at the peaks of the sand dune due to the reasons previously discussed. The simulated bed profiles closely followed the troughs and peaks of the measured points, but tended to underestimate the depth of the scour hole and overestimate the dune height. The mean RMSE was 0.00089 m, and the R^2 was 0.98. Therefore, the model predictions matched the measurements very well, confirming that the proposed model can be a reliable tool for investigating the local scour due to submerged wall jets.

3.4 Summary and Conclusions

In the current study, numerical simulations of local scour due to submerged wall jets were done using a newly implemented numerical model in OpenFOAM. The main feature of the proposed model is that it uses a novel vertex–based, terrain conformal, moving–mesh strategy to update the grids, enabling the novel advantage of allowing for more severe topographic variations without requiring artificial manipulation of the geometry. Although the moving–mesh module is vertex–based and the mesh-motion equation is solved at the mesh nodes directly, the developed code is completely compatible with the finite–volume toolbox OpenFOAM. Due to the open–source nature of OpenFOAM, the developed code can be readily modified and extended, and can be coupled with different turbulence modeling techniques and bedload equations, wall functions, and interface tracking or capturing approaches. The performance of various moving-mesh strategies, turbulence modeling approaches, interface locating techniques, and bedload equations have been investigated, and the tests and corresponding important findings are listed as follows:

- The proposed model was used to simulate a prescribed boundary motion case. The models using previous and available moving-mesh schemes also were developed and utilized to simulate the same case. The results demonstrated that the developed proposed model allows for more severe topographic variations without requiring any artificial modification of the geometry.
- The results simulated using the Meyer-Peter and Müller (1948), the Engelund and Fredsøe (1976), the Nielsen (1992), and Camenen and Larson (2006) bedload

models were compared. The Engelund and Fredsøe and the Nielsen models slightly overestimated, while the Meyer-Peter and Müller and the Camenen and Larson models slightly underestimated the magnitudes of erosion and deposition. Overall, the results obtained using the different bedload equations were quite close, but the Engelund and Fredsøe model was finally selected, as it is more generally used, and the results were closer to the measurements.

- The simulated results were compared to the experimental and the previously simulated results. The simulated results satisfactorily matched the measured data, demonstrating the capability of the proposed model in predicting local scour due to submerged wall jets. The comparisons also demonstrated that the proposed model can provide results that are comparable to or even more accurate than the commercial software Flow-3D and the latest multiphase model.
- A new laboratory experiment also was done in the current study and the proposed model accurately predicted the bed evolution, confirming that the proposed model can be used to simulate local scour problems due to submerged wall jets.

The objective of this study was to implement and validate a sediment-scour model for local scour due to submerged wall jets in OpenFOAM. Future research objectives mainly involve the utilization of the validated model in analyzing the effects of some parameters on the flow field and bed evolution, and the application of the model to some other sediment-scour problems.

3.A Appendix: The sediment scour modeling procedures

The model simulates the mesh motion using the following procedures:

- reads the user-defined coefficients and parameters in the input files,
- reads the ID labels and original coordinates of the grid points,
- extracts the ID labels and corresponding original coordinates of the grid points on the moving boundary,
- reads the updated velocity fields at all cell centers from the hydrodynamic solver,
- finds the updated velocity and coordinate components at the first cell centers adjacent to the moving boundary,
- calculates the new profile angles according to the coordinates,
- calculates the perpendicular distances between the moving boundary and the first cells adjacent to it, and the tangential velocity, according to the new profile angles,
- reads the updated viscosity and turbulent viscosity calculated by the hydrodynamic solver,
- calculates the bed shear stresses and interpolates the results to mesh nodes,
- calculates the Shields numbers at the grid points,
- selects the sediment model according to a user-defined parameter,
- calculates the dimensionless bedload transport rate at each moving boundary point using the selected bedload equations,
- calculates the absolute value of the bedload transport rate,
- calculates the modification of the bedload transport rate due to the bed slope effect using the method of Koch and Flokstra (1981),
- corrects the direction of the bedload transport rate using the direction of the bed shear stress,

- calculates the new coordinates of the moving boundary points using the sediment continuity equation,
- checks the new bed slopes and activates the sand-slide algorithm used by Khosronejad et al. (2011) if the bed slope exceeds the sediment material angle of repose,
- finds the ID labels of the internal grid points corresponding to each moving boundary point,
- calculates the new locations of the internal points according to the new moving boundary points,
- updates the mesh information, and
- resumes the hydrodynamic simulation.

Chapter 4 Numerical modeling of flow and local scour around a pipeline in steady currents using moving mesh with masked elements

Published in the Journal of Hydraulic Engineering: 2020, 146(5), 06020005. **DOI:** https://doi.org/10.1061/(ASCE)HY.1943-7900.0001740.

Yan, X., Mohammadian, A., and Rennie, C. D.

Abstract: The present work reports on a computational fluid dynamics (CFD) model for flow and local scour around a pipeline in steady currents that uses a mixed moving-mesh and fixed-grid method. It performs mesh motions for bed conforming without considering the pipeline, and then simulates the pipeline with a fixed-grid approach after the mesh motion process has been completed. The proposed model combines the best properties of the boundary-fitted-grid and fixed-grid methods. In contrast to previous boundary-fitted-grid models, the present model uses masked elements to resolve the effects of the stationary object on the flow and sediment scour processes. This approach makes it possible to track directly the moving fluid-sediment interface using a very simple mesh setup, which is more practical for engineering computations than the existing models. The modelled results are compared to published laboratory measurements as well as to previous numerical predictions obtained by other models. The results show that the proposed model satisfactorily reproduces the features of the local scour observed in the experiments, and thus can be a promising tool for modeling flow and sediment scour problems.

Keywords: local scour, pipeline, numerical modeling, boundary-fitted grids, masked

elements

4.1 Introduction

Pipelines are used in a large number of industrial applications, including the transportation of oil and gas, disposal of wastewater into the sea, and protection of communication cables (Yeganeh-Bakhtiary et al. 2011; Zhao et al. 2015). Pipelines are often placed on erodible riverbed, and the installation of such pipelines increases the bed shear stresses, turbulence and vortices, and subsequently causes severe local erosion of riverbed material. The scouring processes significantly jeopardize the structural stability of the pipelines and may result in serious safety and environmental issues (Xie et al. 2019), so a clear understanding of the flow and scouring processes is necessary for sound pipeline design and safety assessment. Complementing laboratory approaches, computational fluid dynamics (CFD) modeling has been extensively employed to study flow and sediment scour problems in recent years (Cheng et al. 2017; Lee et al. 2017), primarily because it is usually economically cheaper and less time-consuming. However, modeling flow and local scour adjacent to a static rigid object, such as a pipeline, is often challenging and requires further investigation.

Methods for simulating sediment scour problems can generally be classified into two categories, depending on how the fluid-sediment interfaces are captured or tracked. One is referred to as the “boundary-fitted-grid method” or “moving-mesh method” and the other as the “fixed-grid method” (Bigot et al. 2014). Both of these approaches have inherent advantages and disadvantages specific to the nature of the applications.

The primary objective of the present research was to develop and validate a novel numerical model for flow and sediment scour phenomena that combined the best properties of the boundary-fitted-grid and fixed-grid methods; i.e., a model that was capable of directly tracking the moving fluid-sediment interface using a very simple computational mesh setup. The present study was also motivated by a number of practical reasons. For example, preliminary studies have found that employing a purely fixed-bed method for sediment scour problems requires the modeller to accurately estimate the maximum scour depth prior to the simulations; if not, the computational domain will be too large or too small because the physical domain varies with time.

The new model performs mesh motions for bed conforming without considering the pipeline, and then simulates the pipeline with a fixed-grid approach (using masked elements) after the mesh motion has been completed. To the best of the authors' knowledge, the numerical modeling of flow and local scour using moving mesh with masked elements in OpenFOAM has not been previously reported. The phenomena of flow and local scour around a pipeline in a steady current was chosen here because this is very important in a wide arrange of industrial applications, and has been commonly used for validating numerical models (Brørs 1999; Liang et al. 2005; Zhao and Cheng 2008; Zhao et al. 2015).

It is acknowledged that the masked-element method developed in this study is in the early stages of development and has two potential limitations: first, the surface of the solid object is represented by zig-zagged cells, and second, the surface is treated as no-slip without the turbulent wall function. These two potential limitations can be compensated for with the current model by using high resolution local grids around the solid object, and may be completely avoided in future studies by introducing a better method for surface representation and treatment. The present study only simulated bedload transport and is believed valid for the present case, but its application to suspended load transport requires further investigation.

4.2 Model description

4.2.1 The bed morphology model

The temporal changes in the bed elevation are governed by the sediment continuity equation, which is a statement of sediment mass conservation and can be expressed as (Khosronejad et al. 2011)

$$(1-\gamma)\frac{\partial z_b}{\partial t} = -\nabla \cdot \mathbf{q}_B + D - E \tag{4.1}$$

where γ is the bed material porosity; z_b is the bed elevation; $\mathbf{q}_B$ is the bed–load flux vector, D is the deposition rate and E is the entrainment rate. The bedload transport was assumed to be in equilibrium so D-E=0 was adopted. The assumption is believed valid for the cases simulated in this study. The Camenen and Larson formula (2006) was used to calculate the bedload.

In addition to the equations mentioned above, a sand-slide algorithm, based on the equations used by Khosronejad et al. (2011), the Koch and Flokstra (1981) equation for the effects of bed slope, and a vertex-based moving mesh scheme (Yan et al. 2020b) were also implemented in the model. The present simulations only simulated the bedload transport, considered only one sediment size, and adopted the equilibrium transport assumption, but these limitations are believed acceptable for this study.

4.2.2 The proposed modeling approach

A schematic of the flow chart of the proposed model is presented in Figure 4.1. The model first reads the initial computational grid and simulates the flow field, with the pipeline modeled using a fixed-grid method. The moving-mesh module is then activated. It first reads the variables obtained from the hydrodynamic solver, then calculates the bed profiles, and finally updates the internal computational grids solely according to the new bed elevations. The updated mesh is then transferred back to the hydrodynamic module for further computations.

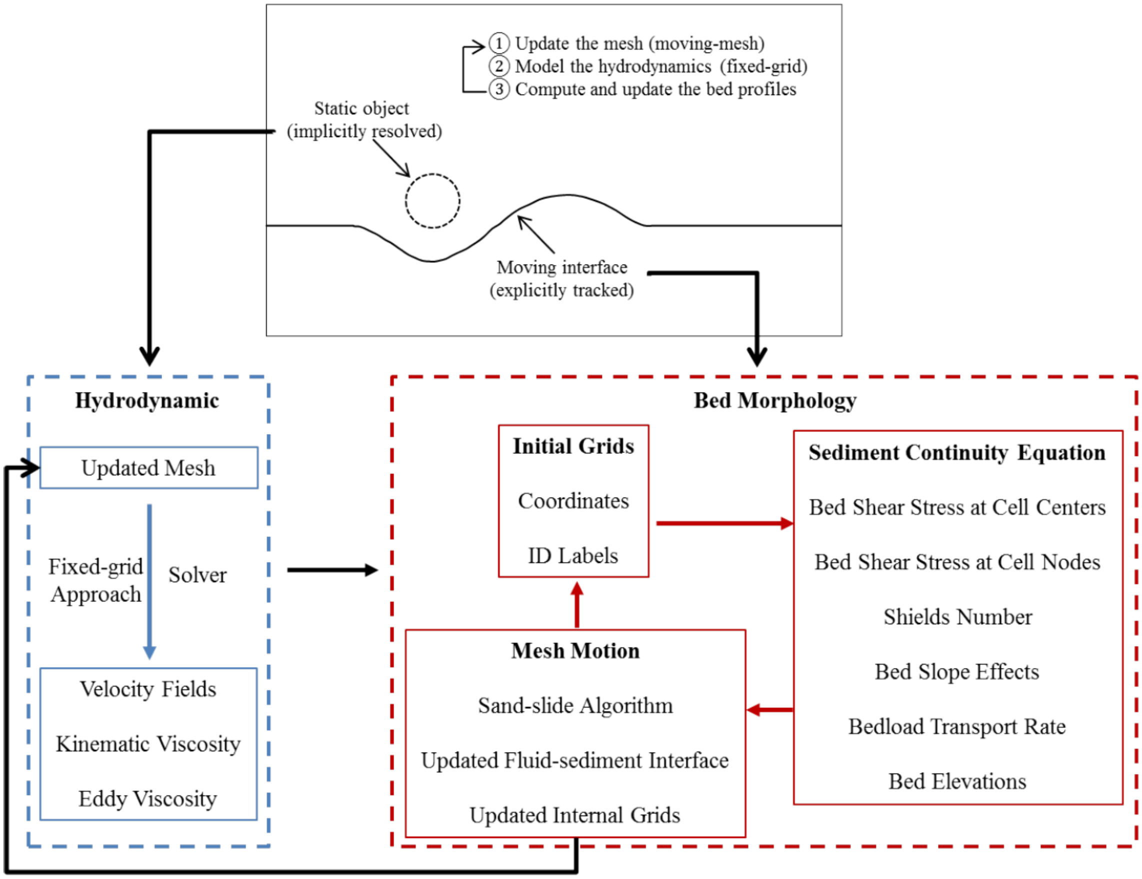

Figure 4.1 Schematic of the flow chart of the proposed model

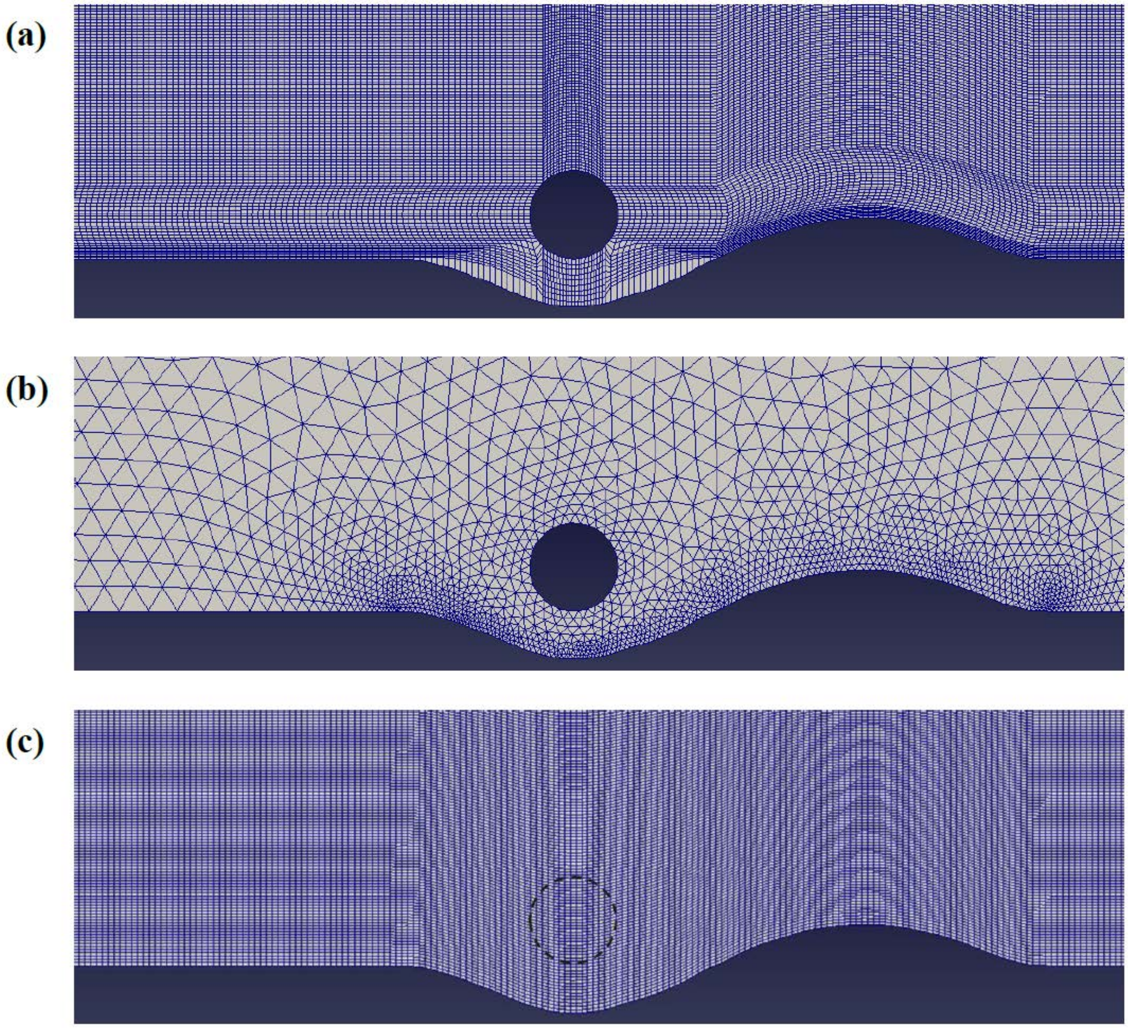

Figure 4.2 The typical patterns of computational mesh for the present method and previous boundary-fitted-grid methods: (a) previous methods using structured boundary-fitted mesh; (b) previous methods using unstructured boundary-fitted mesh; (c) the present method

Unlike a typical fixed-grid method, in which the fluid-solid interaction is captured in a fixed background mesh, the present method incorporated the effects of the rigid object (here, pipeline) in a moving mesh. Unlike a typical boundary-fitted-grid method, in which the mesh needs to fit with the boundary of the rigid object, the present model updates the internal mesh without considering the pipeline, so it is just a very simple terrain-conforming mesh, similar to that used in cases without any embedded structure above the sediment bed. The typical patterns of computational mesh for the present method and for previous boundary-fitted-grid methods obtained by preliminary simulations in this study are presented in Figure 4.2. As can be seen, the mesh setup in the present method is relatively simple, and its quality is quite high.

The present bed-conforming mesh uses a fixed number of computational grids, so it may have some disadvantages, but it is very efficient, if applicable. Consequently, this type of mesh is commonly used and uniformly accepted in the CFD community, and has been adopted in many well-recognized models or systems, such as MIKE Zero, Delft3D, Telemac 3D, and the Princeton Ocean Model.

In the present study, a masked-element approach was newly implemented in the standard OpenFOAM platform to incorporate the effects of a rigid object (here, a pipeline), aided by the standard interFoam solver. This reads the updated coordinates of the computational grid, detects the solid cells, and then imposes a no-slip condition at these cells to enforce the effects of the object on the flow and scouring processes.

4.3 Validation and applications

Jensen et al. (1990) performed point velocity measurements for a number of cross sections around a pipeline above five different scoured bed profiles in a steady current. Their work presented a comprehensive data set for fixed-bed flow and was thus used to validate the hydrodynamic module proposed here. Five fixed-bed flow simulations corresponding to the experiments by Jensen et al. (1990) were conducted, and the velocity fields were very well predicted (the averaged root-mean-squared error, R-squared value, and normalized root-mean-squared error were 3.13 cm/s, 0.86, and 9.42%, respectively).

To validate the proposed integrated numerical model, numerical simulations were carried out on the clear-water scour test reported by Mao (1986). In the experiment, the pipe diameter was 0.1 m. The flow depth was 0.35 m. The constant inflow was discharged at a mean flow velocity of 0.35 m/s. It took approximately 370 minutes for the scour to reach equilibrium, and 47% of the maximum erosion depth was reached in the first 10 minutes (Yeganeh-Bakhtiary et al. 2011). The median grain size was 0.00036 m. The model configurations were almost identical to the experimental setup. The computational domain extended from 2 m upstream of the pipeline center to 2 m downstream, horizontally, extending 0.35 m vertically. The roughness height was 0.00036 m. The angle of repose used in the simulations with the sand-slide algorithm was 36.3°. A commonly adopted sinusoidal bed profile was adopted as the initial condition of sediment bed elevation (Brørs 1999; Liang et al. 2005; Zhao and Fernando 2007; Zhao and Cheng 2008; Fuhrman et al. 2014). At the beginning stage of the scouring process, the difference in pressure between the upstream and downstream of the pipeline led to seepage flow, which washed out the sands below the pipeline, resulting in the initial erosion (Lee et al. 2016). This process cannot be modeled using a typical shear-stress-based model, such as the previous (Brørs 1999; Liang et al. 2005; Zhao and Fernando 2007; Zhao and Cheng 2008; Fuhrman et al. 2014) and present models, and so this was not a focus of the study. The simulations were run for up to 1800 s in order to compare the bed profiles at the typical time instants (Liang et al. 2005; Zhao and Cheng 2008;

Yeganeh-Bakhtiary et al. 2011). To avoid the effects of time marching schemes, the time steps of the flow field and morphology computations were both set at 0.001 s.

The experimental and numerical bed profiles at the typical time instants are compared in Figure 4.3. Brørs (1999) simulated the same experiment using a purely boundary-fitted-grid method. Liang et al. (2005) also used boundary-fitted grids for their simulations; they tested the k-ε and the Smagorinsky subgrid scale (SGS) turbulence closures. Zhao and Fernando (2007) employed an Euler-Euler coupled two-phase model embedded in the CFD package FLUENT, which is based on a fixed-grid method. These numerical results are also plotted in Figure 4.3. It can be seen that all the models predicted the scour hole reasonably well. The Liang et al. (2005) k-ε model tended to over-predict the upstream extent of the local erosion, and the scour depth in the downstream part of the scour hole. The Liang et al. (2005) SGS model predicted the upstream part of the scour hole fairly well, but also predicted deeper erosion in the downstream part. The numerical results obtained by Brørs (1999) and Zhao and Fernando (2007) were close to the present results, but the present model exhibited closer matches to the measured scour hole than the other models. The experimental results clearly show that a deposition dune was formed behind the pipeline. However, the Liang et al. (2005) SGS model failed to capture this feature, violating the sediment mass continuity in the near-bed layer. The Liang et al. (2005) k-ε model successfully predicted the existence of the downstream dune, but it substantially overestimated its size. The present model reproduced the downstream deposition very well, except at the dune crest. Around sharp edges, such as dune crests, there are abrupt changes in velocity, eddy viscosity and bed shear stress, which are very difficult for a numerical model to capture.

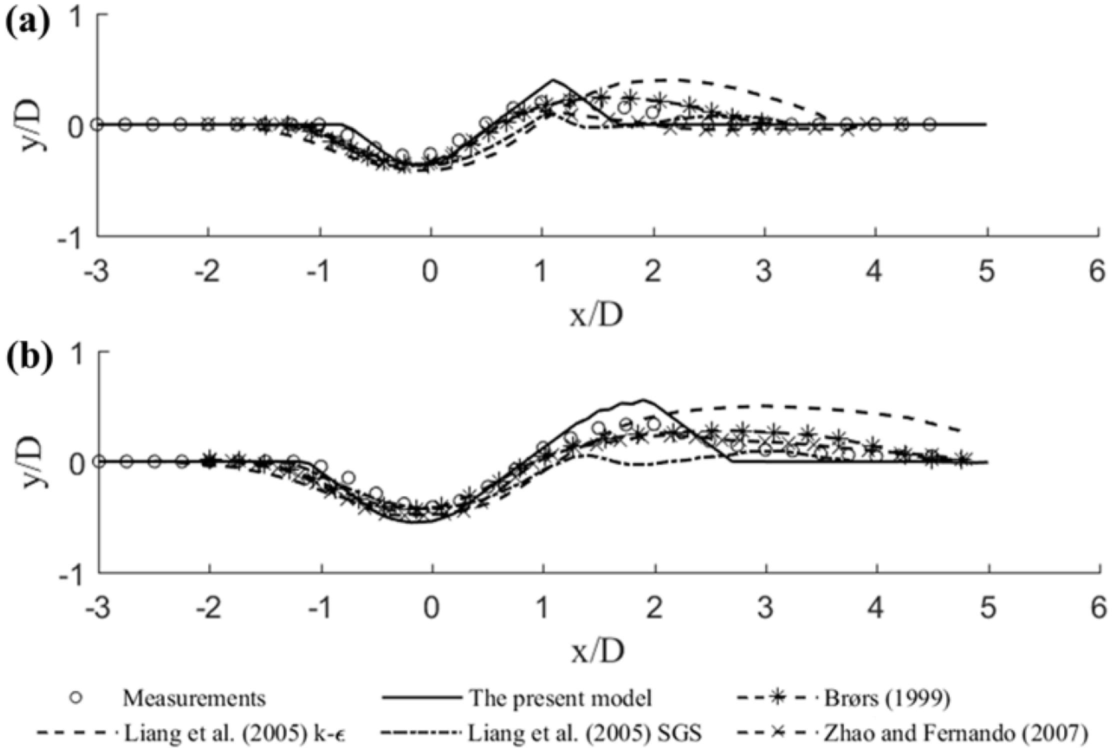

Figure 4.3 Comparison of the measured and simulated bed profiles: (a) t = 600 s; (b) t = 1800 s

The comparisons shown in Figure 4.3 validated the performance of the proposed model in modeling the flow and local scour around pipelines in a steady current.

4.4 Discussion

A major contribution of the present study is the proposed novel method for simulating the flow and local scour around a rigid object. The proposed method helps to improve moving-mesh models by introducing the fixed-mesh approach to simulate embedded structures. In contrast to previous moving-mesh methods, which use boundary-fitted grids to explicitly describe both the moving and stationary fluid-solid interfaces, the present method used a masked-element approach to implicitly describe the stationary rigid object (an embedded pipeline). A significant benefit of this approach is that the rigid object is immersed in the moving background mesh that does not need to conform to the immersed object, which substantially simplifies the mesh setup and consequently makes it possible to simulate bed morphology problems with arbitrarily complex embedded structures using a very simple mesh setup.

The pipeline is implicitly considered using the no-slip condition. It is understood that the accuracy of the flow calculation around the object may be compromised by this approximation. However, the simpler mesh setup and better numerical stability performance makes the model much more practical for engineering computations, especially in applications where the sediment erosion and deposition are of more interest than the flow around the embedded structure. The boundary around the pipeline was stepwise, and thus the pipe shape may not be perfectly interpolated. However, the good results demonstrate that this was not a major concern.

4.5 Summary and conclusions

A new numerical model for flow and sediment scour phenomena, using moving mesh with masked elements, was implemented. Compared to the existing moving-mesh models, a significant benefit of this approach is that the rigid object is immersed in the moving background mesh that does not need to conform to the immersed object, which substantially simplifies the mesh setup and consequently makes it possible to simulate bed morphology problems with arbitrarily complex embedded structures using a very simple mesh setup. The most important conclusions of the present study include

- There were no mesh problems nor any resultant numerical instabilities encountered in the present simulations for the bed evolution cases, demonstrating that the present model outperformed the typical boundary-fitted-grid methods in sustaining the simplicity and quality of computational mesh.
- The model predicted both the upstream and downstream parts of the scour hole beneath the pipeline reasonably well. It reproduced the downstream deposition very well, except at the dune crests.

The primary purpose of the present paper was to present and validate a new model. Subsequent follow-up studies should adapt and evaluate further interface-capturing schemes for the present model.

Chapter 5 Numerical modeling of local scour at a submerged weir with a downstream slope using a coupled moving-mesh and masked-element approach

Accepted by the International Journal of Sediment Research

Yan, X., Rennie, C. D., and Mohammadian, A.

Abstract: This paper presents a model for local scour at submerged weirs with downstream slopes that uses a coupled moving-mesh and masked-element approach. In the developed model, the fluid-sediment interface is tracked using a moving-mesh technique, and the effects of the structure on the hydrodynamics and bed morphology are resolved using a masked-element technique. Compared to traditional sediment scour models, based on the moving-mesh technique, the present model has the advantage of allowing for a simpler setup of the computational grids and a larger-amplitude deformation. Laboratory experiments on local scour at a submerged weir with a downstream slope were conducted, which provided bed profiles at different time instants. The results obtained by the present model are compared to the experimental data. The comparisons demonstrate the performance of the model in satisfactorily predicting local scour at a submerged weir with a downstream slope. The model was further modified and employed to carry out additional computations to investigate the influence of various parameters and sub-models.

Keywords: numerical modeling, bed morphology, submerged weir, downstream slope, moving-mesh and masked-element.

5.1 Introduction

Submerged weirs are one of the most frequently used river-training hydraulic structures, and are typically used to raise the water level and reduce the flow velocity in the upstream reach (Guan et al. 2016). Submerged weirs are often installed on erodible natural riverbeds, and the existence of these structures alters the bed shear stresses and turbulences, consequently leading to local scour. Excessive bed scour significantly impacts the stability of the hydraulic structure and ecology of the river system (Rajaratnam 1981; Wu et al., 2018), so it is important to understand better the scouring properties. Sediment scour at submerged weirs has been investigated using experimental methods (Guan et al. 2015, 2016; Wang et al. 2018a, 2018b). Complementary to such experimental methods, numerical simulations based on the computational fluid dynamics (CFD) have become quite popular in recent decades because they are typically less costly and more efficient (Dodaro et al. 2016; Elalfy et al. 2017; Mendoza et al., 2016; Fang and Rodi 2003;Fang and Wang 2000; Franz et al. 2017; Yan et al. 2020a, 2020b; Zhao et al. 2010); however, simulating local scour near a hydraulic structure, such as a submerged weir with a downstream slope, in an effective and efficient way is quite difficult and thus requires further study. To the best of authors' knowledge, numerical modeling of local scour near a submerged weir with a downstream slope has not previously been reported.

Existing sediment scour models can be categorized into either moving-mesh or fixed-grid methods. A model based on the moving-mesh approach deforms the boundary patch corresponding to the interface of interest, and moves the internal mesh according to the updated boundary patch based on certain mesh-motion equations (Charin et al. 2017). In a fixed-grid model, however, both the boundary patch and internal grids are stationary, with the effects of the interface of interest on the flow being solved by using appropriate equations or boundary conditions (Thorimbert et al. 2018). It is well known that moving-mesh approaches typically outperform fixed-grid methods in tracking a moving interface, producing more accurate predictions with the same grid resolution. However, moving-mesh approaches often lead to the deterioration of mesh quality or mesh failure, especially in cases where the geometry is complex.

In this study a numerical model is developed that can simulate the transient local scour process near a hydraulic structure, such as a submerged weir with a downstream slope, by using an improved moving-mesh approach (Yan et al. 2020a, 2020b). In the model, the fluid-sediment interface is tracked using a moving-mesh technique, and the effects of the structure on the hydrodynamics and bed morphology are resolved using a masked-element technique. Compared to traditional sediment scour models, based on the moving-mesh technique, the present model has the advantage of allowing for a simpler setup of the computational grids and a larger-amplitude deformation, and is thus more effective and efficient for practical engineering applications. To the best of the authors' knowledge, the application of the present modeling technique to local scour caused by sloped submerged weirs, has not previously been reported.

5.2 Methodology

5.2.1 Experimental methods

An experiment was performed using a recirculating flume (Figure 5.1). A constant discharge was supplied, upward through the inlet section, which was 0.35 m long (L_i). The discharge per unit width was 0.005 m^2/s. A downstream-sloped weir was placed at 1 m downstream of the inlet section (L_u). The top length of the weir was 0.01 m (L_w), the height above the sediment bed was 0.03 m (h_w), and the weir slope was 45°. An overflow weir was positioned at 1.06 m downstream from the upstream edge of the sloped weir (L_d), and its height above the sediment bed was 0.015 m. The sediment bed was paved with quartz sand with a median grain diameter of 0.001 m. The default critical Shields parameter was estimated to be 0.0314.

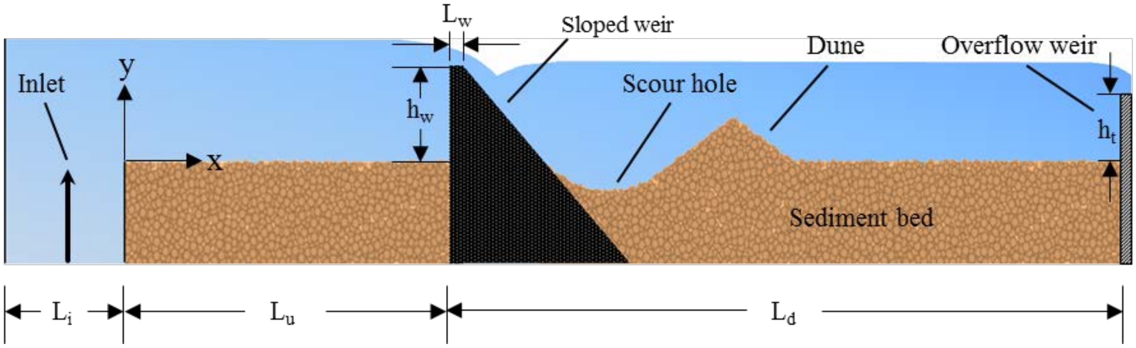

Figure 5.1 Sketch of the experimental setup

Before the experimental test, a very small flowrate was supplied by the recirculating pump for the upstream section and a water hose for the downstream section. The slow water supply saturated the sediment bed and generated an initial water depth of 0.03 m for the upstream section and 0.015 m for the downstream section. After the preparatory work was completed, the inflow was supplied with the target flowrate for specific time duration, and the bed elevations along the centerline were measured using a point gauge. The same procedures–from experimental preparation to measurement–were repeated for the other time durations, and thus the present experiments provided a dataset of the bed profiles at different time instants.

5.2.2 The hydrodynamic model

The present model was implemented within the framework of OpenFOAM (Open source Field Operation And Manipulation), which is a free and open source CFD toolbox. The three-dimensional (3D) Reynolds–Averaged Navier–Stokes equations (RANS) for mass and momentum conservation can be expressed as follows:

Continuity:

$$\nabla \cdot \mathbf{U} = 0 \tag{5.1}$$

Momentum:

$$\frac{\partial \rho \mathbf{U}}{\partial t} + \nabla \cdot \left(\rho \mathbf{U}\mathbf{U} \right) = \nabla \cdot \mathbf{T} + \rho \mathbf{g} - \nabla p \tag{5.2}$$

where $\mathbf{U}$ is the flow velocity vector; ρ is the fluid density; t is the time; $\mathbf{T}$ is the viscous stresses tensor; $\mathbf{g}$ is the gravitational acceleration vector; and p is the pressure (Yan et al. 2020b). The so-called “empty” boundary condition available in OpenFOAM was used in this study, so the simulations were reduced to two-dimensional.

As for turbulence modeling, the re-normalisation group (RNG) k-ε turbulence closure was utilized, which can be expressed as follows:

$$\frac{\partial k}{\partial t} + \frac{\partial k u_i}{\partial x_i} - \frac{\partial}{\partial x_i}\left(D_{keff} \frac{\partial k}{\partial x_i} \right) = G - \varepsilon \tag{5.3}$$

$$\frac{\partial \varepsilon}{\partial t} + \frac{\partial \varepsilon u_i}{\partial x_i} - \frac{\partial}{\partial x_i}\left(D_{\varepsilon eff} \frac{\partial \varepsilon}{\partial x_i} \right) = \left(c_{1\varepsilon} - R_{\varepsilon} \right) \frac{\varepsilon}{k} G - c_{2\varepsilon} \frac{\varepsilon^2}{k} \tag{5.4}$$

where k is the turbulent kinetic energy, u_i is the instantaneous velocity component in the direction x_i, ε is the turbulent energy dissipation rate, G is the production of turbulence due to shear; D_{keff} and $D_{\varepsilon eff}$ are the effective diffusivity for k and ε, respectively; R_ε is an RNG term that corrects the ε equation (Appendix 5.A3); σ_k, σ_ε, $c_{1\varepsilon}$, $c_{2\varepsilon}$, c_μ, η_0, and β are model constants equal to 0.71942, 0.71942, 1.42, 1.68, 0.0845, and 0.012 respectively (Yan et al. 2020d). The initial values of k and ε at both the internal field and boundary fields were initialized by the calculated values at the inlet using the following equations (Paul et al. 2011):

$$k = \frac{3}{2}\left(\overline{u}I\right)^2 \tag{5.5}$$

$$\varepsilon = C_\mu^{\ 3/4}\frac{k^{3/2}}{l} \tag{5.6}$$

where $\overline{u}$ is the average velocity, translated from the flow discharge, under the sluice gate; I is the turbulence intensity; l is the turbulence length scale. The turbulence intensity is estimated by

$$I = 0.16\left(\mathrm{Re}\right)^{-1/8} \tag{5.7}$$

where Re is the Reynolds number, determined by

$$\mathrm{Re} = \frac{\rho\overline{u}L}{\mu} \tag{5.8}$$

where L is the characteristic length, and μ is the dynamic viscosity.

The turbulence length scale is approximated by

$$l = 0.07L \tag{5.9}$$

5.2.3 The bed morphology model

The variations in the bed profiles can be calculated using the sediment continuity equation, which is given by (Khosronejad et al. 2011; Paola and Voller 2005)

$$\left(1-\gamma\right)\frac{\partial z_b}{\partial t} = -\nabla \cdot \mathbf{q}_B + D - E \tag{5.10}$$

where γ is the bed material porosity; z_b is the bed elevation; $\mathbf{q}_B$ is the bed–load flux vector, D is the deposition rate and E is the entrainment rate. In this study, D–E was assumed to be zero because the bedload transport was found to be the dominant mode of transport in the present case. This assumption may impact the predictions very close to the weir but can significantly simplify the model. The bedload flux vector consists of two elements, the bedload transport rate in stream–wise and transverse directions, respectively. They can both be described in the dimensionless form as

$$q_i^* = \frac{q_{Bi}}{\sqrt{g\left(\frac{\rho_s}{\rho_w}-1\right)d^3}} \tag{5.11}$$

where q_{Bi} is the bedload transport rate in the i–th direction, and q_i^* is the corresponding dimensionless form; ρ_s is the density of the bed material; and d is the grain diameter.

To calculate the bed–load, the Engelund and Fredsøe formula (1976) was applied

$$q_i^* = \begin{cases} 18.74(\theta_i - \theta_c)\left[\sqrt{\theta_i} - 0.7\sqrt{\theta_c}\right] & if\ \theta_i > \theta_c \\ 0 & if\ \theta_i \le \theta_c \end{cases} \tag{5.12}$$

where θ_i is the Shields number; and θ_c is the critical Shields number. More details about the Shields number and the wall function are provided in Section 5.A1.

The sand–grain roughness height can be estimated based on the sediment diameter d_χ (χ represents the percentage of sediment that is finer),

$$k_s = \delta d_{50} \tag{5.13}$$

where d_{50} is the median grain size; δ is an empirical coefficient with a default value of 1. There is tremendous scatter in the reported values of δ (Apsley and Stansby 2008; Millar 1999), and further discussion about it will be provided in Section 5.4.2.

A bed-slope-effect model proposed by Koch and Flokstra (1981) and a vertex-based moving mesh scheme implemented by Yan et al. (2020a, 2020b) were also incorporated into the model. The mesh scheme can be expressed as

$$h_{new} = H_{\max} - \frac{H_{\max} - h_{initial}}{H_{\max}} \times (H_{\max} - H_{\min}) \tag{5.14}$$

where h_{new} is the new coordinate of an internal node; H_{max} is the coordinate of the top boundary; $h_{initial}$ is the initial coordinate of the node; and H_{min} is the coordinate of the bottom boundary. The sediment roughness height was assumed to be equal to the median grain size, and the critical Shields number was estimated based on the Soulsby-Whitehouse equation (Soulsby and Whitehouse, 1997). Sand–slide events occur when the bed slope exceeds the sediment material angle of repose, the steepest angle at which a material can be piled without slumping. The algorithm adopted by Khosronejad et al. (2011) is implemented in the present model to take this phenomenon into account. The sand-slide model has been previously reported in Yan et al. (2020a, b), and more details are provided in Section 5.A2.

5.2.4 The coupled approach

To model the influences of the embedded structure (here, a downstream sloped submerged weir) on the flow and scouring processes, the masked-element approach proposed by Yan et al. (2020a) was utilized. The approach first simply updates the internal grid, with respect to the corresponding grids at the sediment bed, and then detects the cells for the solid and imposes a no-slip boundary condition on the cells. Unlike a typical moving-mesh model, the present model does not consider the existence of the embedded structure when it updates the computational grids, and thus the resultant mesh has a higher level of quality and lower level of complexity. Different from a typical fixed-grid model, the model explicitly tracks the water-sediment interface, and thus provides straightforward and accurate results.

5.2.5 Model setup

In all the simulations performed in this study, the maximum Courant number was set to 1. The temporal term was discretized using the Euler scheme. The gradient term and Laplacian terms were discretized using the Gauss linear scheme. The divergence terms were discretized using the Gauss linear, Gauss vanLeer, and Gauss upwind schemes. The linear method was used for interpolation schemes. The preconditioned conjugate gradient

(PCG) method and diagonal incomplete Cholesky (DIC) pre-conditioner were used for the pressure field with a tolerance of 10-7. An iterative solver for symmetric and asymmetric matrices that uses a run-time selected smoother to converge the solution to the required tolerance was used for the velocity field; to reduce the mesh dependency of the numbers of iterations, the Gauss Seidel technique was utilized, which is an improved version of the Jocobi method. These algorithms were employed because they performed better than others in terms of computational efficiency, accuracy, and stability for the present cases. Further details regarding these algorithms can be found in Behrens (2009) and Holzmann (2016). To validate and evaluate the model, two sets of cases were considered: 1) flow over a broad-crested weir; and 2) bed erosion downstream of a sloped weir. The simulation time for the former case was set as 50 s, after which the numerical results became approximately unchanged. The simulation time for the latter case was set as 1200 s, which is consistent with the experiment.

5.3 Model validation and evaluation

5.3.1 Flow over a broad-crested weir

Sarker and Rhodes (2004) collected the free-surface profile over a laboratory-scale, rectangular broad-crested weir. Although the model geometry is very simple, the flow dynamics associated with this test is complex because of the existence of flow separations. Their work presented a high-quality data set for fixed-bed flow and was thus used to validate the hydrodynamic module proposed here. In the experiment, the length and width of the channel were 3.162 m and 0.105 m, respectively. The length and height of the weir were 0.4 m and 0.1 m, respectively.

The numerical model was configured to represent the actual experimental conditions. The masked-element approach proposed by Yan et al. (2020a) was utilized to describe the weir. The computational domain ranged from -0.558 m to 3.162 m in the horizontal direction and 0.25 m in height. Additional simulations were performed with larger computational domains, and the results in the area of interest were found to be almost identical to the final results. The mesh resolution was determined with an independency tolerance of 2%. A uniform velocity of 0.0799 m/s was imposed at the upstream inlet section. A zero-gradient boundary condition was assigned to the downstream outflow boundary. A boundary condition called "inletOutlet" was assigned to the atmosphere as explained in the following. When there is no backward flow, the boundary condition becomes the zero–gradient open boundary condition. When there is backward flow, the boundary condition automatically becomes a fixed–value boundary condition. The so-called "empty" boundary condition available in OpenFOAM was used for the front and back patches, so the simulation was reduced to two-dimensional. The simulation was run for up to 50 s. A value of 0.001 s was used as the default time step interval, but the actual time step was automatically adjusted based on the numerical stability criterion.

Sarker and Rhodes (2004) reported the measured free surface elevations at various locations. Here, data were digitized from the plots presented by Sarker and Rhodes (2004) and are presented in Figure 5.2, which also contains the time-averaged free-surface profile obtained by the numerical model.

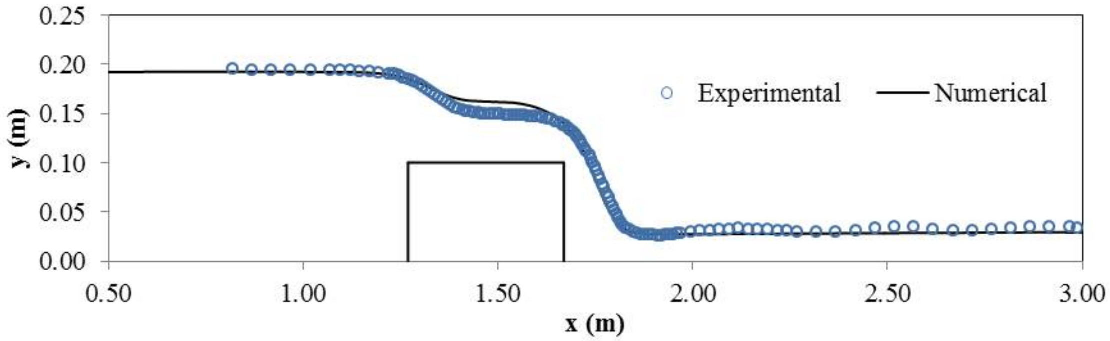

Figure 5.2 Comparison of the measured (symbols) and simulated (solid lines) free surface profile

To obtain a quantitative measure of the difference between the data and predictions, various performance indicators were calculated. The mean absolute percentage error was 6.99%, the mean relative error was -3.07%, the mean absolute error was 0.0054 m, the root-mean-squared error was 0.0069 m, the R-squared value was 0.99, the mean bias error was -0.0002 m, and the normalized root-mean-squared error was 0.066.

The numerical models correctly predicted the overall shape of the free-surface profiles, as the R^2 value was very close to 1. The free-surface elevations provided by the present model showed an excellent match with the experimental data and the RMSE values were quite low. The present model performed relatively poorly at the locations immediately above weir. This revealed the incapability of the present method to accurately resolve the flow field very close to the weir-water interface. However, the good agreement between the measured and simulated results for surrounding locations demonstrated that low prediction accuracies only occurred immediately adjacent to the weir boundary.

5.3.2 Bed erosion downstream of a sloped weir

To validate the proposed integrated numerical model, numerical simulations were carried out on the present scour test. The model setup was mainly determined according to the experimental conditions. The computational domain was 2.44 m in length and 0.1 m in height. The mesh resolution was determined following the mesh sensitivity analysis procedures used by Yan and Mohammadian (2017, 2019) and Yan et al. (2019, 2020a, 2020b, 2020c) with a tolerance of ± 0.001 m. A uniform velocity of 0.0143 m/s was imposed at the upstream inlet section. A boundary condition called “inletOutlet” was assigned to the atmosphere. A zero–gradient open boundary condition was used for the outlet. The no-slip boundary condition was assigned to the sand bed patch and the standard rough wall function in OpenFOAM was applied. The boundary conditions at the front and back patches were set to “empty,” so the simulation was reduced to a 2D case. It was observed in the experiments that the sands were washed out by the flow surge instead of being eroded by the shear stress when the sand layer between the sediment surface and weir surface was thin. This phenomenon seems to be due to the combined effects of shear stress, pressure difference, seepage flow and turbulence, and thus it cannot be satisfactorily predicted using a traditional sediment transport model based on the shear stress theory. In the present study, this process was modelled by correcting the critical Shields number when the layer thickness was below a certain threshold, which is believed to be a simple and practical approach. The optimal values of the corrector for the critical Shields number and the threshold for the sand layer thickness were determined by comparing the experimental and numerical data at one time instant, and can be justified using the data at subsequent time instants. In the present study, the time step was set to be

0.001 s for both the hydrodynamic and bed morphology simulations in all simulations. Additional simulations were performed with smaller values for the time step, and the results were found to be almost identical to the final results. The considered cases are summarized in Table 5.1. In the table, δ is the coefficient for roughness height estimation, ϕ is the angle of repose, S_r is the range of random numbers in a stochastic model, Δd_c is the layer width for corrections of critical Shields number, γ is the corrector for the critical Shields number, L_s is the length for a second sand-slide model, and *TM* indicates the turbulence model. The sensitivity of the model results to these parameters will be reviewed in the Discussion section. The run S25 was the final simulation for this study. In this simulation, δ was set as 1 because it is the default value; ϕ was set as 45°, which is consistent with the experimental observations; Δd_c and γ were set to be 0.03 and 0.01 based on model calibrations. The methods using the parameter S_r and L_s were not employed in this simulation because they may cause more uncertainties although tuning them may further improve the match between numerical and experimental results.

Table 5.1 Parameters of the simulated cases

Case	δ	ϕ	S_r	Δd_c	γ	L_s	TM
S01	2.5	29	—	—	—	—	k-ε
S02	2.5	29	—	—	—	—	k-ω SST
S03	2.5	45	—	—	—	—	k-ω SST
S04	2.5	29	—	—	—	—	RNG k-ε
S05	1.0	29	—	—	—	—	RNG k-ε
S06	1.5	29	—	—	—	—	RNG k-ε
S07	2.0	29	—	—	—	—	RNG k-ε
S08	2.5	45	—	—	—	—	RNG k-ε
S09	1.0	45	—	—	—	—	RNG k-ε
S10	1.5	45	—	—	—	—	RNG k-ε
S11	2.0	45	—	—	—	—	RNG k-ε
S12	1.0	29	[0.5, 1.5]	—	—	—	RNG k-ε
S13	1.0	45	[0, 2.0]	—	—	—	RNG k-ε
S14	1.0	45	—	0.01	0.01	—	RNG k-ε
S15	1.0	45	—	0.01	0.05	—	RNG k-ε
S16	1.0	45	—	0.01	0.1	—	RNG k-ε
S17	1.0	45	—	0.01	0.15	—	RNG k-ε
S18	1.0	45	—	0.01	0.2	—	RNG k-ε
S19	1.0	45	—	0.01	0.3	—	RNG k-ε
S20	1.0	45	—	0.02	0.05	—	RNG k-ε
S21	1.0	45	—	0.02	0.1	—	RNG k-ε
S22	1.0	45	—	0.02	0.15	—	RNG k-ε
S23	1.0	45	—	0.02	0.2	—	RNG k-ε
S24	1.0	45	—	0.02	0.3	—	RNG k-ε
S25	1.0	45	—	0.03	0.01	—	RNG k-ε
S26	1.0	45	—	0.03	0.05	—	RNG k-ε
S27	1.0	45	—	0.03	0.1	—	RNG k-ε
S28	1.0	45	—	0.03	0.15	—	RNG k-ε
S29	1.0	45	—	0.03	0.2	—	RNG k-ε
S30	1.0	45	—	0.03	0.3	—	RNG k-ε
S31	1.0	45	—	0.03	0.01	0.035	RNG k-ε

The measured and simulated (S25) bed profiles for two time-sequence samples are presented in Figure 5.3. In a typical sediment scour phenomenon, a sharp downstream dune is often formed, but neither the present experimental nor numerical results showed a sharp dune. The sharpness of the peak depends on the flow conditions and varies with time. In the current case, the downstream water was very shallow, so the sediment dune was found to be quite flat. Overall, the model predicted the bed profiles satisfactorily, especially for the downstream dune. The predictions for the bed elevations very close to the submerged weir were less accurate than those for the other locations. Adjacent to the weir, the sediment motions were induced by the combined effects of shear stress, pressure difference, seepage flow and turbulence, and thus the mechanisms were complicated, making simulation difficult. The root-mean-squared error and R-squared value (Shcherbakov et al. 2013) for the time instant 600 s were 0.003 m and 0.94, and those for 1200 s were 0.003 m and 0.95, demonstrating that the model can reasonably reproduce the bed profiles downstream of the sloped submerged weir.

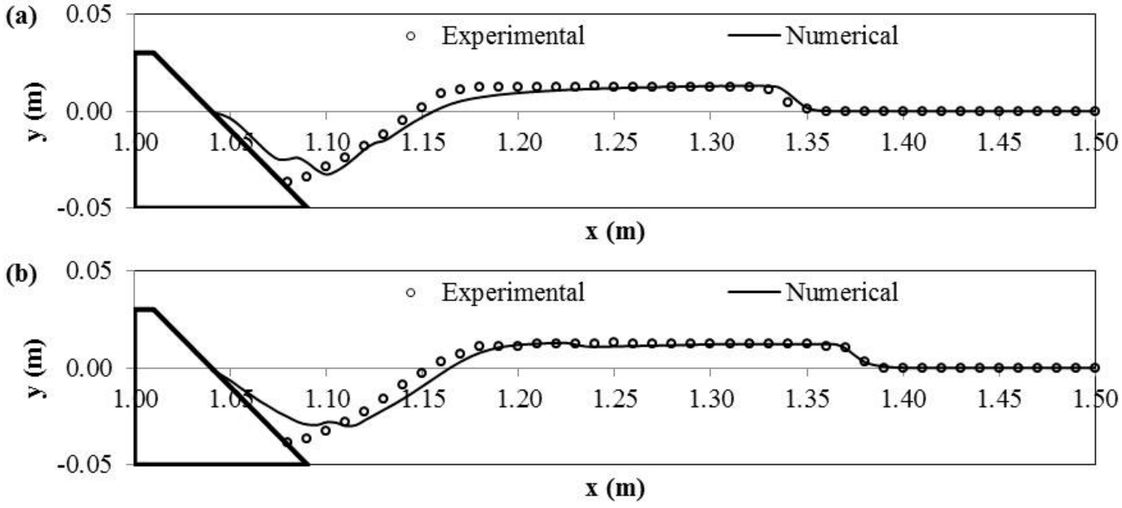

Figure 5.3 Measured and simulated bed profiles: (a) t = 600 s; (b) t = 1200 s

5.4.1 Advantages of the model

A major factor hindering the wide spread use of moving-mesh models is the problem of mesh failure. For simple and small boundary deformation, a typical moving-mesh method works very well. However, for cases with more complicated or larger mesh deformation, the grids at different levels may intersect each other, generating negative grid volume, and causing the simulation to be unstable. For example, Figure 5.4 demonstrates a deforming mesh problem in which the boundary patch downstream of the cell C_L is moving upwards at a constant velocity of U_B, while the one upstream of C_L is stationary. Using the typical moving-mesh approach, the solved motion velocity of the internal node, N_I, can be much smaller than the motion velocity of the boundary node, N_B, which moves at the same speed as the boundary. Eventually, an internal level intersects the bathymetry which causes the simulation to fail. This is a very common and serious problem of the moving-mesh approach, which has significantly hindered its wider use.

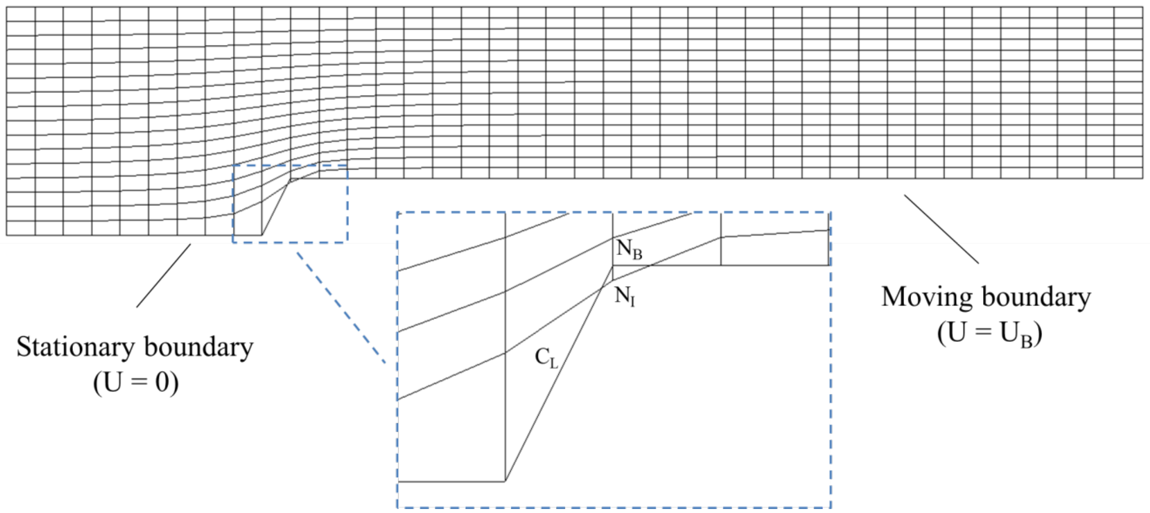

Figure 5.4 Sketch of a typical deforming-mesh problem

Figure 5.5 (a) presents a typical structured boundary-fitted mesh for the present case. Its quality typically became quite poor after a few steps of bed evolutions. The aspect ratio of the points near the downstream face of the weir may become very large and the changes in grid size may become quite abrupt, causing numerical instability and inaccuracy. The mesh quality can be improved by using a very high grid resolution or a complicated dynamic mesh scheme, but the computational efficiency would then be greatly lowered. The grids at different levels may also intersect with each other when the bed deformation becomes very large, resulting in mesh failure, as explained in Figure 5.4.

Figure 5.5 (b) presents a typical unstructured boundary-fitted mesh. This type of mesh can ensure a good initial mesh quality, and thus is very suitable for simulating flow in cases with complex geometries. However, the mesh quality significantly deteriorates when the flow-sediment interface moves. A good mesh quality can be maintained by using an appropriate moving-mesh strategy that is suitable for unstructured grids, but this is currently too complicated and has not been adequately handled, and so this approach is not very practical for cases with moving boundaries.

Figure 5.5 (c) shows a typical mesh used in the present method. As can be seen and discussed above, the mesh setup is quite simple and the quality can be kept very high. There were no mesh failures, and nor was any resultant numerical instability encountered in the simulations while using the present approach, which frequently occurred when using the typical boundary-fitted-grid methods. This merit associated with mesh setup and quality is the most important advantage of the present model.

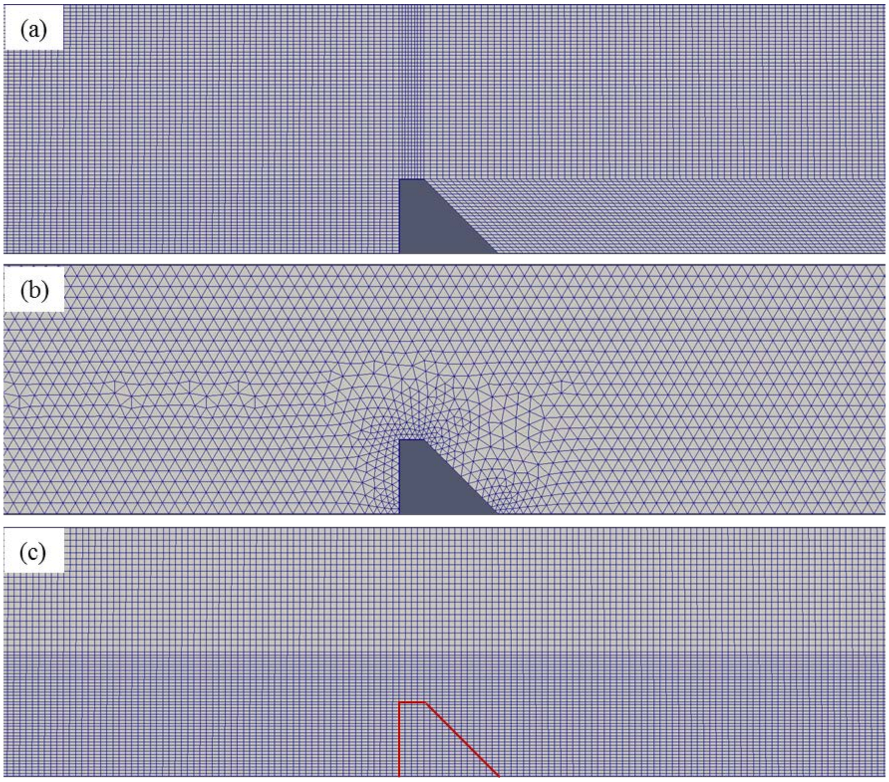

Figure 5.5 Comparison of different patterns of computational grids: (a) a standard structured mesh; (b) a standard unstructured mesh; (c) the mesh for the present approach. The maximum and minimum grid sizes are 0.001 m and 0.01 m, respectively.

5.4.2 Influences of parameter estimations

By definition, k_s should be approximately equal to the sediment diameter for uniform boundary sediment and to mean or d_{50} for non-uniform boundary sediments, and thus $k_s = d_{50}$, which defines a lower bound estimate of flow resistance, is one of the most popular and well recognized assumptions (Kashyap et al. 2012; Kironoto et al. 1994; Millar 1999; Nikuradse 1950; Yan et al. 2020a). There is tremendous scatter in the reported values of k_s, probably due to variable bed forms and surface irregularities (Apsley and Stansby 2008; Millar 1999). Van Rijn (1982) reported that k_s for a plane bed ranges from $k_s = 1.25d_{35}$ to $k_s = 5.1d_{84}$; Bray and Davar (1987) assumed $k_s = 3.5d_{84}$ or $k_s = 6.8d_{50}$ for gravel–bed rivers; Apsley and Stansby (2008) used a value of $k_s = 2.5d_{50}$ to model bedload sediment transport on large slopes; Khosronejad et al. (2007) adopted a value of $k_s = 3d_{50}$ to simulate the flow and sediment transport in laboratory channel bends; Fang et al. (2016) adjusted the value of k_s until the correlation coefficient between calculated and measured data was more than 0.95. The estimation of sand–grain roughness height remains an open topic, and it is a common practice to calibrate numerical models by adjusting the empirical coefficient. The bed forms and surface irregularities of a sediment bed are difficult to measure using experimental methods, so it is practical to estimate these properties by determining the value of δ using a numerical model. In the final simulation in the present study, the default value of 1 was used for δ (i.e, k_s = d_{50}), but various simulations with different values of δ have been performed to investigate its influence. The bed profiles at 600 s obtained with different roughness height coefficients are presented in Figure 5.6. As can be seen, the differences in the results near the weir were not obvious, but the downstream dune extended further with increasing values of *δ*. According to this comparison, the magnitude of the bed elevations predicted using the default value of *δ* (i.e., 1.0) was closer to the experimental data than those predicted using other values of *δ*.

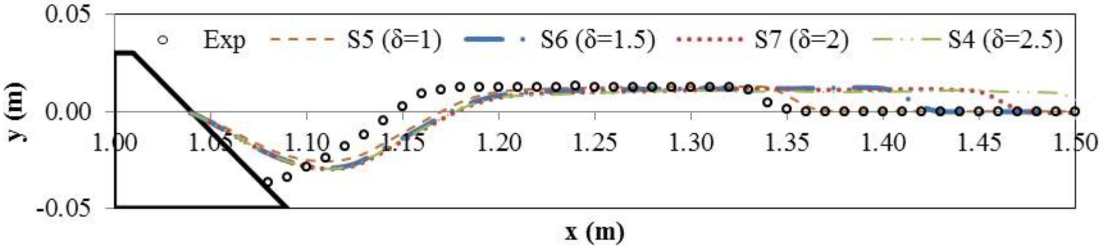

Figure 5.6 Comparison of bed profiles at t = 600 s obtained with different roughness height coefficients

The sediment material angle of repose is the steepest angle at which a material can be piled without slumping. Therefore, the angle of repose is the maximum allowable angle that could occur in the numerical results. The angle of repose ranges from 0° to 90°, primarily affected by the nature of the materials. For example, the angle of repose for clay approximately ranges from 25° to 40°, that for water-filled sand approximately ranges from 15° to 30°, and that for wet sand is approximately 45° (Glover 1995). It has been observed in the present experiment that the maximum angle was about 45°, so the angle of repose for the final simulation was set to be 45°, but various simulations with a different typical value (i.e., 29°) were also conducted to see how the values of angle of repose affect the numerical results. The bed profiles at 600 s obtained with different values of angle of repose are compared in Figure 5.7. As can be seen, the numerical results were quite different, indicating that the influence of the value of angle of repose on the prediction was quite significant. The value of angle of repose did not significantly affect the results when the k-ω SST turbulence model was utilized, partially because the magnitude of the bed evolutions predicted by the k-ω SST turbulence model was quite low. Generally, the scour depth and dune height increased with increasing values of angle of repose.

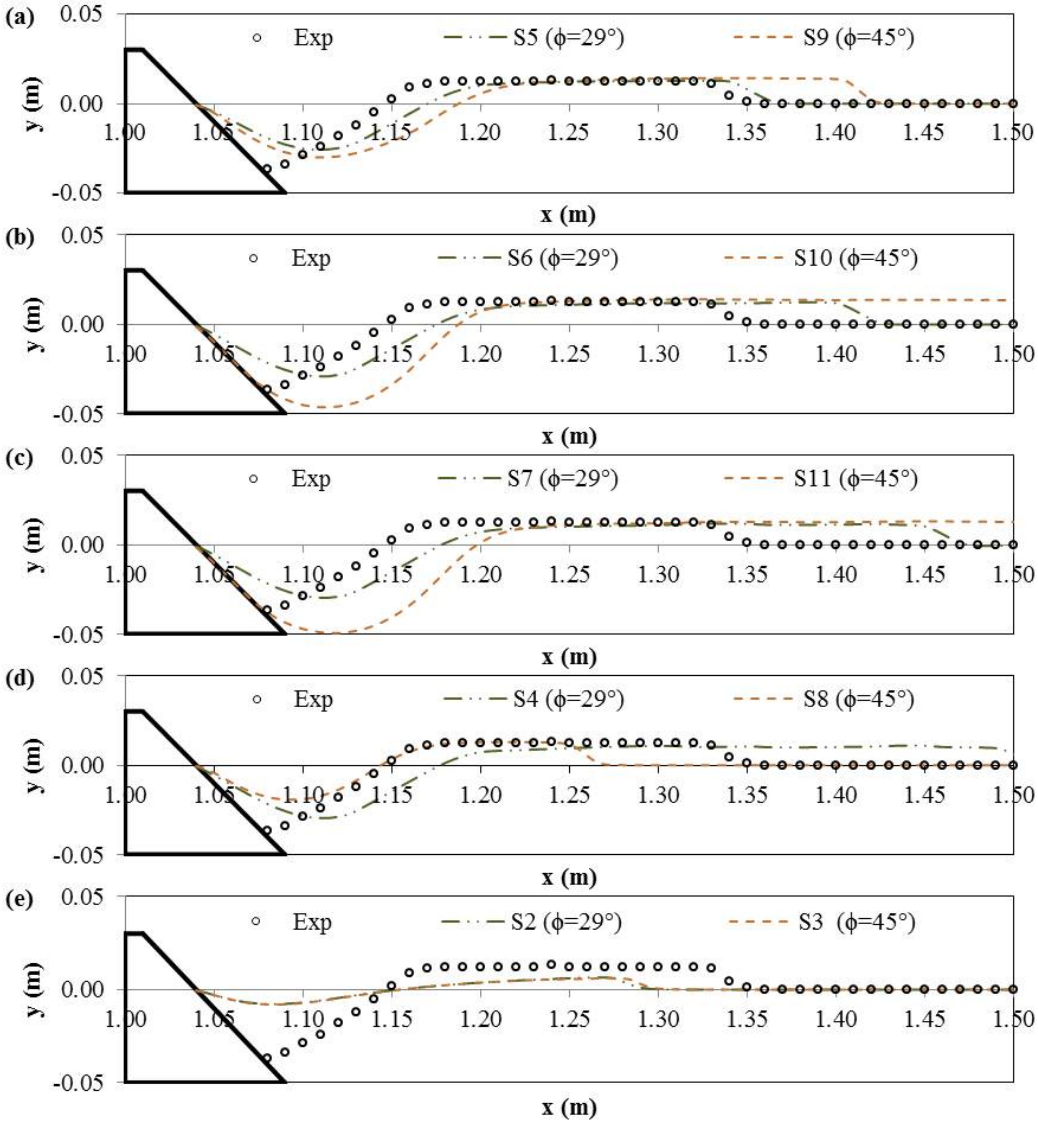

Figure 5.7 Comparison of bed profiles at t = 600 s obtained with different values of angle of repose: (a) RNG k-ε, $k_s = d_{50}$; (b) RNG k-ε, $k_s = 1.5d_{50}$; (c) RNG k-ε, $k_s = 2d_{50}$; (d) RNG k-ε, $k_s = 2.5 d_{50}$; (e) k-ω SST, $k_s = 2.5d_{50}$

5.4.3 Performance of various models

An important benefit of implementing a model in OpenFOAM is that the model can be readily modifiable and extendible. The final simulation in this study used the RNG k-ε model for turbulence closure, but there are many more turbulence models available in the package. Figure 5.8 shows the bed profiles at t = 600 s predicted using different turbulence models. Generally, the shear stresses predicted by the RNG k-ε model were greater than those provided by the standard k-ε and k-ω models, and thus the bed evolutions predicted by the RNG k- ε model were more significant.

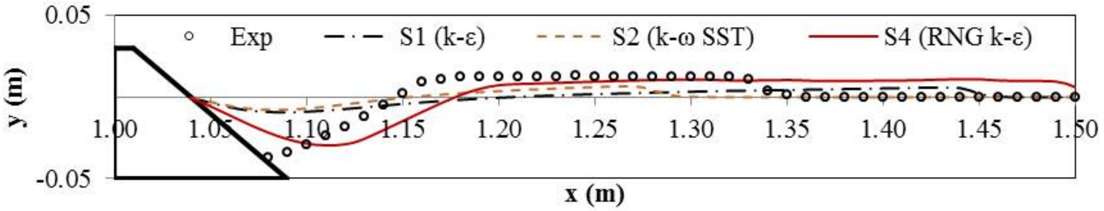

Figure 5.8 Comparison of bed profiles at t = 600 s obtained by different turbulence models

The final simulation in the present study did not use a stochastic model because it may introduce unacceptable uncertainties. However, a stochastic model has also been added into the model and simulations have been conducted to investigate its influence. In the newly implemented model, the bed shear stress was multiplied by a correction coefficient (S_r). The correction coefficient was generated as a random number with a mean value of 1. In simulation S11, the range for the random number generation was [0.5, 15], and that in simulation S13 was [0, 2]. The results are presented in Figure 5.9, showing that the stochastic model can significantly affect the results. The results without a stochastic model can be regarded as a special case of stochastic modeling with a mean value of 1 and range of [1, 1] for the random number generation. As can be seen, a larger range for random number generation generally increased the magnitude of bed erosion and deposition.

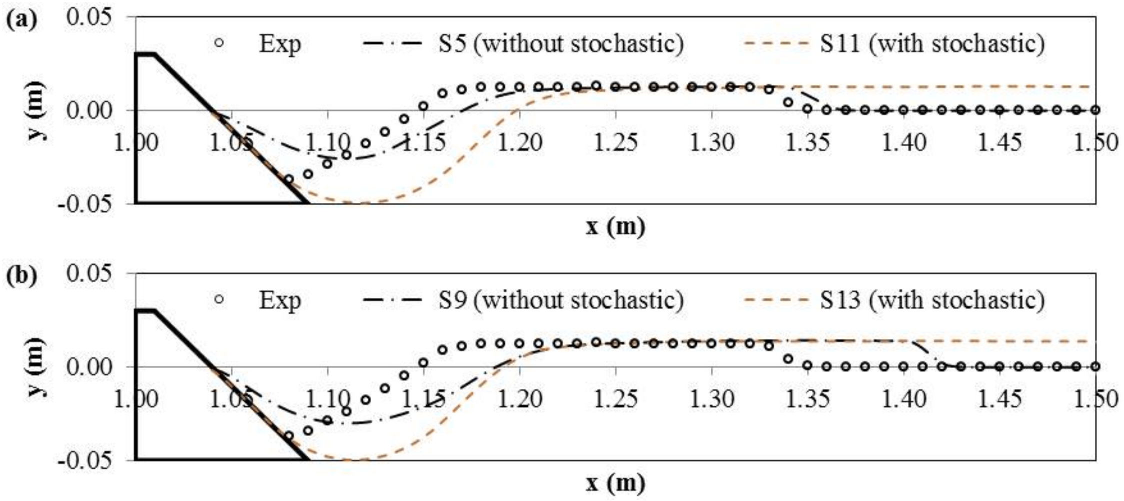

Figure 5.9 Comparison of bed profiles at t = 600 s obtained by different stochastic models: (a) $\phi = 29°$, $S_r = [0.5, 1.5]$; (b) $\phi = 45°$, $S_r = [0, 2]$

It has been explained previously in the present paper that the sands were washed out by the initial flow surge instead of being eroded by the shear stress when the sand layer between the sediment surface and weir surface was thin. Therefore, in the final simulation, the critical Shields number was corrected when the layer thickness was below a certain threshold. The threshold of the layer thickness can be denoted as Δd_c. If the distance between the sediment surface and the weir surface is shorter than this threshold value, the critical Shields number was multiplied by a corrector γ. The bed profiles at t = 600 s obtained by simulations with corrections of critical Shields number are presented in Figure 5.10.

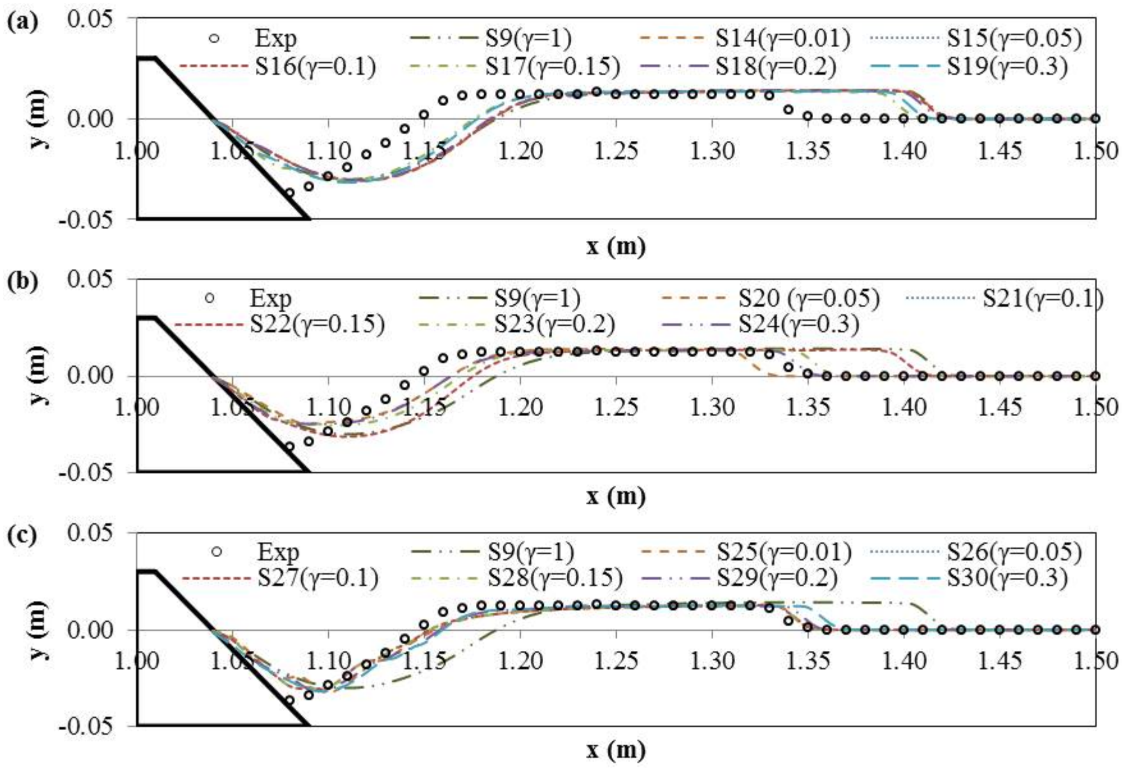

Figure 5.10 Comparison of bed profiles at t = 600 s obtained by simulations with corrections of critical Shields number: (a) Δd_c = 0.01 m, (b) Δd_c = 0.02 m, (c) Δd_c = 0.03 m.

The simulation S9 can be regarded as a special case with a corrector of 1. As can be seen in the figure, the influence of the value of γ was not very significant but the value of Δd_c had a stronger effect on the bed profile. Generally, in a simulation with a greater value of Δd_c, the erosion near the weir was deeper and the downstream dune shifted towards the upstream direction.

Another possible approach of modeling the rapid erosion close to the weir is to add and use a second sand-slide model for a certain region, in which the sand slide phenomenon was forced to occur no matter how small the bed shear stress was. The final simulation in this study did not use this model because it may introduce more uncertainties (e.g., it introduces a new parameter, L_s, which is expected to vary with cases), but this model has been added to the package to see how it affects the results. In simulation S31, the correction region for the second sand-slide model (L) was set at 0.035 m; namely, the second sand-slide model was applied for the region between x = 1.04 m and x = 1.075 m. The bed profiles at t = 600 s obtained by simulations with and without a second sand-slide model are compared in Figure 5.11. As can be seen, the erosion depth in the region of correction was deeper in a simulation with a second sand-slide model.

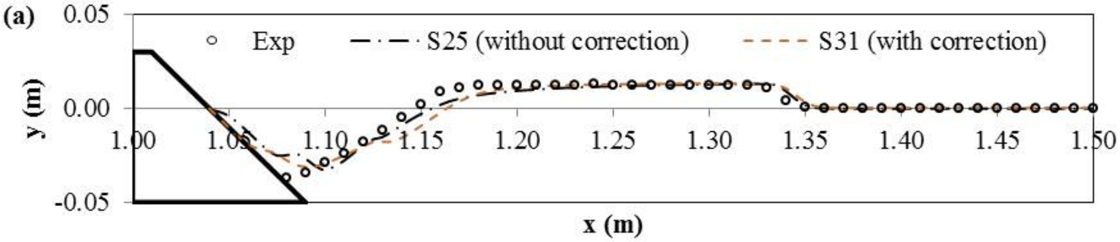

Figure 5.11 Comparison of bed profiles at t = 600 s obtained by simulations with and without a second sand-slide model

5.5 Summary and conclusions

The present study simulated the local scour at a submerged weir with a downstream slope using a coupled moving-mesh and masked-element approach. An experiment was conducted, and the results obtained from the experiment and simulations were compared. The comparisons demonstrated that the present model can satisfactorily reproduce the bed profiles downstream of a sloped submerged weir. The present study aimed to evaluate the performance of the existing model in predicting the local scour downstream of a submerged weir, finding that the predictions close to the weir were less accurate. It has also been found that the numerical results of bed profiles are sensitive to the turbulence models, the stochastic models, the corrections for the critical Shields number, and the sand-slide scheme. Therefore, subsequent studies should be aimed at improving the model in terms of capturing the bed profiles near the weir using different combinations of these configurations. Furthermore, this study focuses on bedload transport modeling, and subsequent studies should also investigate suspended load transport modeling.

5.A1 Appendix: The Shields number and wall function

The Shields number θ_i is defined by

$$\theta_i = \frac{\tau_{bi}}{gd\left(\rho_s - \rho_w\right)} \tag{5A1}$$

where τ_{bi} is the bed shear stress, which is theoretically defined as

$$\tau_{bi} = \rho \nu \frac{\partial U_i}{\partial y}|_{wall} \tag{5A2}$$

where $\left(\partial U_i / \partial y\right)|_{wall}$ is the velocity gradient near the wall. In the current model, τ_{bi} is calculated by

$$\tau_{bi} = \rho \nu_{eff} \frac{U_{1i} - U_{wi}}{y_1} \tag{5A3}$$

where ν_{eff} is the effective viscosity; U_{1i} is the velocity of the flow parallel to the bed at the first cell center; y_1 is the perpendicular distance of the first cell center to the wall; U_{wi} is the velocity of the flow on the wall, which can be assumed to be zero. Note that the velocity gradient near the wall $\left(\partial U_i / \partial y\right)|_{wall}$ is not necessarily equal to $\left(U_{1i} - U_{wi}\right)/y_1$, so an effective viscosity ν_{eff} is taken to make the current expression for bed shear stress equivalent with the standard one.

The effective viscosity is given by

$$\nu_{eff} = \nu + \nu_t \tag{5A4}$$

where ν_t is the turbulence viscosity, calculated by a standard rough wall function in OpenFOAM,

$$\nu_t = \nu \left[\frac{\kappa y^+}{\ln\left(E_r y^+\right)} - 1 \right] \tag{5A5}$$

where κ is the von Karman constant with a default value of 0.41; y^+ is the non–dimensional distance to the wall; E_r is the roughness coefficient.

The non–dimensional distance to the wall y^+ is expressed as

$$y^+ = \frac{u_\tau y_1}{\nu} \tag{5A6}$$

here u_τ is the friction velocity, the initial value of which is estimated by the turbulence model constant c_μ and the turbulent kinetic energy of the cell center adjacent to the wall k,

$$u_\tau = c_\mu^{1/4} \sqrt{k} \tag{5A7}$$

The roughness coefficient E_r is estimated by

$$E_r = \begin{cases} 9.8 & \text{if } k_s^+ \le 2.25 \\ \dfrac{9.8}{\left(\dfrac{k_s^+ - 2.25}{87.75} + C_s k_s^+\right)^{\sin\left(0.4258 \ln k_s^+ - 0.811\right)}} & \text{if } 2.25 < k_s^+ < 90 \\ \dfrac{E}{1 + C_s k_s^+} & \text{if } k_s^+ \ge 90 \end{cases} \tag{5A8}$$

where C_s is the roughness constant with a default value of 0.5; k_s^+ is the dimensionless sand–grain roughness height defined as

$$k_s^+ = \frac{u_\tau k_s}{\nu} \tag{5A9}$$

where k_s is the sand–grain roughness height.

5.A2 Appendix: The sand-slide model

As described in Figure 5A1, P_i and P_{i+1} indicate two adjacent points on a sediment bed; they form a bed slope that is steeper than the critical slope corresponding to the angle of repose of the sands, so the sand particles move downward until a new bed slope is formed.

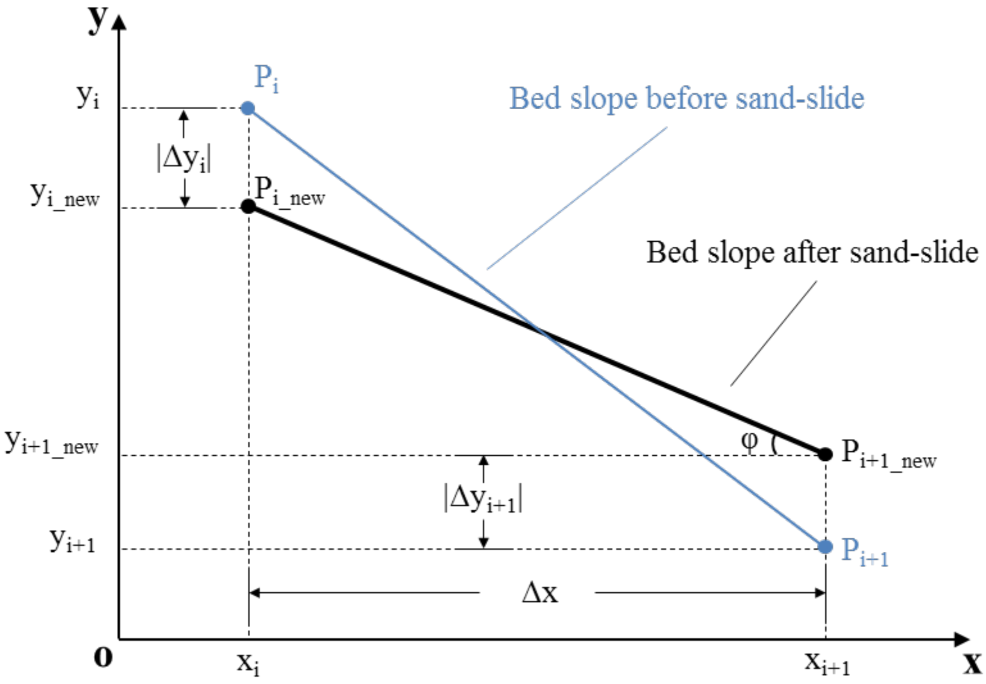

Figure 5A1 Definition sketch of the sand-slide algorithm

The new bed slope is defined by the elevation gradient between the new points, P_{i_new} and P_{i+1_new}, and the angle of the new bed relative to the horizontal plane is equal to the angle of repose. This is achieved using the following equation (Khosronejad et al. 2011):

$$\frac{(y_i + \Delta y_i) - (y_{i+1} + \Delta y_{i+1})}{\Delta x} = \tan \varphi \tag{5A10}$$

where y_i and y_{i+1} are the bed elevations at points P_i and P_{i+1}, respectively; Δy_i and Δy_{i+1} are the corresponding changes in bed elevation due to sand–slide events; Δx is the horizontal distance between the two adjacent points; and φ is the sediment material angle of repose. An additional condition is necessary to be satisfied in order to guarantee mass conservation; for a 2D case on structured mesh, the constraint can be simply expressed as

$$\Delta y_i = -\Delta y_{i+1} \tag{5A12}$$

The new elevations of the two points, $y_{i,new}$ and $y_{i+1,new}$, can then be determined by

$$y_{i,new} = y_i + \Delta y_i \tag{5A13}$$

$$y_{i+1,new} = y_{i+1} + \Delta y_{i+1} \tag{5A14}$$

The sand–slide algorithm is implemented in the following manner. First, the bed slope at each node of the sediment bed boundary patch is calculated; second, the steepest slope is determined and compared to the angle of repose; third, the calculations of bed elevation changes are executed if the steepest bed slope exceeds the angle of repose; finally, the bed nodes are updated. As reported by Khosronejad et al. (2011), a single iteration may not be able to correct all excess slopes, so the above procedures are repeated until the steepest bed slope is equal to or smaller than the angle of repose. In the present study, a converging criterion of 1×10^{-6} m is adopted; when the maximum absolute bed elevation change is smaller than 1×10^{-6} m, the steepest bed slope is regarded equal to the angle of repose, and then the iterative process is terminated.

5.A3 Appendix: The terms in the RNG k-ε model

$$D_{keff} = \frac{\nu_t}{\sigma_k} + \nu \tag{5A15}$$

$$D_{\varepsilon eff} = \frac{\nu_t}{\sigma_\varepsilon} + \nu \tag{5A16}$$

$$\nu_t = c_\mu \frac{k^2}{\varepsilon} \tag{5A17}$$

$$G = \nu_t S_2 \tag{5A18}$$

$$S_2 = 2S_{ij}S_{ij} \tag{5A19}$$

$$S_{ij} = \frac{1}{2}\left(\frac{\partial u_j}{\partial x_i} + \frac{\partial u_i}{\partial x_j}\right) \tag{5A20}$$

$$R_\varepsilon = \frac{\eta\left(1-\eta/\eta_0\right)}{1+\beta\eta^3} \tag{5A21}$$

$$\eta = \sqrt{S_2}\,\frac{k}{\varepsilon} \tag{5A22}$$

where v_t is the turbulent kinematic viscosity; v is the kinematic viscosity; S_{ij} is the strain-rate tensor.

Chapter 6 Additional results and discussions

This chapter provides additional results and discussions that were not included in papers 1 and 2 (Chapters 3 and 4), including some applications of the newly implemented wall jet scour model, numerical modeling of flow around a pipeline near a scoured bed, and mesh configurations and improvement.

6.1 Applications of the wall jet scour model

The effects of some parameters on the equilibrium local scour depths have been studied substantially (e.g., Altinbilek and Basmaki 1973; Chatterjee et al. 1994; Hoffmans 1998; Dey and Sarkar 2006; Melville and Lim 2013; Shayan et al. 2015), but there is a lack of studies in the literature on the effects of some physical factors on early stages of the transient scouring process, primarily because the flow and streambed evolutions in the early stages are quite difficult to capture using experimental methods due to the rapid flow variations. However, the understanding of transient scouring processes in the early stages is quite important for some practical engineering applications, such as short-term storm surges and flooding events. As stated previously, transient numerical modeling approaches can be used to capture these details.

In this section, the effects of a few parameters on the erosive power of the submerged wall jet during the early stages are investigated numerically using the proposed and validated numerical model. These parameters are chosen primarily because they have significant engineering and practical interest. Models based on the previous techniques (e.g., the "artificial geometric discontinuity" method and available automatic mesh motion techniques) have been developed and tested, but they all had the problem of mesh failure without substantial artificial modification of the geometry, which hinders the application of the models. The present model uses a better moving-mesh technique, and thus is able to avoid the above problems and can be applied to investigate different cases regarding local scour problems. Moreover, many previous studies attempted to derive empirical equations that can be generally used to describe the properties of the scouring due to submerged wall jets, but the results were very scattered (Altinbilek and Basmaki 1973; Chatterjee et al. 1994; Hoffmans 1998; Dey and Sarkar 2006; Melville and Lim 2013; Shayan et al. 2015), partially because the local scour properties depend on too many parameters (e.g., the gate opening, apron length, tailgate height, streambed slope, discharge, sediment size and gradation, and jet inclination) and the results are very sensitive to the experiment conditions. Therefore, a practical and reliable method is to employ a numerical model to simulate a base case for a certain project, and then investigate the effects of different alternatives using the same model. The present model can be used for these purposes and this section can be regarded as a demonstration. All the experiments examined in the numerical model presented in this section use the present experiment as a base case. In all the simulations considered in this study, a large portion of the erosion takes place in the first minute; thus, a time span of 60 s is regarded as the criterion for the early stage. Some simple regression formulas are also proposed based on the simulated results using the nonlinear least-square method.

6.1.1 Effects of the gate opening

One application of the current numerical model is to simulate the effects of the gate opening. A clear understanding of how varying the gate opening affects the erosive power of the submerged wall jet is necessary for proper operation of the sluice gate. The investigated gate openings ranged from 0.01 m to 0.05 m with an interval of 0.01 m. The discharge under the sluice gate can be either constant or variable. The constant scenario was considered here. The time history of maximum scour depths under different gate opening scenarios is shown in Figure 6.1.

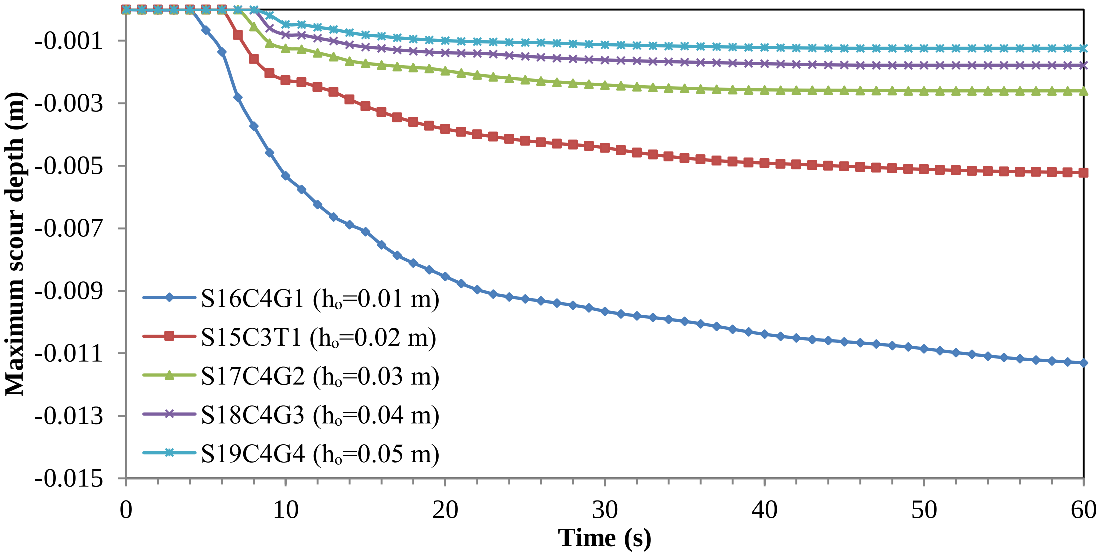

Figure 6.1 Time series of maximum scour depths under different gate opening scenarios

As shown in Figure 6.1, the time variations of the maximum scour depths for the different cases showed a similar pattern. The speed of sediment erosion was rapid during the early stages, and then gradually decreased. Thus, the time variations of the maximum scour depths can be expressed in the following form:

$$d_{\max} = -A \ln t + B \tag{6.1}$$

where d_{max} is the maximum scour depth, t is time, A and B are regression coefficients, the values of which are listed in Table 6.1. The R^2 values and the average variation rate of the maximum scour depth, R_{avg}, are also summarized in the same table. It can be concluded from Figure 6.1 and Table 6.1 that the erosion depth tends to decrease with an increasing gate opening. Under constant discharge, the increase in the gate opening led to a decrease in the velocity and strength of the jet flow, which in turn caused the decrease in the bed shear stress, resulting in a decrease of scour depth. The strength of the jet flow can be represented by the jet Froude number; thus, the results showed that the erosive power of the jet flow increased with the jet Froude number, which was consistent with previous experimental observations (Tarapore 1956; Rajaratnam 1981; Rajaratnam and MacDougal 1983; Lee 1995; Lim and Yu 2002; Melville and Lim 2013).

Table 6.1 Statistics of the maximum scour depths under different gate opening scenarios

Simulation	h_o **(m)**	A	B	R^2	R_{avg} **(m/s)**
S16C4G1	0.01	4E-3	0.0029	0.95	-2E-4
S15C3T1	0.02	2E-3	0.0019	0.96	-6E-5
S17C4G2	0.03	8E-4	0.0006	0.91	-3E-5
S18C4G3	0.04	6E-4	0.0006	0.87	-2E-5
S19C4G4	0.05	4E-4	0.0004	0.87	-1E-5

The regression formula describing the time variations in the transient maximum scour depth can be further modified to consider the gate opening effects, expressed in the following form:

$$d_{\max} = -\frac{A}{h_0 - C} \ln t + B h_0 \tag{6.2}$$

where A, B, and C were found to be 2.61×10^{-5}, 0.01809, and 0.0006353, respectively, from the nonlinear least-square method. The R^2 value for the regression was 0.97, and the RMSE was 0.0005 m.

6.1.2 Effects of the apron length

Another application of the current numerical model is to simulate the effects of the apron length. A clear understanding of how varying the apron length affects the erosive power of the submerged wall jet is important for the sound and efficient design of the apron length. The investigated apron lengths ranged from 0.2 m to 0.8 m with an interval of 0.2 m, in addition to the base case (0.66 m). The time history of maximum scour depths under different scenarios of apron length is shown in Figure 6.2.

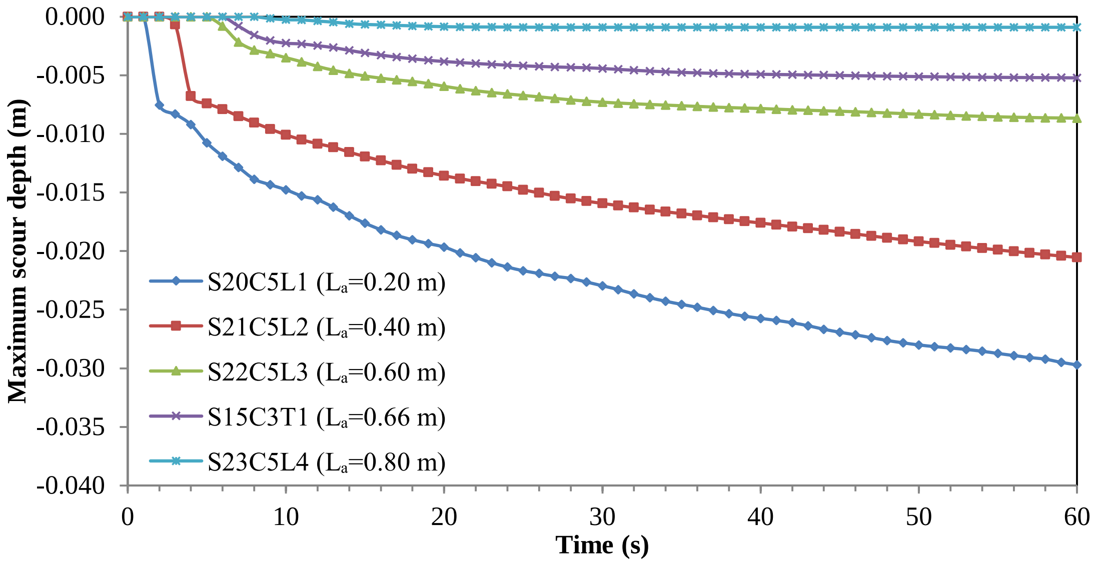

Figure 6.2 Time series of maximum scour depths under different scenarios of apron length

As shown in Figure 6.2, the time variations of the transient maximum scour depths for the different cases can also be expressed in the form of the same equation, and the statistics are listed in Table 6.2.

Table 6.2 Statistics of the maximum scour depths under different scenarios of apron length

Simulation	L_a (m)	A	B	R^2	R_{avg} (m/s)
S20C5L1	0.20	-0.007	0.0013	0.98	-4E-4
S21C5L2	0.40	-0.006	0.0030	0.98	-3E-4
S22C5L3	0.60	-0.003	0.0033	0.98	-1E-4
S15C3T1	0.66	-0.002	0.0019	0.96	-6E-5
S23C5L4	0.80	-3E-4	0.0002	0.66	-2E-5

It can be concluded from Figure 6.2 and Table 6.2 that the erosion depth tended to decrease with an increasing apron length. When the jet was issued from the sluice gate to the ambient water downstream of the sluice gate, a shear layer was formed, which entrained the ambient fluid into the jet, and the momentum dissipated and transferred from the jet to the ambient fluid. Therefore, the strength of the jet flow decreased along the streamwise direction, and thus the bed shear stress where the jet interacted with the streambed was much smaller if a longer protection apron was utilized, resulting in a decrease in scour depth. This was consistent with previous experimental observations (Lim and Yu 2002; Dey and Sarkar 2006; Melville and Lim 2013). The regression formula describing the time variations in the transient maximum scour depth can be further modified to consider the apron length effects, expressed in a form similar to that for the gate opening effects, as follows:

$$d_{\max} = -\frac{A}{L_a + C}\ln t + BL_a \tag{6.3}$$

where A, B, and C were found to be 0.00419, 0.0141, and 0.3266, respectively, from the nonlinear least-square method. The R^2 value for the regression was 0.96, and *RMSE* was 0.0016 m.

5.1.3 Effects of the tailgate height

The downstream flow control condition is another major factor influencing the scouring processes, and it can be represented by the tailgate height. Investigating the tailgate height effects on the erosive power of the submerged wall jet is crucial in the proper operation of the sluice gate, design of protection measures, and sound control of the downstream water-training structures. The investigated apron lengths range from 0.03 m to 0.14 m, in addition to the base case (0.125 m).

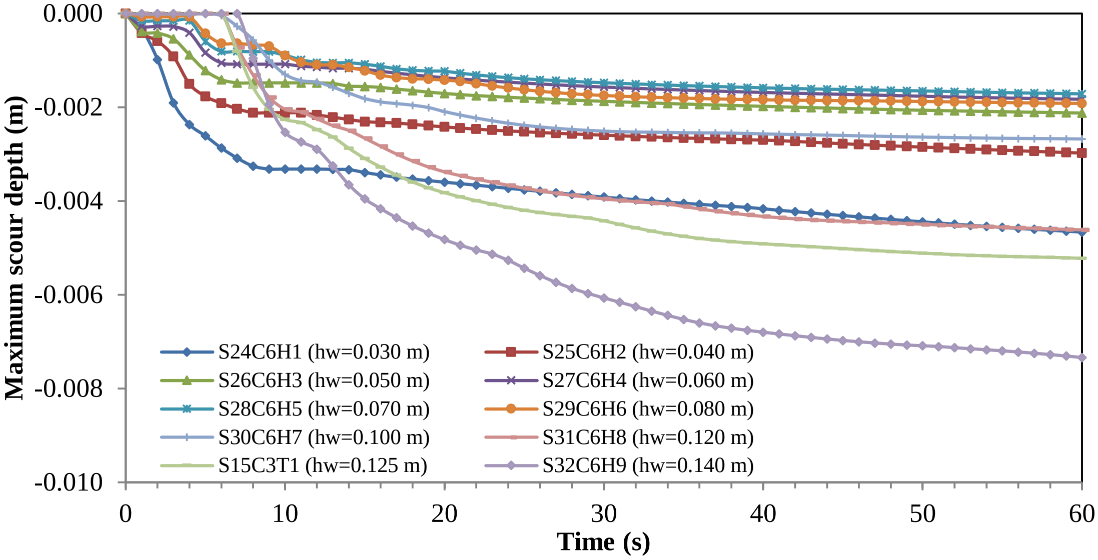

Figure 6.3 Time series of maximum scour depths under different scenarios of tailgate height

The time history of maximum scour depths under different scenarios of tailgate height is shown in Figure 6.3, and the statistics for the regression equation are listed in Table 6.3. Figure 6.3 and Table 6.3 show that the erosion depth tended to first decrease and then increase with an increasing tailgate height. Previous experimental works for similar problems also reported that there is a critical tailwater depth corresponding to a minimum local scour depth (Ali and Lim 1986; Melville and Lim 2013; Xie and Lim2014; Shayan et al. 2015). As discussed by Ali and Lim (1986), this sagging nature is probably due to the different types of flow patterns and characteristics of the free or drowned hydraulic jump, which results in different velocity distributions near the bed. In the present case, the critical tailgate height was about 0.07 m.

Table 6.3 Statistics of the maximum scour depths under different scenarios of tailgate height

Simulation	h_w (m)	A	B	R^2	R_{avg} (m)
S24C6H1	0.030	9E-4	-0.0009	0.96	-4E-5
S25C6H2	0.040	6E-4	-0.0007	0.95	-2E-5
S26C6H3	0.050	4E-4	-0.0004	0.96	-2E-5
S27C6H4	0.060	4E-4	8E-5	0.97	-2E-5
S28C6H5	0.070	5E-4	0.0001	0.97	-2E-5
S29C6H6	0.080	6E-4	0.0004	0.95	-3E-5
S30C6H7	0.100	9E-4	0.0008	0.91	-4E-5
S31C6H8	0.120	2E-3	0.0016	0.96	-5E-5
S15C3T1	0.125	2E-3	0.0019	0.96	-6E-5
S32C6H9	0.140	3E-3	0.0033	0.97	-9E-5

The regression formula describing the time variations in the transient maximum scour depth can be further modified to consider the tailgate effects, expressed in a the following form:

$$d_{\max} = \begin{cases} \left(A_1 - \dfrac{C_1}{h_w}\right)\ln t - B_1 h_w & h_w \le h_{wc} \\ \left(A_2 - C_2 h_w\right)\ln t - B_2 h_w & h_w > h_{wc} \end{cases} \qquad (6.4)$$

where h_{wc} is the critical tailgate height (0.07 m for the present case), and A_1, B_1, and C_1 were found to be 0.0004062, 0.006964, and 4.467×10^{-5}, respectively, while A_2, B_2, and C_2

were found to be 0.001303, -0.01249, and 0.02454, respectively. The R^2 and *RMSE* values for the case where the tailgate height was lower than or equal to the critical depth were 0.96 and 0.0002 m, respectively. The values for the case where the tailgate height was higher than the critical depth were 0.95 and 0.0004 m, respectively.

6.2 Flow around a pipeline near a scoured bed

Jensen et al. (1990) performed point velocity measurements for a number of cross sections around a pipeline above five different scoured bed profiles in a steady current. Their work presented a comprehensive data set for fixed-bed flow and was thus used to validate the hydrodynamic module proposed here. The experiments were conducted in a 10m×0.3m×0.3m water flume. The outer diameter of the pipeline was 0.03 m. The flow depth was kept constant at 0.23 m. The Reynolds number based on the pipe diameter was 6000. The sampling rate for the velocity measurements was 40 Hz, and the sample size was 40,000.

The model setup was mainly determined according to the experimental conditions. The computational domain was 2.4 m in length and 0.23 m in height. Additional simulations were performed with larger computational domains, and the results in the area of interest were found to be almost identical to the final results. The mesh resolution was determined with an independency tolerance of 2%. A uniform velocity of 0.2 m/s was imposed at the upstream inlet section. A rigid-lid assumption was employed to approximate the free surface, as Smith and Foster (2005) found that there were no appreciable differences when a free-surface boundary condition was utilized. A zero-gradient boundary condition was assigned to the downstream outflow boundary. The no-slip boundary condition was assigned to the sand bed patch and the standard rough wall function in OpenFOAM was applied. The so-called “empty” boundary condition available in OpenFOAM was used for the front and back patches, so the simulations were reduced to two-dimensional. The simulations were run for up to 1000 s, which was consistent with the sampling rate and sample size in the experiment. A value of 0.001 s was used as the default time step interval, but the actual time step was automatically adjusted based on the numerical stability criterion.

Jensen et al. (1990) reported the time-averaged streamwise and vertical velocities at various locations in the experimental setup. Here, data were digitized from the plots presented by Jensen et al. (1990) and are presented in Figure 6.4, which also contains the time-averaged velocities calculated from the present numerical results.

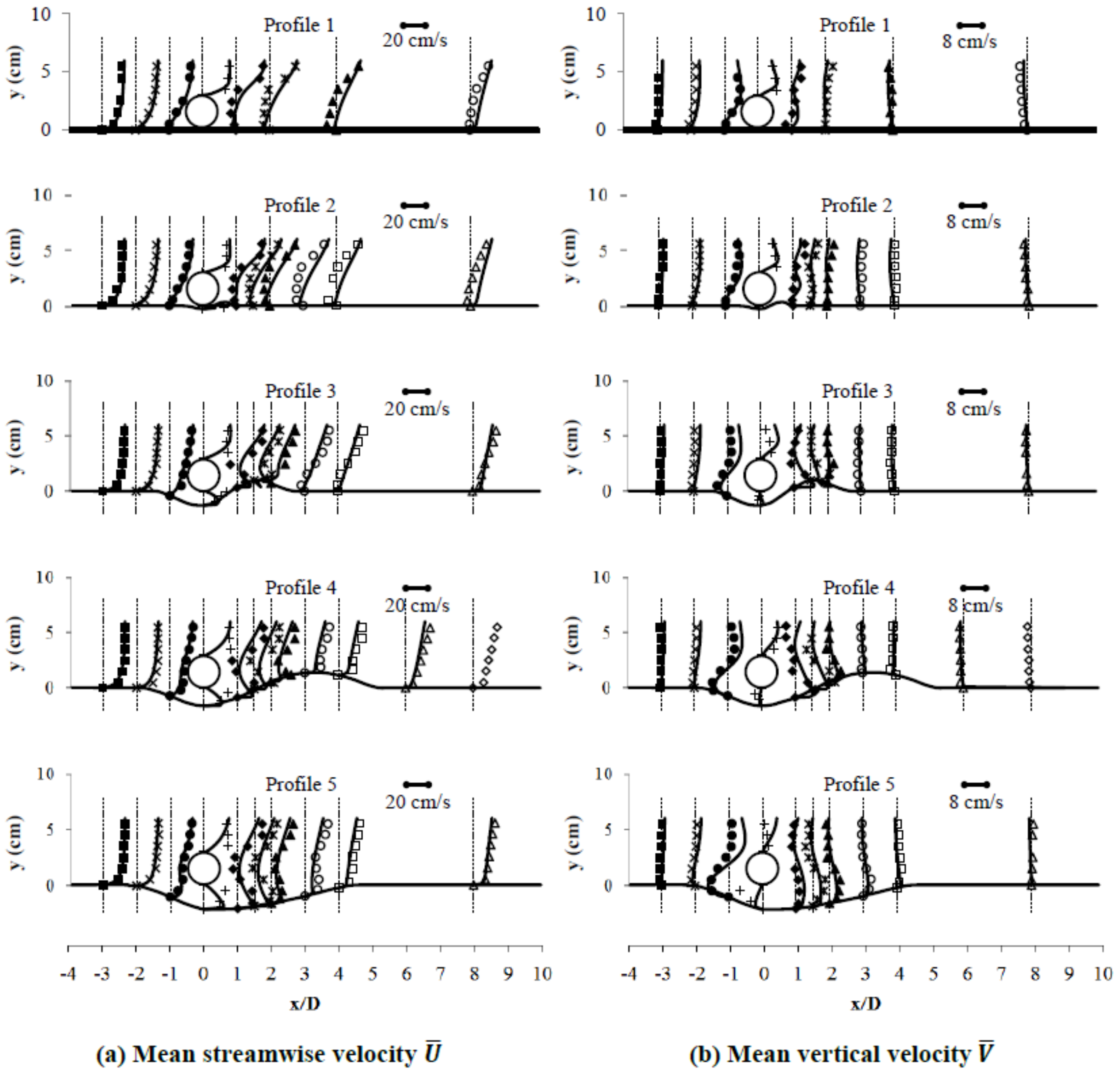

(a) Mean streamwise velocity $\overline{U}$ (b) Mean vertical velocity $\overline{V}$

Figure 6.4 Comparison of the measured (symbols) and simulated (solid lines) mean velocities in five different cases

To obtain a quantitative measure of the difference between the data and predictions, the root-mean-squared errors (RMSE) and R-squared (R^2) correlation values (Legates et al. 1999; Shcherbakov et al. 2013) at all the considered cross sections were calculated and are presented in Figures 6.5 and 6.6. The RMSE and R^2 values can be used to evaluate the magnitudes of the simulated velocity and the shapes of the simulated velocity profiles, respectively. Smith and Foster (2005) simulated the same experiments using a commercial CFD software, FLOW-3D, with a k-ε and a Smagorinsky LES turbulence closure. In their simulations, the fractional area-volume obstacle representation (FAVOR) technique was employed to simulate the fluid-solid interfaces. The RSME and R^2 values between their simulations and the experiment are also presented in Figures 6.5 and 6.6.

As expected, the profiles of streamwise velocity in the upstream region (x/D = -3 and -2) appear to be logarithmic, as the flow was well established and not significantly affected by the pipeline or the scoured bed. The numerical models correctly predicted the overall shape of the velocity profiles, as the R^2 values were very close to 1. The velocity magnitudes provided by the present model showed an excellent match with the experimental data in this region, and the RMSE values were consistently lower than those for the two models used by Smith and Foster (2005), except at X/D = -2 in the case “Profile 4”. The RMSE and R^2 values for the vertical velocity were lower, primarily because the vertical velocity magnitudes were lower.

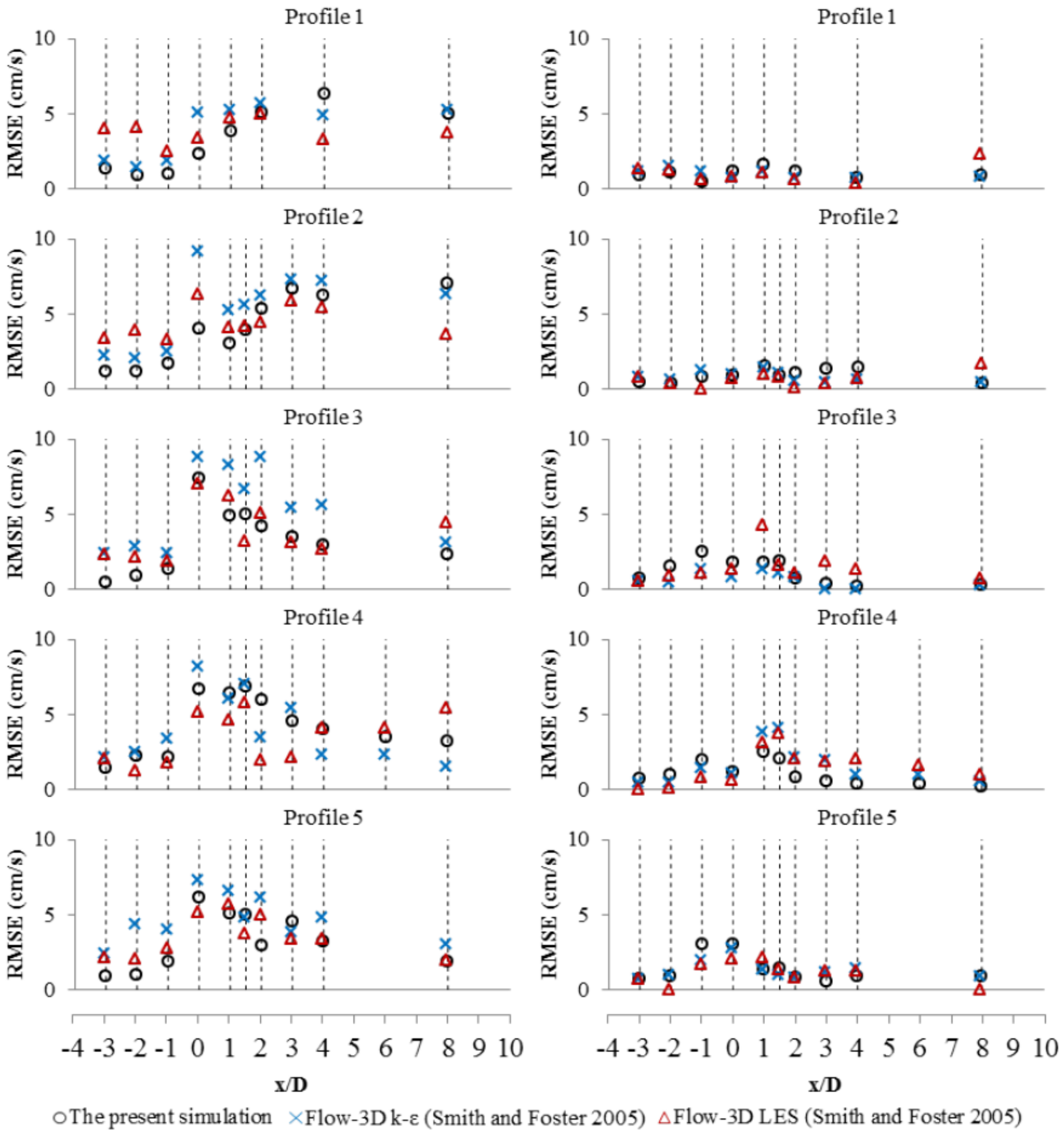

(a) Mean streamwise velocity $\bar{U}$ (b) Mean streamwise velocity $\bar{V}$

Figure 6.5 Comparison of the RMSE values for the different model results

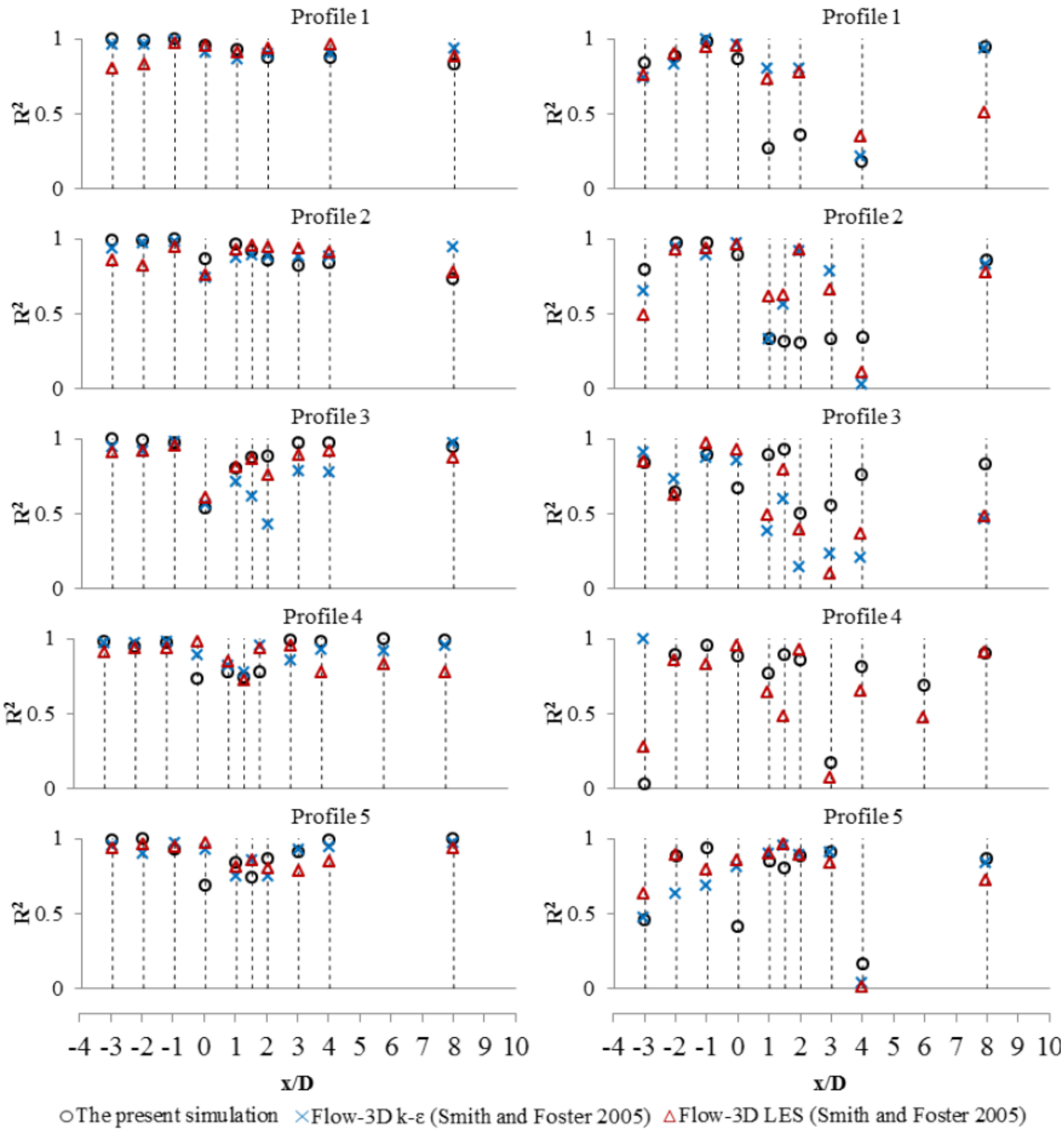

(a) Mean streamwise velocity $\bar{U}$ (b) Mean streamwise velocity $\bar{V}$

Figure 6.6 Comparison of the R^2 values for the different model results

As shown by the measurements, flow deceleration and reversal of the vertical gradient of the velocity occurred downstream of the pipeline, partially due to flow blockage caused by the pipeline. The models described this feature well. The flow characteristics in the downstream region became more complicated than in the upstream region due to the existence of the pipeline, especially in the case “Profile 5”, where the vortex shedding became a dominant feature. Therefore, the numerical calculations in this region were slightly worse than those in the upstream region, as indicated by the error statistics. However, the numerical predictions were still within a reasonable range, and the present model provided the best results among all the models for most of the cases.

The present model performed relatively poorly at the locations immediately above and below the pipeline in the cases “Profile 4” and “Profile 5”. This revealed the incapability of the present method to accurately resolve the flow field very close to the pipeline-water interface. However, the good agreement between the measured and simulated results for surrounding locations demonstrated that low prediction accuracies only occurred immediately adjacent to the pipeline boundary. The shape and magnitude of the velocity profiles near the sediment bed were very well predicted.

6.3 Mesh configurations and improvement

To achieve a successful simulation, it is important to make optimal decisions on the organization and sizes of the computational grids. Structured meshes with local refinements were used in the simulation for the wall jet scour experiment (Chatterjee et al. 1994), as shown in Fig. 6.7.

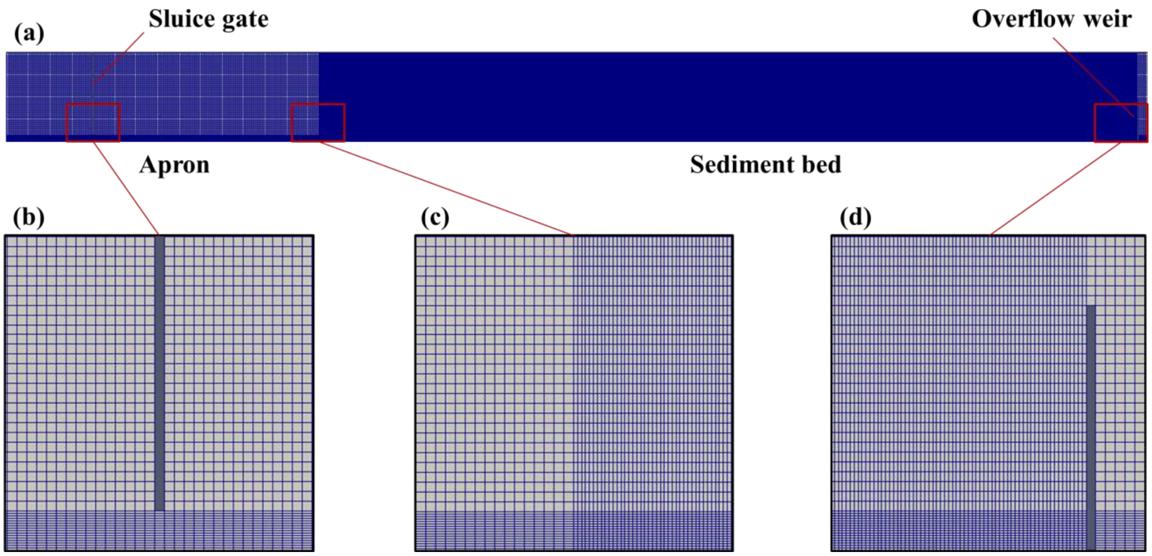

Figure 6.7 A typical mesh setup: (a) the whole computational domain; (b) the detailed grids near the sluice gate; (c) the detailed grids near the transition from apron to sediment bed; (d) the detailed grids near the overflow weir.

The computational domain contained only one cell in the span–wise direction, as the simulation was two–dimensional. Refinement was performed in some regions both in the stream–wise and vertical directions to keep a good balance between accuracy and cost. The focus of the simulations was on the sediment evolution, so the grids over the sediment bed used a higher resolution than those over the apron. The grids in lower layers have more significant influence on the numerical results of streambed erosion, so the grid resolution was higher close to the sediment bed. The region downstream of the overflow weir was out of the primary domain of interest and had almost no impact on the upstream field, so relatively coarser mesh was employed.

A finer mesh typically produces better results but requires larger computational effort. Therefore, a modeler has to make a compromise between accuracy and efficiency.

In the current work, the mesh resolution was determined following the mesh sensitivity analysis procedures used by Yan and Mohammadian (2017). Taking the simulation for the wall jet scour experiment (Chatterjee et al. 1994) as an example, six grid resolutions were evaluated for a grid independency study with a tolerance of 0.001 m, as shown in Fig. 6.8 (a).

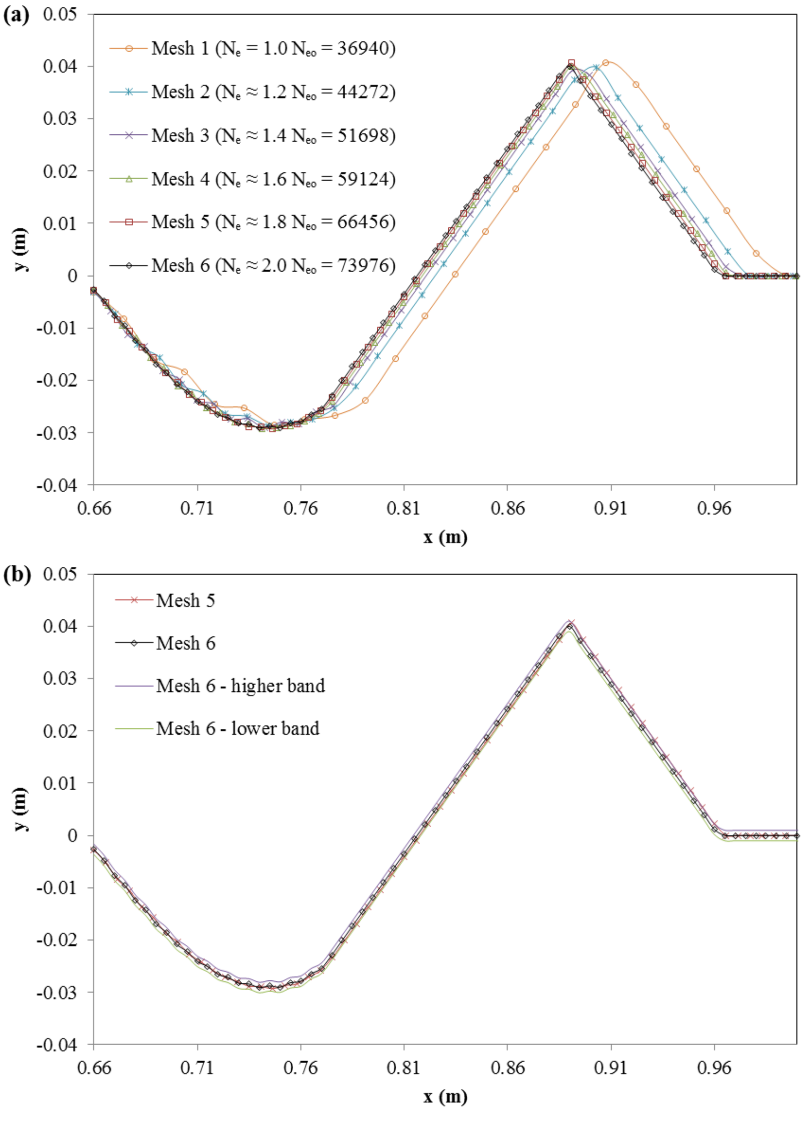

Figure 6.8 Case A sediment bed elevations predicted by simulations with different grid resolutions

A preliminary simulation was conducted with a relatively coarse mesh (Mesh 1), which contained N_{eo} = 36940 cells. Then more simulations with finer meshes were performed, and the numbers of cells of these meshes, N_e, were 1.2~2.0 times N_{eo}. As shown in Figure 6.8 (b), almost all of the points obtained by Mesh 5 resided between the upper and lower bands (± 0.001 m) of Mesh 6, meaning that the model achieved the desired confidence criterion. To be conservative, Mesh 6 was finally adopted.

To further improve mesh quality, a central mesh smoothing scheme for the sediment bed has been added into the modeling system as

$$y_{i,new} = a_s y_i + \left(1 - a_s\right) \frac{y_{i-1} + y_{i+1}}{2} \tag{6.5}$$

where $y_{i,new}$ is the new bed elevation at point P_i; a_s is a smoothing coefficient; y_i is the original node location; and y_{i-1} and y_{i+1} are the positions of the nodes upstream and downstream of point P_i, respectively. The scheme is inactive by default and can be turned on. The smoothing coefficient, time step, and iteration numbers are all user–defined values. The determination of these values requires trial–and–error effort, and proper selection of these values could improve the mesh quality but does not severely change the mesh shape.

Some irregular points were observed on the bed profiles in some preliminary simulations, so the mesh smoothing scheme was employed. A commonly seen problem of dynamic–mesh–based models is that the mesh may exhibit some non–smooth behavior, partially due to interpolation errors (Chen and Holst 2011). For example, the present model interpolates hydrodynamic variables from face centers to grid nodes to calculate bed evolution, which inevitably leads to errors caused by interpolation. For the wall jet scour case corresponding to the experiment conducted by Chatterjee et al. (1994), the magnitude of bed elevation changes was much larger than the errors, so the mesh irregularities were negligible. For the wall jet scour case corresponding to the present experiment, however, the erosion depth and deposition height were relatively small, so the non–smoothness became more obvious, and thus a mesh improvement was necessary.

The mesh improvement approaches can be mainly classified into three categories: refinement, edge–swapping, and mesh–smoothing (Chen and Holst 2011). The refinement method can save a large effort of programming, but it would sacrifice the model efficiency. The edge–swapping method is more appropriate for triangular grids rather than the current type of mesh. Therefore, the mesh–smoothing approach was considered for the purpose of mesh improvement.

There are many mesh smoothing techniques available in some widely recognized CFD or mesh–generation software, such as the Laplacian smoothing and skewness–based smoothing techniques in Fluent (Fluent 2017), and the centroid area pull and edge length methods in CUBIT (Team 2016). In the present simulations, the mesh is structured and quadrilateral, the smoothing scheme is only supposed to be applied to the sediment bed, and the grid resolution is relatively high, so a simple smoothing scheme, represented by Eqn. (6.5), is adequate to achieve the current purpose. The adopted smoothing scheme is similar to a Laplacian one, which determines a node position based on the local information, but it is more advantageous in conserving the original shape of the mesh because the new position of a node largely depends on its original position.

For the wall jet scour case corresponding to the present experiment, the mesh smoothing scheme was turned on. The smoothing coefficient was set to be 0.9. The time step for the smoother was 60 seconds, and the iteration number was 10. Comparing the results before and after the smoother is applied at only one time instance may not be adequate to evaluate the performance of the scheme, so the simulated results at different time sequences are compared (Figure 6.9).

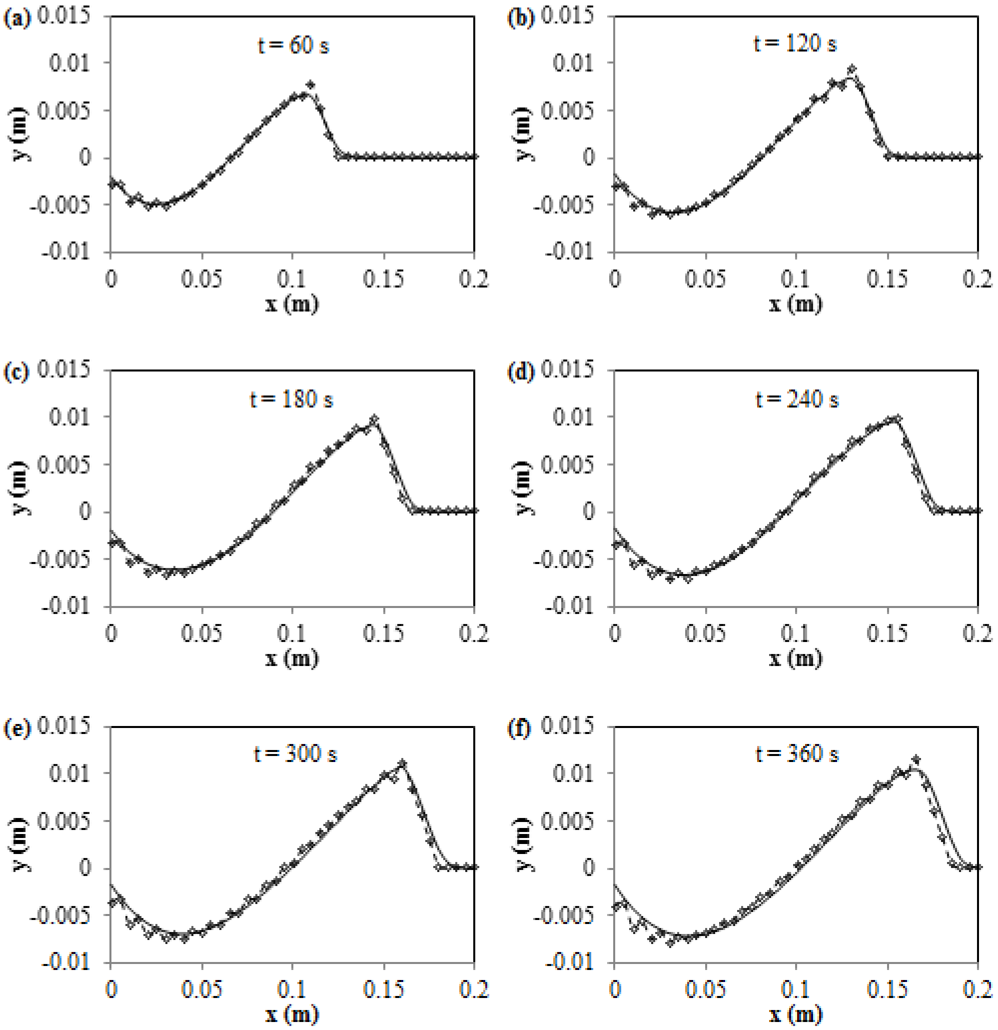

Figure 6.9 Simulated bed profiles for the present case with (solid line) and without the mesh smoothing scheme (dash line with symbols).

As shown in Figure 6.9, the smoothed profile extended slightly more downstream than the raw profile, which may explain some of the disparities between the experimental data and numerical predictions. Overall, the performance of the smoothing algorithm was satisfactory as it successfully removed the noisy nodes or irregularities without obviously affecting the profile shape.

6.4 Additional figures

A photo of the experimental setup for the test of scour caused by a submerged wall jet, corresponding to the schematic diagram (Figure 3.2), is shown in Figure 6.10.

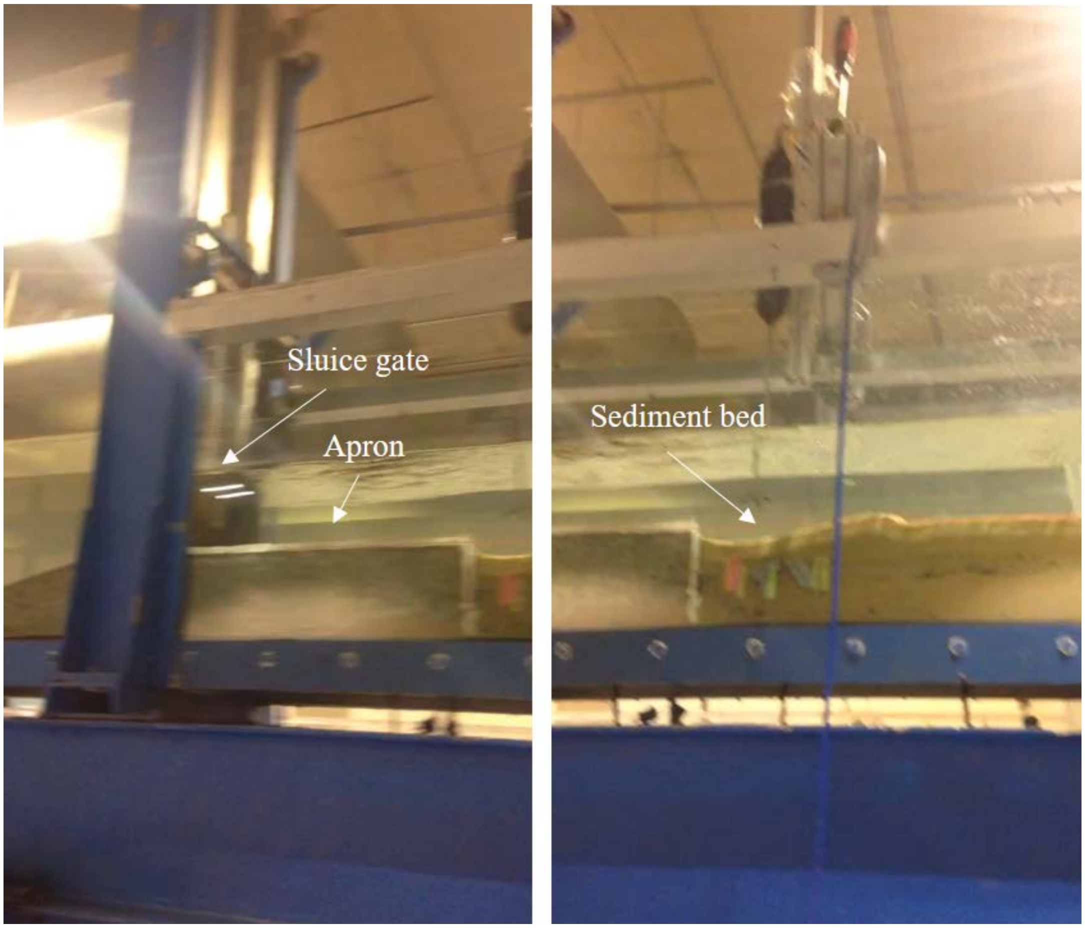

Figure 6.10 A photo of the experimental setup for the test of wall jet scour

A photo of the experimental setup for the test of scour caused by a submerged weir with a downstream slope, corresponding to the schematic diagram (Figure 5.1), is shown in Figure 6.11.

Figure 6.11 A photo of the experimental setup for the test of scour caused by a submerged weir with a downstream slope

The simulated flow fields corresponding to the case presented in Figure 5.3 are visualized in Figure 6.12. The region with vectors indicates the water flow field, and that without vectors indicates the air flow field.

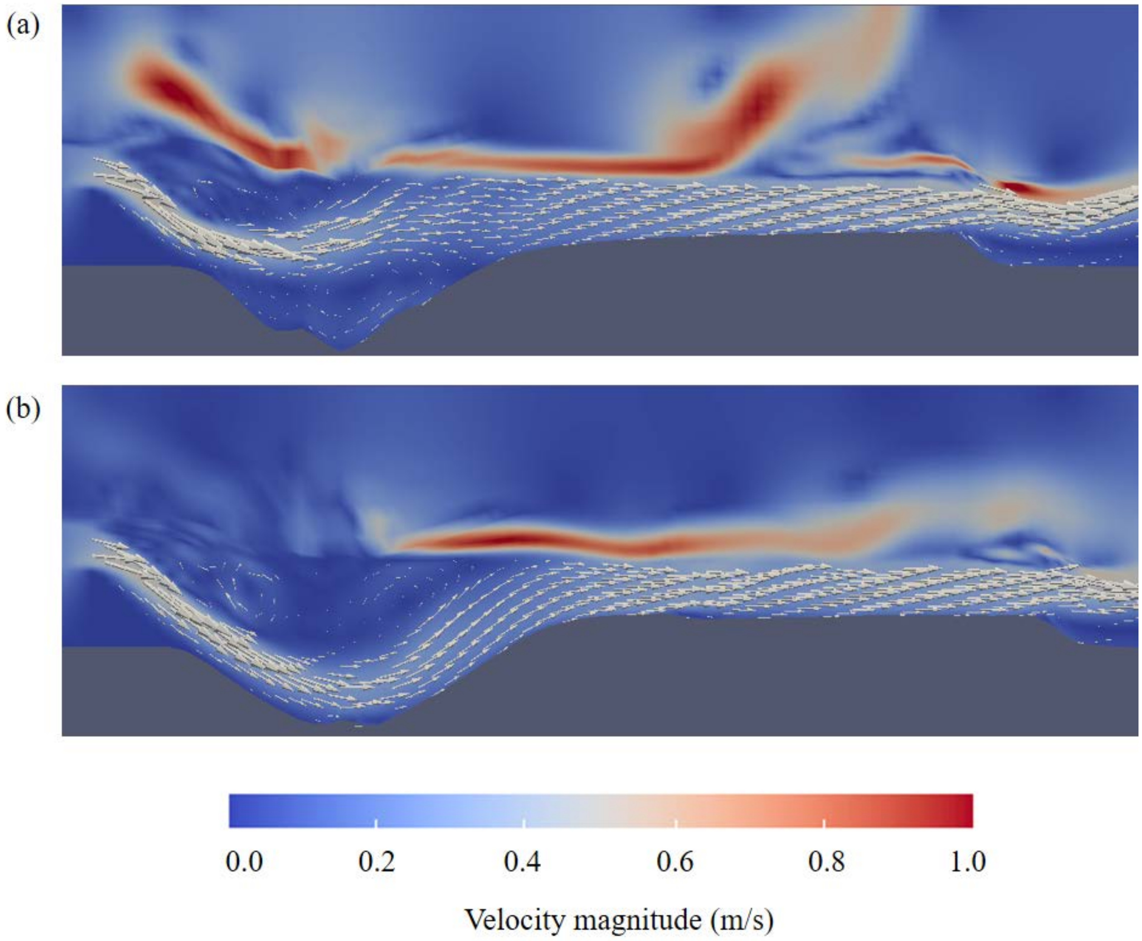

Figure 6.12 The simulated flow fields at different time sequences: (a) t = 600 s; (b) t = 1200 s. The region with vectors indicates the water flow field, and that without vectors indicates the air flow field.

Chapter 7 Summary and conclusions

The present study aimed to develop a novel sediment scour approach and implement a sediment scour model in OpenFOAM. In order to achieve this objective, this study included three parts focused on development and validation of new numerical approaches for sediment scour modeling, and one part for additional results and discussions. The three parts for model development and validation correspond to three commonly seen sediment scour problems, respectively, and they were organized in the current thesis based on their complexities.

In the first part of this study (Chapter 3), a new sediment-scour model with a strict vertex-based terrain conformal moving-mesh technique within the framework of OpenFOAM was implemented. Numerical simulations of local scour due to submerged wall jets were performed using a newly implemented numerical model in OpenFOAM. The present model was used to simulate a prescribed boundary motion case. The models using previous and available moving-mesh schemes were also developed and utilized to simulate the same case. The results demonstrated that the developed present model allows for more severe topographic variations without requiring any artificial modification of the geometry. The simulated results were compared to the experimental and the previously simulated results. The simulated results matched satisfactorily with the measured data, demonstrating the capability of the developed model in predicting local scour due to submerged wall jets. A new laboratory experiment was also conducted in this study and the present model accurately predicted the bed evolutions, confirming that the present model can be used to simulate local scour problems due to submerged wall jets.

In the second part of this study (Chapter 4), a new numerical model for flow and sediment scour phenomena, using moving mesh with masked elements, was implemented. The proposed numerical model was able to predict the overall shape of the logarithmic velocity profiles in the upstream region and the flow deceleration and reversal of the vertical gradient of the velocity that occurred downstream of the pipeline. There were no mesh problems nor any resultant numerical instability encountered in the present simulations for the bed evolution cases, demonstrating that the present model outperformed the typical boundary-fitted-grid methods in sustaining the simplicity and quality of computational mesh. The model predicted both the upstream and downstream parts of the scour hole beneath the pipeline reasonably well. It reproduced the downstream deposition very well, except at the dune crests.

In the third part of this study (Chapter 5), the local scour at a submerged weir with a downstream slope was simulated using a coupled moving-mesh and masked-element approach. An experiment was also conducted, which provides the bed profiles at different time instants. The comparisons demonstrated that the present model can satisfactorily reproduce the bed profiles downstream of a sloped submerged weir. Furthermore, the effects of various parameters and configurations, such as the roughness height estimation, angle of repose, turbulence model, stochastic model, critical Shield number, and a second sand-slide model, on the numerical predictions have also been studied.

In the fourth part of this study (Chapter 6), the present model was further applied to investigate the effects of a few parameters on the transient scouring processes in the early stages. These studies not only made contributions to the knowledge regarding sediment scour problems but also demonstrated how the present model would be useful in engineering practice. The present model was utilized to simulate the flow around a pipeline near a scoured bed. The proposed numerical model was able to predict the overall shape of the logarithmic velocity profiles in the upstream region and the flow deceleration and reversal of the vertical gradient of the velocity that occurred downstream of the pipeline. The proposed model performed relatively poorly at the locations immediately below the pipeline. However, the favourable agreement between the measured and simulated results in the surrounding locations demonstrated that low prediction accuracies only occurred at a few locations immediately adjacent to the pipeline. Its performance can be further improved by releasing the simplifications of the fixed-grid method if needed.

This study limited the scope of work to the implementation and validation of a new numerical model and modeling approach. Therefore, the model and research are still at the early stage of development and require further improvements.

In all the simulations conducted in this research, the time steps for the hydrodynamics and sediment scour computations were kept the same. The goal of using the same time steps was to eliminate the influence of time steps on the numerical predictions and to keep the model more accurate. However, the time scale of sediment scour process is typically much larger than that of flow process except at the early stage, therefore, using a different time marching scheme with a larger time step for sediment scour may significantly improve the efficiency of the model without significantly impacting the model accuracy. The influence of different time marching schemes on the numerical predictions may require further investigations.

This study focused on 2D cases because it aimed to develop and validate the modeling approach. The experiments used for model validation were found to be 2D, so conducting 2D simulations is reasonable and correct in terms of reproducing the experimental conditions. However, many applications in nature are 3D, such as sediment scour in channel bends. Therefore, future research could further apply the model for 3D applications. It should be mentioned that fully 3D numerical modeling of sediment scour is typically very computationally expensive, so the influence of time marching schemes should be first investigated to improve the model efficiency prior to modeling a 3D case.

A major advantage of the present model is that it is implemented within the framework of OpenFOAM, so it can be readily modified or extended, and thus can be easily used to check how the numerical schemes, sub-models, and configurations affect the numerical predictions. The current research has already conducted some sensitivity analyses, such as those regarding different turbulence models, bedload equations, and roughness height estimations. However, the main goals of conducting these studies are to demonstrate that the model can be freely extended and to discuss how the model can be further improved.

Future research could be conducted using the current model to deeply investigate the influence of a numerical scheme, a sub-model, and model configurations on the numerical simulations. The model can be further optimized for practical applications. For example, the time marching scheme and grid resolution could be further optimized to provide a better balance between model accuracy and efficiency. The accuracy of the model could be further improved by adding wall functions near the embedded structures.

References

Aamir, M., & Ahmad, Z. (2016). Review of literature on local scour under plane turbulent wall jets. *Physics of Fluids, 28*(10), 105102.

Ackers, P., & White, W. (1993). Sediment transport in open channels: Ackers and White update. Technical note. *Proceedings of the Institution of Civil Engineers-Water Maritime and Energy, 101*(4), 247-249.

Ali, K. H. M., & Lim, S. Y. (1986). Local scour caused by submerged wall jets. *Proceedings of the Institution of Civil Engineers, 81*(4), 607-645.

Amoudry, L. O., & Liu, P. F. (2009). Two–dimensional, two–phase granular sediment transport model with applications to scouring downstream of an apron. *Coastal Engineering*, *56*(7), 693–702.

Apsley, D. D., & Stansby, P. K. (2008). Bed–load sediment transport on large slopes: Model formulation and implementation within a RANS solver. *Journal of Hydraulic Engineering*, *134*(10), 1440–1451.

Altinbilek, H. D., & Basmaci, Y. (1973). Localized scour at the downstream of outlet structures. In *Proceedings of the 11th Congress on Large Dams* (pp. 105-121).

Bagnold, R. A. (1973). The nature of saltation and of'bed-load'transport in water. In *Proceedings of the Royal Society of London A: Mathematical, Physical and Engineering Sciences* (Vol. 332, No. 1591, pp. 473-504). The Royal Society.

Bagnold, R.A. (1980). *An empirical correlation of bedload transport rates in flumes and* *natural rivers*. Proc. Royal Society, London A 405, 369–374.

Bathurst, J. C. (2007). Effect of coarse surface layer on bed-load transport. *Journal of Hydraulic Engineering, 133*(11), 1192-1205.

Behrens, T. (2009). OpenFOAM's basic solvers for linear systems of equations. *Chalmers, Department of Applied Mechanics, 18*(02).

Bigot, B., Bonometti, T., Lacaze, L., & Thual, O. (2014). A simple immersed-boundary method for solid–fluid interaction in constant-and stratified-density flows. *Computers & Fluids, 97*, 126-142.

Bray, D. I., & Davar, K. S. (1987). Resistance to flow in gravel–bed rivers. *Canadian Journal of Civil Engineering*, *14*(1), 77–86.

Brown, C. B. (1950). Sediment transportation. *Engineering hydraulics, 12*.

Brørs, B. (1999). Numerical modeling of flow and scour at pipelines. *Journal of hydraulic Engineering*, *125*(5), 511-523.

Camenen, B., & Larson, M. (2006). Phase-lag effects in sheet flow transport. *Coastal Engineering*, *53*(5-6), 531-542.

Charin, A. H. L. M., Tuković, Ž., Jasak, H., Silva, L. F. L., & Lage, P. L. (2017). A moving mesh interface tracking method for simulation of liquid–liquid systems. *Journal of computational physics, 334*, 419–441.

Chatterjee, S. S., Ghosh, S. N., & Chatterjee, M. (1994). Local scour due to submerged horizontal jet. *Journal of Hydraulic Engineering, 120*(8), 973–992.

Chen, L., & Holst, M. (2011). Efficient mesh optimization schemes based on optimal Delaunay triangulations. *Computer Methods in Applied Mechanics and Engineering*, *200*(9–12), 967–984.

Cheng, Z., Hsu, T. J., & Calantoni, J. (2017). SedFoam: A multi–dimensional Eulerian two–phase model for sediment transport and its application to momentary bed failure. *Coastal Engineering*, *119*, 32–50.

Cooper, J. R., Aberle, J., Koll, K., & Tait, S. J. (2013). Influence of relative submergence on spatial variance and form-induced stress of gravel-bed flows. *Water Resources Research*, *49*(9), 5765-5777.

Demirel, E. (2015). Measured and simulated flow downstream of the submerged sluice gate. *Water and Environment Journal*, *29*(3), 446-455.

Dey, S., & Sarkar, A. (2006). Scour downstream of an apron due to submerged wall jets. *Journal of hydraulic engineering*, *132*(3), 246–257.

Dissanayake, A. L., Yapa, P. D., & Nakata, K. (2014). Modelling of hydrothermal vent plumes to assess the mineral particle distribution. *Journal of Hydraulic Research, 52*(1), 49-66.

Dodaro, G., Tafarojnoruz, A., Sciortino, G., Adduce, C., Calomino, F., & Gaudio, R. (2016). Modified Einstein sediment transport method to simulate the local scour evolution downstream of a rigid bed. *Journal of Hydraulic Engineering, 142*(11), 04016041.

Einstein, H.A., 1950. *The bed-load function for sediment transportation in open* *channel flows*. Technical Bulletin, No. 1026, U.S. Dep. of Agriculture, Washington, D.C

Elalfy, E., Tabrizi, A. A., & Chaudhry, M. H. (2017). Numerical and Experimental Modeling of Levee Breach Including Slumping Failure of Breach Sides. *Journal of Hydraulic Engineering, 144*(2), 04017066.

Engelund, F., & Fredsøe, J. (1976). A sediment transport model for straight alluvial channels. *Hydrology Research, 7*(5), 293–306.

Fang, H. W., & Wang, G. Q. (2000). Three-dimensional mathematical model of suspended-sediment transport. *Journal of Hydraulic Engineering, 126*(8), 578-592.

Fang, H. W., & Rodi, W. (2003). Three-dimensional calculations of flow and suspended sediment transport in the neighborhood of the dam for the Three Gorges Project (TGP) reservoir in the Yangtze River. *Journal of Hydraulic Research, 41*(4), 379-394.

Fang, J., Chen, Y., Yao, P., & Su, M. (2016). Effective Roughness Height in High–Concentrated Flows. *Journal of Coastal Research*, *75*(sp1), 53–57.

Fluent, A. (2017). ANSYS Fluent theory guide 18.0. *Ansys Inc. USA*.

Franz, G., Leitão, P., Pinto, L., Jauch, E., Fernandes, L., & Neves, R. (2017). Development and validation of a morphological model for multiple sediment classes. International *Journal of Sediment Research, 32*(4), 585-596.

Fuhrman, D. R., Baykal, C., Sumer, B. M., Jacobsen, N. G., & Fredsøe, J. (2014). Numerical simulation of wave-induced scour and backfilling processes beneath submarine pipelines. Coastal engineering, 94, 10-22.

Glover, T. J. (1995). Pocket Ref. Sequoia Publishing. ISBN 978-1885071002.

Gomez, B., & Church, M. (1989). An assessment of bed load sediment transport formulae for gravel bed rivers. *Water Resources Research*, *25*(6), 1161-1186.

Guan, D., Melville, B. W., & Friedrich, H. (2015). Live-bed scour at submerged weirs. *Journal of Hydraulic Engineering*, *141*(2), 04014071.

Guan, D., Melville, B., & Friedrich, H. (2016). Local scour at submerged weirs in sand-bed channels. *Journal of Hydraulic Research*, *54*(2), 172-184.

Habibzadeh, A., & Rajaratnam, N. (2016). Turbulent Jet Approach to Predict Expansion Head Loss at Submerged Outlets. *Journal of Hydraulic Engineering*, *142*(10), 06016011.

Haddadchi, A., Omid, M. H., & Dehghani, A. A. (2013). Bedload equation analysis using bed load-material grain size. *Journal of Hydrology and Hydromechanics*, *61*(3), 241-249.

Hirt, C. W., & Nichols, B. D. (1981). Volume of fluid (VOF) method for the dynamics of free boundaries. *Journal of computational physics*, *39*(1), 201–225.

Hoffmans, G. J. (1998). Jet scour in equilibrium phase. *Journal of Hydraulic Engineering*, *124*(4), 430-437.

Holzmann, T. (2016). Mathematics, Numerics, Derivations and OpenFOAM®. *Loeben, Germany: Holzmann CFD, URl: https://holzmann-cfd. de (visited on Nov. 29, 2017).*

Jamieson, E. C., Rennie, C. D., & Townsend, R. D. (2013). 3D flow and sediment dynamics in a laboratory channel bend with and without stream barbs. *Journal of Hydraulic Engineering, 139*(2), 154-166.

Jasak, H. (2009). Dynamic mesh handling in OpenFOAM. *In 47th AIAA Aerospace Sciences Meeting Including the New Horizons Forum and Aerospace Exposition* (p. 341).

Jasak, H., & Tukovic, Z. (2006). Automatic mesh motion for the unstructured finite volume method. *Transactions of FAMENA, 30*(2), 1-20.

Jensen, B. L., Sumer, B. M., Jensen, H. R., & Fredsoe, J. (1990). Flow around and forces on a pipeline near a scoured bed in steady current. Journal of Offshore Mechanics and Arctic Engineering, 112(3), 206-213.

Jian, S. U. N., Lin, B. L., & Kuang, H. W. (2015). Numerical modelling of channel migration with application to laboratory rivers. *International Journal of Sediment Research, 30*(1), 13-27.

Jones, W. P., & Launder, B. (1972). The prediction of laminarization with a two–equation model of turbulence. *International journal of heat and mass transfer, 15*(2), 301–314.

Kashyap, S., Constantinescu, G., Rennie, C. D., Post, G., & Townsend, R. (2012). Influence of channel aspect ratio and curvature on flow, secondary circulation, and bed shear stress in a rectangular channel bend. *Journal of Hydraulic Engineering, 138*(12), 1045-1059.

Khosronejad, A., Rennie, C. D., Salehi Neyshabouri, S. A. A., & Townsend, R. D. (2007). 3D numerical modeling of flow and sediment transport in laboratory channel bends. *Journal of hydraulic Engineering*, *133*(10), 1123–1134.

Khosronejad, A., & Rennie, C. D. (2010). Three-dimensional numerical modeling of unconfined and confined wall-jet flow with two different turbulence models. *Canadian Journal of Civil Engineering*, *37*(4), 576-587.

Khosronejad, A., Kang, S., Borazjani, I., & Sotiropoulos, F. (2011). Curvilinear immersed boundary method for simulating coupled flow and bed morphodynamic interactions due to sediment transport phenomena. *Advances in water resources*, *34*(7), 829–843.

Kironoto, B. A., Graf, W. H., & REYNOLDS. (1994). Turbulence characteristics in rough uniform open-channel flow. *Proceedings of the Institution of Civil Engineers-Water Maritime and Energy*, *106*(4), 333-344.

Kitsikoudis, V., Sidiropoulos, E., & Hrissanthou, V. (2015). Assessment of sediment transport approaches for sand-bed rivers by means of machine learning. *Hydrological sciences journal*, *60*(9), 1566-1586.

Knack, I., & Shen, H. T. (2015). Sediment transport in ice-covered channels. *International Journal of Sediment Research*, *30*(1), 63-67.

Koch, F.G. and Flokstra, C., 1981. Bed level computations for curved alluvial channels. *19th IAHR congress, Vol. 2*, New Delhi, India.

Langendoen, E. J., Mendoza, A., Abad, J. D., Tassi, P., Wang, D., Ata, R., ... &

Hervouet, J. M. (2016). *Improved numerical modeling of morphodynamics of rivers with steep banks. Advances in water resources*, *93*, 4-14.

Lee, W. W. L. (1995). Erosion downstream of a sluice gate. *Final Year Project, Nanyang Technological University, Singapore*.

Lee, C. H., Low, Y. M., & Chiew, Y. M. (2016). Multi–dimensional rheology–based two–phase model for sediment transport and applications to sheet flow and pipeline scour. *Physics of Fluids*, *28*(5), 053305.

Lee, C. H., Xu, C., & Huang, Z. (2017). A three–phase flow simulation of local scour caused by a submerged wall jet with a water–air interface. *Advances in Water Resources*.

Legates, D. R., & McCabe Jr, G. J. (1999). Evaluating the use of "goodness-of-fit" measures in hydrologic and hydroclimatic model validation. *Water resources research*, *35*(1), 233-241.

Liang, D., Cheng, L., & Li, F. (2005). Numerical modeling of flow and scour below a pipeline in currents: Part II. Scour simulation. *Coastal engineering, 52*(1), 43-62.

Lim, S. Y., & Yu, G. (2002). Scouring downstream of sluice gate. In *First International Conference on Scour of FoundationsInternational Society of Soil Mech and Foundations*.

Liu, X., & García, M. H. (2008). Three–dimensional numerical model with free water surface and mesh deformation for local sediment scour. *Journal of waterway, port, coastal, and ocean engineering*, *134*(4), 203–217.

Mao, Y. (1986). *The interaction between a pipeline and an erodible bed*. PhD thesis, Institute of Hydrodynamics and Hydraulic Engineering, Technical University of Denmark, Lyngby, Denmark.

Marsooli, R., & Wu, W. (2014). Three–dimensional numerical modeling of dam–break flows with sediment transport over movable beds. *Journal of Hydraulic Engineering, 141*(1), 04014066.

Melville, B. W., & Lim, S. Y. (2013). Scour caused by 2D horizontal jets. *Journal of Hydraulic Engineering*, *140*(2), 149–155.

Mendoza, A., Abad, J. D., Langendoen, E. J., Wang, D., Tassi, P., & Abderrezzak, K. E. K. (2016). Effect of sediment transport boundary conditions on the numerical modeling of bed morphodynamics. *Journal of Hydraulic Engineering*, *143*(4), 04016099.

Meng, Z., Li, D., & Wang, X. (2016). Modification of the Engelund bed-load formula. *International Journal of Sediment Research*, *31*(3), 251-256.

Meyer-Peter, E., & Müller, R. (1948). Formulas for bed-load transport. *In IAHSR 2nd meeting, Stockholm, appendix 2*. IAHR.

Millar, R. G. (1999). Grain and form resistance in gravel-bed rivers. *Journal of Hydraulic Research*, *37*(3), 303-312.

Mil-Homens, J., Ranasinghe, R., de Vries, J. V. T., & Stive, M. J. F. (2013). Re-evaluation and improvement of three commonly used bulk longshore sediment transport formulas. *Coastal Engineering*, *75*, 29-39.

Mirjalili, S., Jain, S. S., & Dodd, M. S (2017). Interface–capturing methods for two–phase flows: An overview and recent developments. *Center for Turbulence Research Annual Research Briefs*, 117–135.

Nakato, T. (1990). Tests of selected sediment-transport formulas. *Journal of Hydraulic Engineering*, *116*(3), 362-379.

Nielsen, P. (1992). *Coastal bottom boundary layers and sediment transport* (Vol. 4). World Scientific Publishing Company.

Nikuradse, J. (1950). Laws of flow in rough pipes. *National Advisory Committee for Aeronautics. NACA Technical Memorandum, NACA Technical Memorandum, 1292*, 60-68.

OpenCFD Limited. (2014). OpenFOAM [user guide]. *Version 2.3.1*.

Paola, C., & Voller, V. R. (2005). A generalized Exner equation for sediment mass balance. *Journal of Geophysical Research: Earth Surface, 110*(F4*)*.

Parker, G. (1978). Self-formed straight rivers with equilibrium banks and mobile bed. Part 1. The sand-silt river. *Journal of Fluid Mechanics*, *89*(1), 109-125.

Parker, G., Klingeman, P. C., & McLean, D. G. (1982). Bedload and size distribution in paved gravel-bed streams. *Journal of the Hydraulics Division*, *108*(4), 544-571.

Paul, A. R., Ranjan, P., Upadhyay, R. R., & Jain, A. (2011). Flow control in twin air–intakes using vertex generators. In *Proceedings of the 2011 international conference on Applied & computational mathematics* (pp. 107–116). World Scientific and

Engineering Academy and Society (WSEAS).

Rajaratnam, N. (1981). Erosion by plane turbulent jets. *Journal of hydraulic Research, 19*(4), 339-358.

Rajaratnam, N., & Macdougall, R. K. (1983). Erosion by plane wall jets with minimum tailwater. *Journal of Hydraulic Engineering*, *109*(7), 1061-1064.

Rijn, L. C. V. (1986). Mathematical modeling of suspended sediment in nonuniform flows. *Journal of Hydraulic Engineering*, *112*(6), 433-455.

Rusche, H. (2002). *Computational fluid dynamics of dispersed two–phase flows at high phase fractions* (Doctoral dissertation, Imperial College London).

Sarathi, P., Faruque, M. A. A., & Balachandar, R. (2008). Influence of tailwater depth, sediment size and densimetric Froude number on scour by submerged square wall jets. *Journal of Hydraulic Research*, *46*(2), 158-175.

Sarker, M. A., & Rhodes, D. G. (2004). Calculation of free-surface profile over a rectangular broad-crested weir. *Flow measurement and Instrumentation*, *15*(4), 215-219.

Sasal, M., Kashyap, S., Rennie, C.D., Nistor, I. Artificial Neural Network for bedload estimation in alluvial rivers, *Journal of Hydraulic Research*, *47*(2):223–232, 2009.

Schoklitsch, A. (1962). *Handbuch des Wasserbaus*, Springer-Verlag, Vienna, Austria

Shayan, H. K., Farhoudi, J., & Hamidifar, H. (2015). Estimation of maximum scour depth downstream of horizontal and adverse stilling basins using a semi-theoretical approach. *International journal of civil engineering, 13*(1 A), 1-15.

Shcherbakov, M. V., Brebels, A., Shcherbakova, N. L., Tyukov, A. P., Janovsky, T. A., & Kamaev, V. A. E. (2013). A survey of forecast error measures. *World Applied Sciences Journal*, *24*(24), 171-176.

Shen, Z., Wan, D., & Carrica, P. M. (2015). Dynamic overset grids in OpenFOAM with application to KCS self-propulsion and maneuvering. *Ocean Engineering, 108*, 287-306.

Smith, H. D., & Foster, D. L. (2005). Modeling of flow around a cylinder over a scoured bed. *Journal of waterway, port, coastal, and ocean engineering*, *131*(1), 14-24.

Soulsby, R. L., & Whitehouse, R. J. S. (1997). Threshold of sediment motion in coastal environments. In *Pacific Coasts and Ports' 97: Proceedings of the 13th Australasian Coastal and Ocean Engineering Conference and the 6th Australasian Port and Harbour Conference; Volume 1* (p. 145). Centre for Advanced Engineering, University of Canterbury.

Sumer, B. M. (2014). A review of recent advances in numerical Modeling of local scour problems. In *Proc., 7th Int. Conf. on Scour and Erosion* (pp. 61–70).

Tarapore, Z. S. (1956). *Scour below a submerged sluice gate* (Doctoral dissertation, University of Minnesota).

Team, C. (2016). Cubit, geometry and mesh generation toolkit: version 15.2 user's manual. *Sandia National Laboratories, Tech. Rep. SAND2016–1649 R.*

Tezduyar, T. E. (2006). Interface–tracking and interface–capturing techniques for finite element computation of moving boundaries and interfaces. *Computer Methods in Applied Mechanics and Engineering*, *195*(23–24), 2983–3000.

Thorimbert, Y., Marson, F., Parmigiani, A., Chopard, B., & Lätt, J. (2018). Lattice Boltzmann simulation of dense rigid spherical particle suspensions using immersed boundary method. *Computers & Fluids*, *166*, 286-294.

Tomas, G., Bleninger, T., Rennie, C. D., & Guarneri, H. (2018). Advanced 3D Mapping of Hydrodynamic Parameters for the Analysis of Complex Flow Motions in a Submerged Bedrock Canyon of the Tocantins River, Brazil. *Water*, *10*(4), 367.

Ubbink, O., & Issa, R. I. (1999). A method for capturing sharp fluid interfaces on arbitrary meshes. *Journal of Computational Physics*, *153*(1), 26–50.

van Rijn, L. C. (1982). Equivalent roughness of alluvial bed. *Journal of the Hydraulics Division*, *108*(10), 1215-1218.

van Rijn, L. C. (1984). Sediment transport, part I: bed load transport. J*ournal of hydraulic engineering*, *110*(10), 1431-1456.

Wang, L., Melville, B. W., & Guan, D. (2018a). Effects of upstream weir slope on local scour at submerged weirs. Journal of Hydraulic Engineering, 144(3), 04018002.

Wang, L., Melville, B. W., Guan, D., & Whittaker, C. N. (2018b). Local scour at downstream sloped submerged weirs. *Journal of Hydraulic Engineering, 144*(8), 04018044.

Wang, Z. B., & Ribberink, J. S. (1986). The validity of a depth-integrated model for suspended sediment transport. *Journal of Hydraulic Research, 24*(1), 53-67.

Watts, M., Aliabadi, S., & Tu, S. (2005). A coupled interface–tracking/interface–capturing technique for free–surface flows. *WIT Transactions on Engineering Sciences, 50*.

Wei, G., Brethour, J., Grünzner, M., & Burnham, J. (2014). Sedimentation scour model. *Flow Science Report*, 03–14.

Wendt, J. F. (Ed.). (2008). *Computational fluid dynamics: an introduction*. Springer Science & Business Media.

Wong, M., & Parker, G. (2006). Reanalysis and correction of bed-load relation of Meyer-Peter and Müller using their own database. *Journal of Hydraulic Engineering, 132*(11), 1159-1168.

Wren, D. G., Rigby, J. R., Langendoen, E. J., & Kuhnle, R. A. (2018). Sampling Interval Analysis and CDF Generation for Grain-Scale Gravel Bed Topography. *Journal of Hydraulic Engineering, 144*(10), 04018065.

Wu, P., Balachandar, R., & Ramamurthy, A. (2018). Effects of splitter plate on reducing local scour around bridge pier. *River Research and Applications, 34*(10), 1338-1346.

Xie, L., Zhu, Y., & Su, T. C. (2019). Scour protection of partially embedded pipelines using sloping curtains. *Journal of Hydraulic Engineering, 145*(3), 04019001.

Yan, X., & Mohammadian, A. (2017). Numerical Modeling of Vertical Buoyant Jets

Subjected to Lateral Confinement. *Journal of Hydraulic Engineering, 143*(7), 04017016.

Yan, X., Mohammadian, A. (2019). Numerical Modeling of Multiple Inclined Dense Jets Discharged from Moderately Spaced Ports. *Water*, *11*, 1-15. doi:10.3390/w11102077.

Yan, X., Mohammadian, A., Chen, X. (2019). Three-dimensional numerical simulations of buoyant jets discharged from a rosette-type multiport diffuser. *Journal of Marine Science and Engineering*, *7*(11), 409, 1-15.

Yan, X., Mohammadian, A., & Rennie, C. D. (2020a). Numerical Modeling of Flow and Local Scour around Pipeline in Steady Currents Using Moving Mesh with Masked Elements. J*ournal of Hydraulic Engineering, 146*(5), 06020005.

Yan, X., Mohammadian, A., and Rennie C.D. (2020b). Numerical modeling of local scour due to submerged wall jets using a strict vertex-based, terrain conformal, moving-mesh technique in OpenFOAM. *International Journal of Sediment Research, 35*(3), 237-248.

Yan, X., Ghodoosipour, B., and Mohammadian. (2020c). Three-dimensional numerical study of multiple vertical buoyant jets in stationary ambient water. *Journal of Hydraulic Engineering, in press,* DOI: 10.1061/(ASCE)HY.1943-7900.0001768.

Yan, X., Rennie, C.D. and Mohammadian, A. (2020d). A three-dimensional numerical study of flow characteristics in strongly curved channel bends with different side slopes. *Environmental Fluid Mechanics*. https://doi.org/10.1007/s10652-020-09751-9

Yang, C. T. (1984). Unit stream power equation for gravel. *Journal of Hydraulic*

Engineering, *110*(12), 1783-1797.

Yeganeh-Bakhtiary, A., Kazeminezhad, M. H., Etemad-Shahidi, A., Baas, J. H., & Cheng, L. (2011). Euler–Euler two-phase flow simulation of tunnel erosion beneath marine pipelines. *Applied Ocean Research*, *33*(2), 137-146.

Zhao, M., Cheng, L., & Zang, Z. (2010). Experimental and numerical investigation of local scour around a submerged vertical circular cylinder in steady currents. *Coastal Engineering*, *57*(8), 709–721.

Zhao, M., & Cheng, L. (2008). Numerical modeling of local scour below a piggyback pipeline in currents. *Journal of Hydraulic Engineering*, *134*(10), 1452-1463.

Zhao, Z., & Fernando, H. J. S. (2007). Numerical simulation of scour around pipelines using an Euler–Euler coupled two-phase model. *Environmental Fluid Mechanics*, *7*(2), 121-142.

Zhao, M., Vaidya, S., Zhang, Q., & Cheng, L. (2015). Local scour around two pipelines in tandem in steady current. *Coastal Engineering*, *98*, 1-15.

Zhong, D. Y., Wang, G. Q., & Zhang, L. (2012). A bed-load function based on kinetic theory. *International Journal of Sediment Research*, *27*(4), 460-472.